Optimization of Integrated Power Systems with Hydrogen-Based Infrastructure: Strategic Operation, Planning and Benefits Analysis

by
Jin Lu

A report submitted to the Department of Electrical and Computer Engineering,

Cullen College of Engineering

in partial fulfillment of the requirements for the degree of

Doctor of Philosophy

in Electrical and Computer Engineering

Chair of Committee: Dr. Xingpeng Li

Committee Member: Dr. Kaushik Rajashekara

Committee Member: Dr. Harish Sarma Krishnamoorthy

Committee Member: Dr. Zhu Han

Committee Member: Dr. Lei Fan

University of Houston

August 2024

ACKNOWLEDGMENTS

I would like to express my sincere gratitude and appreciation to Dr. Xingpeng Li for his unwavering support, profound expertise, and patience throughout my Ph.D. studies in the Renewable Power Grid lab and Power Electronics, Microgrids & Subsea Electrical Systems Center at the University of Houston. His mentorship has been crucial to the completion of this research.

I am immensely grateful to the members of my dissertation committee, Prof. Kaushik Rajasekhara, Prof Harish Sarma Krishnamoorthy, Prof. Zhu Han, together with Prof Lei Fan. I greatly appreciate their insightful feedback, thoughtful critiques, and the generous amount of time they devoted, all of which has substantially improved this dissertation.

Special thanks to the graduated students, Dr. Arun Venkatesh Ramesh, Dr. Mingjian Tuo and Dr. Cunzhi Zhao, as well as current students Thuan Pham, Jesus Silva-Rodriguez, Ann Mary Toms, Rida Fatima, Hassan Zahid Butt, Qiushi Wang, Lei Jiang, and Elias Raffoul. Their academic and emotional support has been invaluable. The insights and discussions we shared have profoundly enriched my academic journey.

I would like to thank my parents, Bingliang Lu and Hong Xu for their unwavering love and support in the past four years. Their constant encouragement has inspired me to strive for academic excellence.

ABSTRACT

This dissertation investigates the optimization of integrated power systems with a focus on hydrogen-based infrastructure, aiming to enhance strategic operation and planning. The increasing integration of renewable energy sources, such as wind and solar, has necessitated innovative solutions to address the inherent variability and stability challenges in power grids. Despite the potential of hydrogen technology to mitigate these challenges, current strategies for grid operation and planning often overlook the synergistic integration of hydrogen production, storage, and utilization with electric power systems. This research aims to bridge this gap by developing advanced modeling and optimization techniques for grids integrated with hydrogen energy systems, to improve the economic efficiency and reliability of power systems.

Novel strategies are proposed for the daily operation of hybrid grids, incorporating hydrogen energy transmission and conversion systems (HETCS) and energy hubs. These strategies co-optimize the conversion, storage, and transmission of hydrogen. By developing comprehensive models for seasonal hydrogen storage, the research addresses the need for long-term energy management solutions that balance renewable production and load demands throughout the year.

Novel planning methods for offshore hybrid energy transmission and bulk power system hybrid transmission are also proposed. The planning strategy allows for selective investment in either hydrogen pipelines or electrical transmission lines for different sections or routes. The creation of the Texas 123-bus backbone transmission

(TX-123BT) test case, which includes spatio-temporally correlated profiles for extended periods, enables long term simulation-based studies. It serves as a critical tool for evaluating the integration and impact of hydrogen on future renewable grids. Numerical results from the TX-123BT demonstrate that the proposed planning models can reduce electrical transmission investments and lower overall grid costs.

To enhance the reliability of the hydrogen integrated power systems, restoration strategies utilizing fuel cells or battery energy storage as black start (BS) resources are proposed. The novel models include detailed formulation and linearization of the output characteristics of the fuel cells. The generator start-up sequences (GSUS) for restoration using fuel cells and batteries are compared, and network reconfiguration times are analyzed.

TABLE OF CONTENTS

LIST OF TABLES

LIST OF FIGURES

1. INTRODUCTION

1.1 Background

Hydrogen energy is increasingly capturing the attention of modern society, especially in the fields of transportation, energy storage, and power generation [1]–[5]. In the power industry, hydrogen is recognized as a clean energy source and is pivotal to the development of renewable grids with minimal or zero carbon emissions [6]–[7]. Hydrogen's potential as a key component in future grids is underscored by its environmentally friendly production and usage. It can be produced from water using electrolyzers, a process that consumes electric power while yielding oxygen as a byproduct—a potential resource under study for further utilization. The consumption of hydrogen, mainly through fuel cells, generates electricity for various applications like transportation and power generation. Fuel cells oxidize hydrogen, producing water and heat, which can be effectively used, underscoring hydrogen's clean and sustainable nature for future renewable energy grids.

Electric power grids can integrate hydrogen resources through a series of processes including electric-hydrogen conversion, hydrogen storage, and transmission via pipelines [8]-[10]. Electric energy in power grids is transmitted through lines from generators to loads and can be stored in various forms such as batteries, compressed air, and pumped-hydro storage. To integrate hydrogen transmission and storage into the electric power system, facilities such as fuel cells and electrolyzers are utilized to enable the conversion of hydrogen and electric energy into each other. From the

electric grid's perspective, electric energy can first be converted into hydrogen energy, and then be transmitted and stored through the hydrogen pipeline and storage, which will be converted back into electricity whenever it is needed. Hence, the integration of hydrogen can improve the electric grids on both transmission and storage aspects.

The future grids are expected to be dominated by renewable energy resources [11]–[12], necessitating substantial energy storage capacity to manage the intermittency and unpredictability of these sources. Moreover, such renewables-dominated power grids will require extensively additional transmission capacity, influenced by the geographical distribution of renewable energy plants [13]–[14]. Often located in areas with high wind or solar radiation potential, these plants are typically distant from load centers, necessitating the transfer of large amounts of renewable energy. Employing or integrating existing hydrogen transmissions has the potential to alleviate the high transmission capacity demands caused by significant renewable penetration. While existing hydrogen pipelines are limited, there are examples of utilities upgrading natural gas pipelines for hydrogen or hydrogen blend delivery [15]–[17]. Additionally, a number of studies are assessing the feasibility and economics of hydrogen transmission [18]–[19]. This indicates the growing potential for hydrogen transmission in real-world applications, supported by the trend towards renewable development and the existing natural gas network.

However, practical applications of hydrogen still face challenges, including high costs, leakage risks, and energy conversion inefficiencies [20]–[22]. The small size of hydrogen molecules can lead to increased leakage rates. Additionally,

hydrogen embrittlement can weaken metals, necessitating pipelines made of or lined with materials resistant to this phenomenon, increasing production and maintenance costs. Moreover, energy conversion inefficiency remains a significant barrier to hydrogen integration into power systems [23]. For instance, the ideal efficiency for PEM electrolyzers is around 80% [24]–[25], and only 60% for PEM fuel cells [26]–[27]. This means a substantial portion of energy is lost during conversion, making increased efficiency crucial for hydrogen's viability in power transmission.

Despite these challenges, hydrogen transmission is expected to become more feasible and practical for future renewable energy grids. As grids incorporate more renewables, the low efficiency of conversion becomes less critical, particularly when utilizing abundant, low-cost renewable energy for conversion processes. Additionally, advancements in hydrogen technologies are likely to reduce costs associated with hydrogen conversion and transmission [28]–[31]. For example, the cost of electrolyzers is anticipated to decrease due to economies of scale in both module and manufacturing plant sizes [32]. The International Renewable Energy Agency (IRENA) projects that investment costs for electrolyzers could decrease by 40% in the near term and potentially by up to 80% in the future [33]. Improvements in fuel cell durability and power density are also expected. In [34], the key points to increase the power density of proton-exchange membrane fuel cell (PEMFC) is discussed. Research focused on fuel cell catalyst technology is pivotal for enhancing fuel cell durability [35]–[36]. For hydrogen transmission, materials that slow down hydrogen

embrittlement and reduce leakage risks are under development, with numerous studies investigating suitable materials for hydrogen pipelines [37]–[39].

1.2 Motivations

While significant advancements in hydrogen technologies are anticipated, the operation and planning of renewable grids integrated with hydrogen remain critical for optimizing the advantages and benefits of hydrogen. Current strategies employed by independent system operators (ISOs) or regional transmission organizations (RTOs), such as economic dispatch and security-constrained unit commitment (SCUC), primarily address electric transmission constraints like nodal power balance and line flow equations [40]–[41]. However, these strategies do not account for hydrogen transmission and storage constraints, rendering them insufficient for managing hydrogen facility operations. Furthermore, there is a lack of consideration for the synergy between electric and hydrogen systems, which could yield optimal operation solutions for grid benefits. It's also necessary for grid planning to consider hydrogen integration. Wise investment in hydrogen facilities is essential to achieve the reliability and economic efficiency of the power-hydrogen hybrid energy grids. Suitable facility placement lays the foundation for reliable and economical grid operations. Expansion planning strategies should account for operational conditions across different future periods, encompassing constraints similar to those in operational strategies, including generation capacity ramping, reserve requirements, and transmission constraints like line flow thermal limits. Unlike the day-ahead or

real-time operational strategy, transmission planning involves considering multi-scenario forecasts, accommodating long-term shifts in generation and load.

The integration of hydrogen into power grids is still in its early stages, with pioneering research exploring its feasibility and economics [42]–[44]. Some studies focus on the economic viability of hydrogen by evaluating the costs of various hydrogen facilities, such as pipelines and storage tanks, and assessing the entire hydrogen industry chain, including production, transmission, and storage. However, there is a notable gap in simulation-based studies on hydrogen-integrated power systems. Many existing models often focus on individual components (e.g., electrolyzers, fuel cells) rather than integrated operational strategies that consider the entire hybrid energy system. Most planning strategies for both electrical and hydrogen investments do not account for detailed daily co-operation of facilities in hybrid grids. The important dynamics of future grids including the renewable production and dynamic line ratings, are not sufficiently considered. Moreover, performance evaluation and comparison between different hydrogen integration configurations and application scenarios are lacking. Developing suitable optimization models for operational and planning strategies for hybrid systems is essential to fully utilize the benefits of hydrogen. By simulating various future grid changes and improvements in hydrogen technology using these optimal strategies, we can more accurately determine the conditions under which hydrogen becomes economically feasible and gain deeper insights into the benefits brought by integrating hydrogen infrastructure.

1.3 Summary of contents

The rest of this dissertation is structured as follows. The daily operation of the hydrogen integrated power systems is studied in Chapter 2. In this chapter, we establish separate security-constrained unit commitment (SCUC) models for grids integrated with hydrogen transportation systems and local hydrogen hubs. We then simulate the daily operation of these grids at various levels of renewable energy penetration using the optimal strategies. Based on the simulation results, we numerically analyze the benefits, including reductions in wind curtailment, carbon emissions, operational costs, and electricity prices. Additionally, we discuss the site selection of fuel cells to optimize the daily operation of the hybrid grid.

In Chapter 3, we propose strategies for the seasonal scheduling of hydrogen storage. By integrating the hydrogen storage system with salt caverns, long-term energy storage can be achieved. We introduce a novel annual scheduling model (ASM) for hydrogen storage, which schedules the hydrogen import and export from the salt cavern throughout the year. The model determines the hydrogen import and export and the operating points of fuel cells and electrolyzers by modeling the amount of hydrogen stored for each time interval, day, and season using a linearized hydrogen inventory equation. The annual simulation of the grids using the ASM strategy provides a detailed analysis of both intra-day and cross-season electrical-hydrogen energy exchanges.

In Chapter 4, a comprehensive framework for power system test case and future grid profiles is presented, incorporating spatio-temporal correlated profiles that

simulate long-term system dynamics. The created test case TX-123BT is meticulously designed to capture the complex interactions between various elements of the power grid, including conventional and renewable energy sources, load demands, and transmission line capacities. By integrating climate impacts, renewable production variability, and dynamic line ratings, the TX-123BT test case provides a robust platform for evaluating the performance and reliability of power systems under diverse future scenarios. Through detailed simulations, the TX-123BT test case demonstrates its utility in research of hydrogen integrated power systems.

Chapter 5 discusses the innovative strategies for planning and expanding hybrid energy transmission networks, focusing on integrating hydrogen pipelines with electrical transmission lines. This hybrid approach aims to optimize investments, reduce costs, and enhance the reliability of future power systems. The Transmission Expansion Planning (TEP) model introduced in this chapter allows for selective investment in either hydrogen pipelines or electrical transmission lines based on the specific needs of different sections of the network. By co-optimizing these investments, the proposed model ensures a cost-effective and reliable hybrid transmission network. Additionally, the chapter explores offshore hybrid energy transmission configurations, comparing different scenarios to determine under what conditions hydrogen pipelines might be more beneficial than HVDC power transmission.

Chapter 6 delves into the use of fuel cells and battery energy storage systems as black start resources for power system restoration. It presents detailed models that

include the output characteristics of fuel cells and the necessary constraints for using them in black start scenarios. The chapter compares the generator start-up sequences (GSUS) for systems utilizing fuel cells and batteries, highlighting the efficiency and performance improvements of using fuel cells over traditional methods. The chapter also includes an in-depth analysis of network reconfiguration times and the optimal location selection for these black start resources. Through simulations on the IEEE 39-bus system, the chapter demonstrates that integrating fuel cells can significantly improve the startup time of generators and overall restoration performance. The fuel cells can outperform batteries in some situations due to the limitations of battery storage capacity. Sensitivity analyses are conducted to understand the impact of fuel cell capacity and battery storage on restoration efficiency.

Finally, Chapter 7 concludes this dissertation and outlines potential areas for future research.

2. DAILY OPERATION OF HYBRID GRIDS

2.1 Literature Review

Renewable energy plays an increasingly important role in modern power systems due to its sustainability and environmental friendliness. According to U.S. Energy Information Administration, renewable energy is expected to provide 24% of U.S. generation in 2023 [45]. While the increasing renewable energy leads to cleaner power grids, some challenges and issues arise due to intermittency of renewable generation. The flexible resources with high ramping rate and frequent start-up capability are required to ensure the reliability of the grids [46]–[47]. Besides, the increasing renewables cannot be well utilized if the grids do not suit for high renewable penetration [48]–[50]. Specifically, the transmission capacity of the power grids is limited, and unnecessary curtailment of wind/solar power is frequently observed when the network is congested [51]–[53]. For instance, California power grid was forced to curtail 187 GWh of wind and solar generation in 2015, and that number rose to 1,587 GWh in 2020 [54]–[55]. The curtailment of the renewables is a waste of the available green energy, and it also implies the barrier of deploying more renewables under the current grid condition. Furthermore, many potential benefits of the renewables such as accelerating the power system restoration [56] cannot be well utilized.

Lots of research are conducted on renewable grid integration by utilizing energy storage such as electric vehicles, batteries, compressed air and pumped-hydro storage [57]–[60]. The Power-to-hydrogen (P2H) technology can convert electrical

energy into hydrogen [61]. Since the hydrogen can be stored in the hydrogen storage facility and release the energy back to grid using hydrogen-to-power (H2P) facility [62]–[63]. The combination of P2H, hydrogen storage and H2P is capable to realize the energy storage function in the power grids. In [64], the performance of the energy hub (EH) that is equipped with an electrolyzer, hydrogen storage and a hydrogen turbine in the power system with high wind penetration level is investigated. It shows such a combination is capable to reduce wind curtailments, especially for high wind energy penetration conditions.

A number of utilities around the world are upgrading or have set up plans to upgrade the natural gas pipeline network to a network that can handle larger portion of hydrogen mix or even pure hydrogen, while many other utilities are still conducting cost-benefit analysis for such upgrade [65]–[69]. Compared with local hydrogen storage, a hydrogen pipeline network can transmit the hydrogen in addition to storing the hydrogen. A Hydrogen Energy Transmission and Conversion System (HETCS) consisting of H2P, hydrogen pipeline network and P2H can interact and coordinate with the power system. The electrical energy can be converted into the hydrogen energy, stored in the hydrogen pipeline network and salt caverns, and transferred to other locations through the hydrogen pipeline network. Hence, a HETCS is expected to effectively address the over renewable generation and congestion-induced curtailment. Few current literatures investigate the feasibility and performance of a power system that is coupled with HETCS. The purpose of this paper is to fill this gap

by studying the potential benefits of HETCS to the renewable power grids (RPG) with high penetration level of renewable generation.

Security-constrained unit commitment (SCUC) is to determine generator on or off status in power system day-ahead scheduling [68]–[70]. Existing SCUC method only models electrical facilities such as electrical transmission lines, thermal generators and renewable power plants in the power systems. Current SCUC studies mainly focus on grids integrated with local energy hubs. We have further developed the model for hybrid grids that incorporate hydrogen energy transportation and conversion systems (HETCS).

2.2 Hydrogen Energy Transmission and Conversion System

The hydrogen energy transmission and conversion system (HETCS) includes a hydrogen transportation network with hydrogen pipelines between different nodes that are also interfaced with the power grid. The P2H and H2P facilities are placed at such locations covered by both the hydrogen network and the power transmission network.

2.2.1 The functionalities of HETCS from Grid Perspective

The hydrogen network, P2H and H2P facilities constitute the HETCS that benefits the power system mainly through two functions: energy storage function (temporal flexibility) and energy transfer function (spatial flexibility).

For energy storage function, electrical energy can be converted into hydrogen energy by the P2H facilities. Since the hydrogen can be stored in the hydrogen

network and other storage facilities such as salt caverns, the electrical energy can be stored in the form of hydrogen energy. The stored hydrogen energy can be converted back to electrical energy by the H2P facilities.

For energy transfer function, if a power system is coupled with HETCS, it can transfer energy through both the power transmission network and the hydrogen network to serve the loads. Specifically, the electrical energy of excess renewable generation can be converted into hydrogen energy, transferred through the hydrogen network, and converted back to the electrical energy at the destination. Note that the energy can only be transmitted from where the P2H facilities are located to the H2P locations in the HETCS.

In HETCS-coupled power systems, the generated renewable energy can be converted into hydrogen energy and stored in the HETCS. Hence, the disadvantages of intermittent renewable generation can be mitigated. Traditionally, a large amount of renewable generation requires higher transmission capacity. If the transmission lines are congested, it may cause renewable curtailment. In HETCS-coupled power systems, the electrical energy generated by renewable sources can be transferred through HETCS in the form of hydrogen, which reduces the renewable curtailment. Based on the above reasons, we expect HETCS can improve renewable integration in power systems.

2.2.2 Daily Operation of the HETCS Integrated Power Systems

The SCUC model is established to determine the optimal operational scheduling of the power system for the next day and is widely used in the industry.

The optimal solution to SCUC is the most cost beneficial operational schedule, which includes generator commitment status and generation. The power system conditions such as transmission line power flow can also be obtained, as well as locational marginal price (LMP).

The object of the power grid daily operation model SCUC is to minimize the total cost of the power system, which consists of generator operation cost, generator no-load cost and generator startup cost. This objective function is represented as:

$$\min \sum_{g\in G}\sum_{t\in T}\left(c_g P_{gt} + c_g^{NL} u_{gt} + c_g^{SU} v_{gt}\right). \tag{2.1}$$

The constraints including generator maximum and minimum output, reserve, ramping up as well as the power flow in transmission network are as follows:

$$P_g^{\min} u_{gt} \le P_{gt} \quad (g \in G, t \in T), \tag{2.2}$$

$$P_{gt} + r_{gt} \le P_g^{\max} u_{gt} \quad (g \in G, t \in T), \tag{2.3}$$

$$0 \le r_{gt} \le R_g^{10} u_{gt} \quad (g \in G, t \in T), \tag{2.4}$$

$$\sum_{m\in G} r_{mt} \ge P_{gt} + r_{gt} \quad (g \in G, t \in T), \tag{2.5}$$

$$P_{kt} = \theta_{kt}/x_k \quad (k \in K, t \in T), \tag{2.6}$$

$$-P_k^{max} \le P_{kt} \le P_k^{max} \quad (k \in K, t \in T), \tag{2.7}$$

$$0 \le P_{wt}^{Cur} \le P_{wt} \quad (w \in W, t \in T), \tag{2.9}$$

$$-R_g \le P_{gt} - P_{g,t-1} \le R_g \quad (g \in G, t \in T), \tag{2.10}$$

$$v_{gt} \ge u_{gt} - u_{g,t-1} \quad (g \in G, t \in T), \tag{2.11}$$

$$v_{gt} \in \{0,1\} \quad (g \in G, t \in T), \tag{2.12}$$

$$\text{and } u_{gt} \in \{0,1\} \quad (g \in G, t \in T), \tag{2.13}$$

where generators' maximum and minimum output limit is included in (2.2) and (2.3). The generator reserve requirements are considered using (2.4) – (2.5); DC power flow equation is shown in (2.6) and the power flow limits are imposed in (2.7). Since this study focuses on the curtailment of renewable energy, P_{wt}^{Cur} is used to evaluate the curtailment of the wind power. The renewable curtailment limitation is in (2.9). The generator ramping constraint is shown in (2.10). The binary variables denoting generator status are u_{gt} and v_{gt}, which are described by (2.11) – (2.13).

In our model formulation, we assume the P2H facilities in the HETCS are electrolyzers, and the H2P facilities are fuel cells. We use variable P_{et} to represents the electrical power consumed by the electrolyzer *e* at time *t*. Similarly, we use P_{ft} to represents the electrical power generated by the fuel cell *f* at time *t*. The nodal power balance equation considering the power consumed or generated by the hydrogen facilities is shown as:

$$\sum_{g \in G(n)} P_{gt} + \sum_{k \in K(n-)} P_{kt} - \sum_{k \in K(n+)} P_{kt} + \sum_{w \in W(n)} P_{wt} - \sum_{w \in W(n)} P_{wt}^{Cur} + \sum_{f \in F(n)} P_{ft} = d_{nt} + \sum_{e \in E(n)} P_{et} \quad (n \in N, t \in T). \tag{2.14}$$

We use η_e and η_f to describe the energy conversion efficiency of the electrolyzer and fuel cell respectively. Additionally, Δt represents the time interval of each time step in the model. The hydrogen energy stored in HETCS can be calculated by

$$E_t = E_{t-1} + \sum_{e \in E} \eta_e P_{et} \cdot \Delta t - \sum_{f \in F} P_{ft}/\eta_f \cdot \Delta t \quad (t \in T). \tag{2.15}$$

For any time interval, the hydrogen energy stored in the hydrogen network should be larger than zero and less than the maximum storage capacity. It is described as:

$$0 \leq E_t \leq E^{\max} \ (t \in T). \tag{2.16}$$

The electrolyzer and fuel cell power capacity constraints are as follows:

$$0 \leq P_{et} \leq P_e^{\max} \ (e \in E, t \in T) \tag{2.17}$$

$$\text{and } 0 \leq P_{ft} \leq P_f^{\max} \ (f \in F, t \in T). \tag{2.18}$$

Since this model is focused on providing preliminary benefit analysis of the proposed HETCS to the renewable power grid, for simplicity, we ignored the costs associated with hydrogen transmission and storage.

2.3 Daily Operation of the Energy Hub Integrated Power Systems

Electrical energy can be converted and stored locally as hydrogen energy in a hydrogen energy hub (EH). In daily operations, as illustrated in Figure 2.1, the hydrogen energy hub interacts seamlessly with the power system. Electric power, potentially generated from renewable sources such as solar or wind, is first directed to an electrolyzer. The electrolyzer uses this electricity to split water molecules into hydrogen and oxygen through the process of electrolysis. The generated hydrogen is then stored locally in hydrogen storage facilities. When there is a demand for energy,

the stored hydrogen can be converted back into electric power using a fuel cell. This power is then fed back into the local substation, making it available for immediate use within the grid. This dual capability of storing energy locally and returning it to the grid when needed ensures a continuous and stable power supply, enhances the reliability of renewable energy sources, and reduces the environmental impact associated with long-distance electricity transmission. The hydrogen energy hub thus plays a critical role in modernizing and optimizing the energy infrastructure by ensuring efficient energy management and contributing to the sustainability goals.

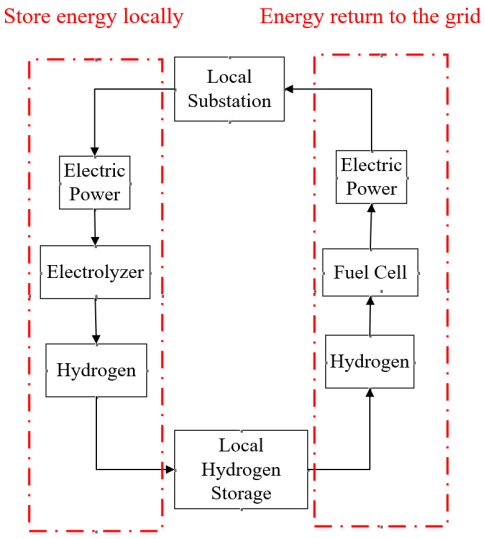

Fig. 2.1. Local energy exchange using the hydrogen energy hub.

EH-coupled SCUC (EH-SCUC) should consider the physical constraints of the local electrolyzers, fuel cells and hydrogen storage to store and release the energy at the same location. The hydrogen energy stored in the tank can be calculated as follows:

$$E_{nt} = E_{n,t-1} + \sum_{e \in E(n)} \eta_e P_{et} \cdot \Delta t - \sum_{f \in F(n)} P_{ft}/\eta_f \cdot \Delta t \quad (n \in N^H, t \in T). \qquad (2.19)$$

Moreover, the hydrogen energy stored in the hydrogen tank should always be positive, which is described as:

$$0 \le E_{nt} \le E_n^{\max} \ \ (n \in N^H, t \in T). \tag{2.20}$$

2.4 SCUC Models for Comparison

To gauge the operational performance of HETCS-coupled and EH-coupled power systems, two benchmark cases are established for comparison: (i) a relaxed SCUC (R-SCUC) model that assumes infinite electrical network capacity, in which no transmission congestion will occur and HETCS or EH is not included; (ii) a traditional SCUC (T-SCUC) that is a normal SCUC model for traditional power systems without HETCS or EH; The formulations of various SCUC models are concluded in Table 2.1. The power balance equation of the benchmark cases does not involve hydrogen facilities power consumption and generation, which is shown as:

$$\sum_{g \in G(n)} P_{gt} + \sum_{k \in K(n-)} P_{kt} - \sum_{k \in K(n+)} P_{kt} + \sum_{w \in W(n)} P_{wt} - \sum_{w \in W(n)} P_{wt}^{Cur} = d_{nt} \ \ (n \in N, t \in T). \tag{2.21}$$

Table 2.1 Formulations of Various SCUC Models

H-SCUC Model	EH-SCUC Model	R-SCUC Model	T-SCUC Model
Constraints (2.1) – (2.18)	Constraints (2.1) – (2.14), (2.17) – (2.20)	Constraints (2.1) – (2.6), (2.8) – (2.13), (2.21)	Constraints (2.1) – (2.13), (2.21)

2.5 Results Analysis

The proposed H-SCUC and EH-SCUC models for HETCS-coupled and EH-coupled power systems are tested, as well as the benchmark SCUC models, using the modified IEEE 24-bus system shown in Fig 2.2 [71]. In this test system, the HETCS consists of two electrolyzers and two fuel cells. The wind power plants are located on Bus 14 and Bus 22. The electrolyzers are also located on these two buses. The fuel cells are located on Bus 13 and Bus 15, where peak loads are over 200 MW. The electrolyzer conversion efficiency η_e is set to 0.8, and the fuel cell conversion efficiency η_f is set to 0.6. For EH-coupled test case, two energy hubs are located on Bus 14 and Bus 22 where wind farms sit. Although we did not set a maximum limit on the hydrogen storage capacity for simplicity, we set maximum limits on the power capacities of electrolyzers and fuel cells. For a fair comparison, we set the same capacities of electrolyzers and fuel cells for both the HETCS-coupled power system and EH-coupled power system.

The simulation is conducted on all four SCUC models at different wind penetration levels. We use python language with GLPK solving package to build and solve the cases. The simulation is performed on a desktop computer with Intel-i7 3.2 GHz CPU and 16 GB RAM. The SCUC simulation results for wind penetration level 10%, 30% and 50% are concluded in Table 2.2, Table 2.3 and Table 2.4 respectively. It is observed that HETCS can achieve cost saving, mitigate network congestion, lower load payment, and reduce the renewable curtailment and CO2 emissions substantially.

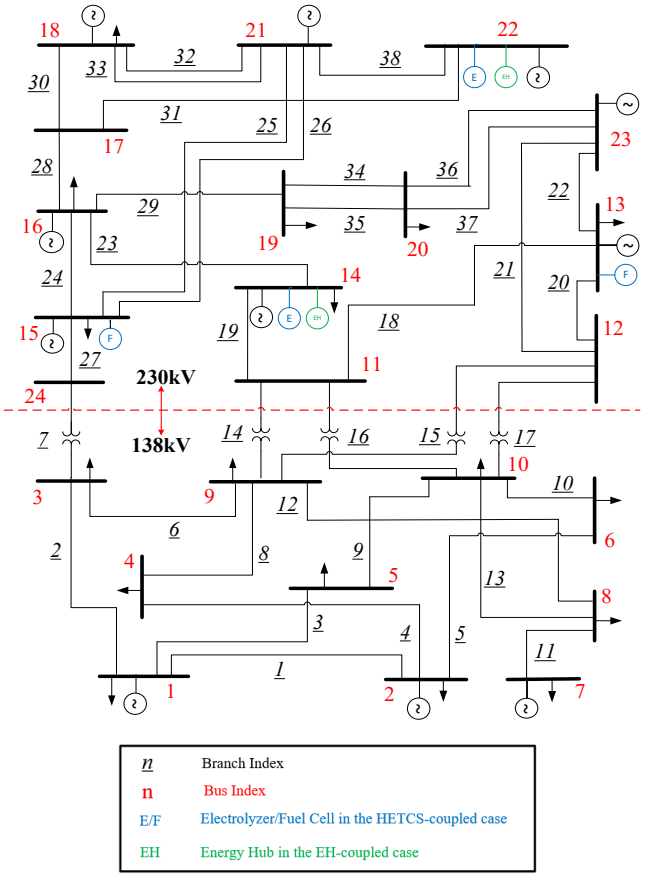

Fig. 2.2. The IEEE 24-bus system architecture (revised from [71]).

Table 2.2 Operational Performance Comparison for 10% Wind Penetration

	R-SCUC Model	T-SCUC Model	EH-SCUC Model	H-SCUC Model
Total Cost ($)	1,126,615.1	1,135,979.3 (100%)	1,128,001.2 (99.2%)	1,126,805.1 (99.1%)
Total Load Payment ($)	2,875,415.6	2,742,558.2 (100%)	2,899,254.7 (105.7%)	2,853,568.1 (104.0%)
Congestion Cost ($)	0	9,364.1 (100%)	1,386.0 (14.8%)	190.0 (2.0%)
RC (MWh)	0	0 (100%)	0 (100%)	0 (100%)
ANCLpH	N/A	1.3 (100%)	0.7 (53.8%)	0.7 (53.8%)
NCLPH	N/A	3 (100%)	1 (33.3%)	1 (33.3%)

Table 2.2 Continued

CO2 Emission (Lbs×10^6)	72.6	74.3 (100%)	72.6 (97.7%)	72.3 (97.3%)

"RC" denotes Renewable Curtailment; "ANCLpH" denotes Average Number of Congested Lines per Hour; "NCLPH" denotes Number of Congested Lines in the Peak Hour.

Table 2.3 Operational Performance Comparison for 30% Wind Penetration

	R-SCUC Model	T-SCUC Model	EH-SCUC Model	H-SCUC Model
Total Cost ($)	706,582.3	922,125.5 (100%)	712,789.2 (77.2%)	700,928.3 (76.0%)
Total Load Payment ($)	2,096,256.2	2,497,307.6 (100%)	2,144,122.2 (85.8%)	2,285,817.7 (91.5%)
Congestion Cost ($)	0	215,543.2 (100%)	6,206.8 (2.8%)	-5654.0 (-2.6%)
RC (MWh)	0	5,343.0 (100%)	335.8 (6.2%)	0 (0%)
ANCLpH	0	3.1 (100%)	1.7 (54.8%)	1.5 (48.3%)
NCLPH	0	4 (100%)	4 (100%)	4 (100%)
CO2 Emission (Lbs×10^6)	55.8	69.5 (100%)	60.8 (87.4%)	58.4 (84.0%)

"RC" denotes Renewable Curtailment; "ANCLpH" denotes Average Number of Congested Lines per Hour; "NCLPH" denotes Number of Congested Lines in the Peak Hour.

Table 2.4 Operational Performance Comparison for 50% Wind Penetration

	R-SCUC Model	T-SCUC Model	EH-SCUC Model	H-SCUC Model
Total Cost ($)	437,160.3	842,091.2 (100%)	632,472.1 (75.1%)	561,891.6 (66.7%)
Total Load Payment ($)	1,552,202.4	2,282,258.4 (100%)	1,844,646.7 (80.8%)	1,586,690.3 (69.5%)
Congestion Cost ($)	0	404,930.9 (100%)	195,311.8 (48.2%)	124,731.3 (30.8%)
RC (MWh)	0	14,096.6 (100%)	7,291.4 (51.7%)	5,007.3 (35.5%)
ANCLpH	0	3 (100%)	3 (100%)	3 (100%)

Table 2.4 Continued

NCLPH	0	3 (100%)	4 (133.3%)	4 (133.3%)
CO2 Emission (Lbs×10^6)	36.2	68.4 (100%)	58.8 (85.9%)	52.8 (77.1%)

"RC" denotes Renewable Curtailment; "ANCLPH" denotes Average Number of Congested Lines per Hour; "NCLPH" denotes Number of Congested Lines in the Peak Hour.

The wind power curtailment of different cases is plotted in Fig 2.3. From the plots, we can observe that the wind curtailment increases when the wind penetration level is high. The wind curtailment of the HETCS-coupled case is much lower than the traditional case and the EH-coupled case.

The carbon emission is calculated based on the scheduled generator output power in the SCUC results. The emission data of the generators is from [72]. The carbon emission for different wind penetration levels is plotted and shown in Fig 2.4. We can observe that HETCS-coupled case can significantly reduce the carbon emission. It reduces more carbon emission than EH-coupled case when the wind penetration level is high.

The total operational cost of different cases is shown in Fig 2.5. When the wind penetration level is higher, the total operational cost is lower. From the plot, we can observe that the HETCS case has lower operational cost than the EH-coupled case and the traditional case. The HETCS case can obviously save more cost when the wind penetration level is higher. The total operation cost of the HETCS-coupled case is even lower than the non-congestion case when the wind penetration level is 30%. The reason is that the HETCS can provide the function of energy storage, while no energy storage is included in the non-congestion case.

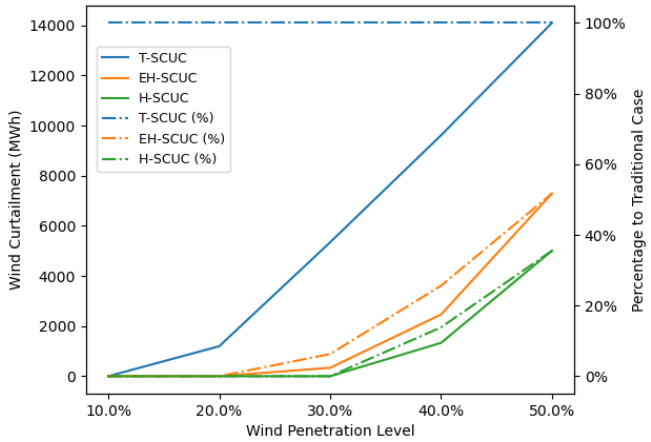

Fig. 2.3. Wind curtailment for different wind penetration level.

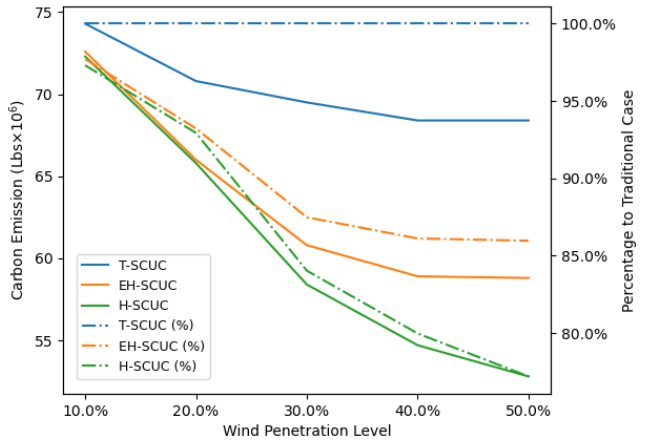

Fig. 2.4. Carbon emission for different wind penetration level.

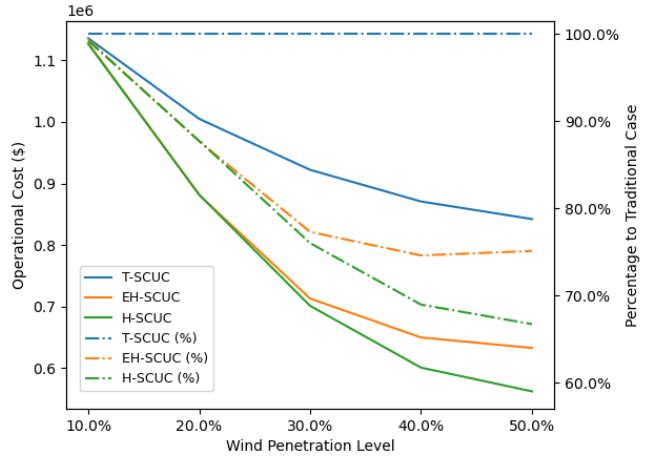

Fig. 2.5. Total operational cost for different wind penetration level.

The average LMPs of different cases is shown in Fig 2.6. The average LMP of the HETCS-coupled case is lower than the EH-coupled case for most wind penetration scenarios. Besides, the average LMP of HETCS-coupled case is much lower than the traditional case.

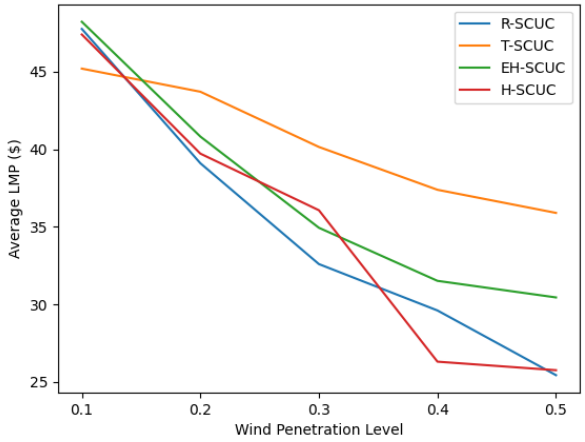

Fig. 2.6. Average LMP for different wind penetration level.

2.6 Site Selection of Fuel Cells

The P2H and H2P facilities should be placed at proper locations to ensure the HECTS-coupled power system can perform well. To find the suitable locations of fuel cells, we conduct the H-SCUC simulations on the HETCS-coupled systems with different fuel cell locations. Based on the load distribution of the IEEE 24-bus system, three fuel cell site selection cases are compared: (i) the fuel cells are located at the high-loaded buses. Bus 13 and Bus 15 are selected where peak loads are over 200 MWh. It's the HETCS-coupled case in the various SCUC comparison; (ii) the fuel cells are located at the center of load area. In the IEEE-24 bus system, the 138 kV area has more loads than the 230 kV area. Bus 4 and Bus 5 are selected in this case; (iii) the fuel cells are located at the bridges between the generation area and the load area. Bus

9 and Bus 10 are selected in this case. For fair comparison, the electrolyzers are located at Bus 14 and Bus 22 where wind farms sit in all above cases. Besides, we select the EH-coupled case which the fuel cells and electrolyzers are located at Bus 14 and Bus 22 as the benchmark case. The simulation results are shown in Table 2.5 and Table 2.6.

Table 2.5 Wind Curtailment of Different Fuel Cell Site Selection Cases Under Different Wind Penetration Levels

	10% Wind (MWh)	20% Wind (MWh)	30% Wind (MWh)	40% Wind (MWh)	50% Wind (MWh)
EH-coupled Case (Benchmark)	0	0	335.8 (100%)	2544.5 (100%)	7291.4 (100%)
Site Selection Case 1	0.0	0.0	0.0	1331.8 (52.3%)	5007.3 (68.6%)
Site Selection Case 2	0.0	0.0	0.0	1332.7 (52.3%)	4270.8 (58.5%)
Site Selection Case 3	0.0	0.0	0.0	1339.1 (52.6%)	4303.2 (59.0%)

Table 2.6 Total Cost of Different Fuel Cell Site Selection Cases

	10% Wind (MWh)	20% Wind (MWh)	30% Wind (MWh)	40% Wind (MWh)	50% Wind (MWh)
Table 2.6 Continued.					
EH-coupled Case (Benchmark)	$1.128M (100%)	$0.882M (100%)	$0.712M (100%)	$0.651M (100%)	$0.632M (100%)
Site Selection Case 1	$1.126M (99.8%)	$0.881M (99.9%)	$0.700M (98.3%)	$0.600M (92.0%)	$0.561M (88.8%)
Site Selection Case 2	$1.126M (99.8%)	$0.880M (99.8%)	$0.699M (98.1%)	$0.597M (91.6%)	$0.549M (86.8%)
Site Selection Case 3	$1.126M (99.8%)	$0.881M (99.8%)	$0.700M (98.2%)	$0.594M (91.1%)	$0.544M (86.1%)

The simulation result shows that different fuel cell locations may not influence the HETCS-coupled power system performance when wind penetration is low. When wind penetration is 40% or more, the proper selection of fuel cells can considerably reduce renewable curtailment and the total cost. Compared to random selection of high-loaded buses, locating the fuel cells at the center of load area or the bridges between the load area and generation area is more likely to attain better performance of HETCS-coupled systems. Determining the best P2H and H2P locations is a complicated problem, and it needs further thorough investigation in future.

2.7 Summary

Power systems with high renewable penetration can significantly benefit from coupling with the Hydrogen Energy Transmission and Conversion System (HETCS). The HETCS integrates a hydrogen network, Power-to-Hydrogen (P2H), and Hydrogen-to-Power (H2P) facilities, enabling both energy transfer and storage in the form of hydrogen. This study proposes a unit commitment model for HETCS-coupled power systems to evaluate their operational performance. To provide a comprehensive analysis, the non-congestion case, traditional case, and Energy Hub (EH)-coupled case are developed for comparison.

Simulation results indicate that HETCS and EH can considerably reduce renewable curtailment once the renewable penetration exceeds 20%. The system also shows improvements in other operational metrics, such as total operational cost, Locational Marginal Prices (LMPs), and carbon emissions, suggesting that HETCS and EH are a promising solution for power systems with high levels of renewable

energy. For instance, the integration of EH helps mitigate the intermittency issues associated with renewable generation by allowing excess energy to be converted into hydrogen and stored, which can later be converted back to electricity as needed. This capability not only reduces curtailment but also alleviates congestion in the power grid, leading to lower operational costs and emissions.

The study employs a modified IEEE 24-bus system for simulation, demonstrating the feasibility and benefits of the proposed HETCS model. At varying levels of wind penetration (10%, 30%, and 50%), HETCS consistently outperforms traditional and EH-coupled systems in terms of cost savings, reduced congestion, and lower emissions. For example, at 50% wind penetration, HETCS reduces the total cost to 66.7% and cuts renewable curtailment to 35.5% compared to the values observed in the traditional system and daily operation strategy.

While this research confirms the advantages of HETCS-coupled power systems, it also highlights the need for detailed modeling of HETCS in future studies. Further investigation into optimal placement of P2H and H2P facilities and comprehensive cost-benefit analyses will be crucial for practical implementation. The findings underscore the potential of HETCS to enhance the integration of renewable energy sources, paving the way for more sustainable and efficient power systems.

3. SCHEDULING OF SEASONAL HYDROGEN STORAGE

3.1 Literature Review

Energy storage systems (ESS) have emerged as a crucial technology to address the intermittency and spatial distribution challenges of renewable energy. Studies have demonstrated that ESS can significantly improve grid reliability and efficiency by providing backup power, balancing supply and demand, and reducing curtailment. Among the various types of energy storage technologies, batteries and electric vehicles have been extensively studied and implemented to integrate with the grid and mitigate issues caused by renewable variability. In addition to hydrogen storage, other advanced energy storage technologies are being researched to complement renewable energy integration. For instance, flywheel energy storage, as discussed by [73], offers high power density and rapid response times, making it suitable for frequency regulation and short-term energy balancing. Similarly, supercapacitors, as highlighted by [74], provide high efficiency and long cycle life, making them ideal for applications requiring frequent charge-discharge cycles.

However, hydrogen storage is increasingly recognized as one of the most promising technologies for large-scale energy storage. Hydrogen can be stored in different forms, including gas cylinders, liquid tanks, absorptive materials, and interstitial sites in host metals, offering diverse options for grid-scale. Large-capacity hydrogen storage is essential for grid-scale operations, and one of the most viable methods for achieving this is through the use of salt caverns. The renewable energy production and load demand exhibit distinct seasonal patterns due to varying

environmental and human factors. For instance, solar energy generation peaks during summer months when sunlight is abundant, whereas wind energy production may be higher in winter due to stronger and more consistent wind patterns. Conversely, the load demand also fluctuates with seasons; it generally increases in winter and summer due to heating and cooling requirements respectively, and decreases during milder spring and autumn months. These seasonal variations necessitate a long-term cross-season energy management system to balance supply and demand efficiently, ensuring reliable power grid operation throughout the year.

In the research conducted by [75], methods and design aspects of salt caverns for large-scale hydrogen storage were investigated. The study highlighted the feasibility and technical considerations of using salt caverns to store significant volumes of hydrogen, providing a stable and secure storage solution. Further research by [76] and [77] explored the practical application of salt caverns in energy systems, demonstrating their potential to support large-scale renewable integration.

Despite the advancements in hydrogen storage technologies, there is a notable gap in the literature regarding long-term management and operation strategies for these systems. For instance, [78] developed a mathematical model for seasonal hydrogen storage within multi-energy systems, addressing the need for effective seasonal energy management. The model can handle uncertainties in generation and load, but the practical implementation and computational efficiency of the model in real-world scenarios remain a challenge. Another study by [79] in 2020 examined the annual management of power grids coupled with hydrogen and heat systems,

highlighting the complex interactions and optimization required for integrated energy systems.

Moreover, recent studies have started to explore the economic and environmental benefits of hydrogen storage. For example, [80] conducted a comprehensive analysis of the cost-effectiveness and environmental impact of integrating hydrogen storage with renewable energy sources. The findings suggest that hydrogen storage not only enhances grid stability but also contributes to reducing greenhouse gas emissions and dependency on fossil fuels.

3.2 Annual Scheduling of EH-coupled Power Systems

In a power grid integrated with energy hubs (EHs), electrical and hydrogen energy can be exchanged at the nodes where these hubs are situated. Regarding power grid operation, surplus electrical energy can be stored as hydrogen and later converted back to electricity when required. Since salt caverns are capable of storing energy for extended periods, EHs can store hydrogen during low-load seasons and convert it back to electrical energy during high-load seasons. Additionally, EHs can store hydrogen during periods of high renewable energy production and release it during periods of low renewable production.

To effectively manage such a system, EH-coupled renewable power grids must incorporate electrical-hydrogen exchange constraints for both short and long time periods. The annual scheduling model (ASM) ensures that seasonal storage provides long-term temporal flexibility, balancing renewable production and load demands throughout the year. Furthermore, it helps mitigate the short-term

intermittency and fluctuations inherent in renewable energy production, thus enhancing the overall stability and reliability of the power grid.

3.2.1 Annual Scheduling Model Formulation

To consider the short time period electrical-hydrogen exchange operations, the proposed ASM uses four typical days to describe the daily operations in four quarters. Specifically, we assume the renewable generation and load profiles are the same for all days in a quarter. Hence, the daily power system operations remain the same for all days in the quarter. The daily operation constraints considering different quarters are listed as follows:

$$P_g^{\min} u_{gqt} \le P_{gqt} \quad \forall g, q, t, \tag{3.1}$$

$$P_{gqt} + r_{gqt} \le P_g^{\max} u_{gqt} \quad \forall g, q, t, \tag{3.2}$$

$$0 \le r_{gqt} \le R_g^{10} u_{gqt} \quad \forall g, q, t, \tag{3.3}$$

$$\sum_{m \in G} r_{mqt} \ge P_{gqt} + r_{gqt} \quad \forall g, q, t, \tag{3.4}$$

$$P_{kqt} = \theta_{kqt} / x_k \quad \forall k, q, t, \tag{3.5}$$

$$-P_k^{max} \le P_{kqt} \le P_k^{\max} \quad \forall k, q, t, \tag{3.6}$$

$$0 \le P_{wqt}^{Cur} \le P_{wt} \quad \forall w, q, t, \tag{3.7}$$

$$-R_g \le P_{gqt} - P_{g,q,t-1} \le R_g \quad \forall g, q, t \ge 2, \tag{3.8}$$

$$v_{gqt} \ge u_{gqt} - u_{g,q,t-1} \quad \forall g, q, t \ge 2, \tag{3.9}$$

$$v_{gqt} \in \{0,1\} \quad \forall g, q, t, \tag{3.10}$$

$$\text{and } u_{gqt} \in \{0,1\} \quad \forall g, q, t. \tag{3.11}$$

The generator power maximum and minimum power limits are shown in Constraints (3.1) – (3.2). Besides, the generator reserve's ramping limit and minimum reserve constraint are shown in Constraints (3.3) – (3.4). Constraints (3.5) is the DC power flow equation, and Constraints (3.6) represents the transmission line power limits. Since this study focuses on grids with high renewable penetration level, the curtailment of renewables is modeled using Constraints (3.7). The generator ramping limit is represented by Constraints (3.8). The relationship of the two binary variables v_{gqt} and u_{gqt} is shown in Constraints (3.9).

The nodal power balance equation in the EH coupled grids should include the electrical power generated or consumed by the fuel cells and electrolyzers. Besides, renewable generation and curtailment are also included in the equation. The nodal power balance equation can be expressed as

$$\sum_{g\in G(n)} P_{gqt} + \sum_{k\in K(n-)} P_{kqt} - \sum_{k\in K(n+)} P_{kqt} + \sum_{w\in W(n)} P_{wqt} - \sum_{w\in W(n)} P_{wqt}^{Cur} + \sum_{f\in F(n)} P_{fqt} = d_{nqt} + \sum_{e\in E(n)} P_{eqt} \quad \forall n, q, t. \tag{3.12}$$

The fuel cells and electrolyzers have maximum power capacity, which is described by

$$0 \le P_{eqt} \le P_e^{\max} \quad \forall e, t \tag{3.13}$$

$$\text{and } 0 \le P_{fqt} \le P_f^{\max} \quad \forall f, t. \tag{3.14}$$

The same daily operation will repeat for all days in the quarter. Following constraints involved the last hour of the previous day and the first hour of the current

day. Constraint (3.15) is the generator ramping rate constraint between the days in the same quarter, and can be expressed as

$$-R_g \leq P_{g,q,1} - P_{g,q,24} \leq R_g \quad \forall g, q. \tag{3.15}$$

Constraint (3.16) is the binary variable constraint for the two connecting hours between the days and it is given by

$$v_{g,q,1} \geq u_{g,q,1} - u_{g,q,24} \quad \forall g, q. \tag{3.16}$$

To consider the seasonal electrical-hydrogen exchange operation, the stored hydrogen at different quarters is modeled. The stored hydrogen at the specific hour and day can be calculated and expressed as

$$\begin{aligned} E_{nqtd} = E^0_{n,q} + \sum_{t' \in T^D} \left(\sum_{e \in E(n)} \eta_e P_{eqt'} \cdot \Delta t - \sum_{f \in F(n)} P_{fqt'} / \eta_f \cdot \Delta t \right) * (d-1) \\ + \sum_{t'' \in T^P(t)} \left(\sum_{e \in E(n)} \eta_e P_{eqt''} \cdot \Delta t - \sum_{f \in F(n)} P_{fqt''} / \eta_f \cdot \Delta t \right) \quad \forall n, q, t, d, \end{aligned} \tag{3.17}$$

where E_{nqtd} is the hydrogen energy stored at bus *n* at period *t* for day *d* in Quarter *q*. $E^0_{n,q}$ is the initial hydrogen energy stored at bus *n* for Quarter *q*. The second addition term on the right-hand side is the total hydrogen energy generated or consumed in the previous days of the quarter. T^D is the set of all hours in a day. P_{eqt} and P_{fqt} are the power generated or consumed by the electrolyzers and fuel cells. The third addition term on the right-hand side calculates the accumulated hydrogen energy generated or consumed in the previous hours of the day. $T^P(t)$ is the set of hours in a day which are earlier than hour *t*.

The initial stored hydrogen energy in a quarter equals the stored hydrogen energy in the last hour of the last day in the previous quarter. It is given by

$$E_{n,q}^{0} = E_{n,q-1,24,90} \quad \forall n, q \geq 2. \tag{3.18}$$

Besides, we assume the stored hydrogen energy remains the same after the one-year operation, which can be expressed as

$$E_{n,4,24,90} = E_{n,1}^{0} \quad \forall n. \tag{3.19}$$

With all the above constraints, the objective of the annual operation is to minimize the total operation cost including generator operational cost, startup cost, and no-load cost. We assume each quarter contains 90 days. The objective function is given by

$$\min \sum_{g \in G} \sum_{q \in Q} \sum_{t \in T} \left(c_g P_{gqt} + c_g^{NL} u_{gqt} + c_g^{SU} v_{gqt} \right) * 90. \tag{3.20}$$

Based on the above statement, the ASM for EH coupled grids includes Constraints (3.1) – (3.20).

3.3 Benchmark Model for Grids Without EHs

To analyze the performance and benefits of the EH coupled power grids using ASM, we also develop the ASM for the traditional grids without EHs. Compared to EH coupled grids, traditional grids do not have electrical-hydrogen exchange. Hence, the difference between the ASM for EH coupled grids (EH-ASM) and the ASM for traditional grids (T-ASM) is that no hydrogen related constraints are included in the T-

ASM. The nodal power balance equation without P2H and H2P facilities can be expressed as

$$\sum_{g\in G(n)} P_{gqt} + \sum_{k\in K(n-)} P_{kqt} - \sum_{k\in K(n+)} P_{kqt} + \sum_{w\in W(n)} P_{wqt} - \sum_{w\in W(n)} P_{wqt}^{Cur} = d_{nqt} \quad \forall n, q, t. \tag{3.21}$$

The T-ASM includes Constraints (3.1) – (3.11), (3.15) – (3.16), (3.20) – (3.21).

3.4 Results Analysis

The modified IEEE 24-bus system is selected as the test case. The quarterly loads and wind production profiles are created which can simulate the actual hourly fluctuation in four typical days. Besides, the four quarters' profiles also show the seasonal fluctuation. For example, the loads in quarter 3 are higher than in other quarters. For EH coupled case, two energy hubs are located on bus 14 and bus 22. Since the wind farms sit on these two buses, the wind energy can convert into hydrogen energy and be stored. Each energy hub contains a pair of fuel cell and electrolyzer. The efficiency of fuel cells η_f is set to 0.6, and the efficiency of electrolyzers η_{e} is set to 0.8. The hydrogen storage at each energy hub has 5000 MWh maximum energy capacity. The benchmark case for T-ASM simulation is the same 24-bus system without EHs.

The proposed EH-ASM and benchmark T-ASM are implemented using Python with the pyomo package and GLPK solver. The simulation is performed on a desktop computer with Intel-i7 3.2 GHz CPU and 16 GB RAM.

Two scenarios with 20% and 50% wind penetration levels are considered in this simulation. The quarterly wind production profiles for four typical days at different wind penetration levels are created. Then, the EH-ASM and T-ASM simulation is run for these wind penetration scenarios. The simulation results for EH-ASM and T-ASM at 20% wind penetration level are shown in Table 3.1 and Table 3.2 separately.

Table 3.1 EH-ASM Simulation Result at 20% Wind Penetration Level

	Quarter 1	Quarter 2	Quarter 3	Quarter 4
Wind Curtailment (MWh)	0	0	0	0
Conventional Generation (MWh)	$3.52*10^6$	$3.82*10^6$	$4.8*10^6$	$3.56*10^6$
Average Power Flow Percentage (%)	39.3%	42.9%	42.3%	42.2%
Total Cost ($)	258.53M			

Table 3.2 T-ASM Simulation Result at 20% Wind Penetration Level

	Quarter 1	Quarter 2	Quarter 3	Quarter 4
Wind Curtailment (MWh)	0	0	0	0
Conventional Generation (MWh)	$3.45*10^6$	$3.67*10^6$	$4.75*10^6$	$3.45*10^6$
Average Power Flow Percentage (%)	41.0%	40.2%	42.4%	41.2%
Total Cost ($)	267.01M			

As shown in tables 3.1 and 3.2, neither the EH-ASM case nor the T-ASM case has to curtail any wind power at 20% wind penetration level. The conventional generation of the EH-ASM case is higher than the T-ASM case due to the losses in energy conversion between hydrogen and electricity. However, the total operation cost of the EH-ASM is about 3.17% lower than the T-ASM case. Since the proposed

ASMs model the daily operation of the typical days, the hourly grid operation condition is also obtained from the ASM simulation. The hourly conventional generation at 20% wind penetration level for 4 typical days is shown in Figs. 3.1– 3.4. The conventional generation curve of EH-ASM has fewer high value periods, which means the grid does not need to start more expensive generators to meet these high generation periods. The reason is that the EH-ASM can optimize the hourly electrical and hydrogen energy exchange operation to reduce the operation cost. It indicates that hydrogen storage can benefit the renewable power grid even when the renewable penetration level is not very high.

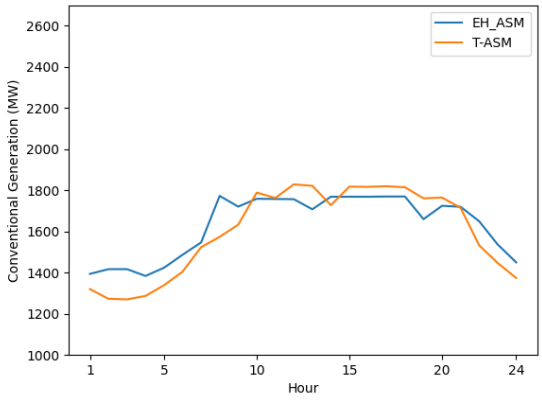

Fig. 3.1. The conventional generation in Quarter 1 at 20% wind penetration level.

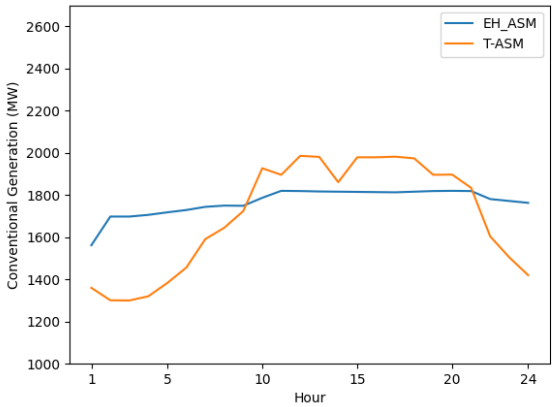

Fig. 3.2. The conventional generation in Quarter 2 at 20% wind penetration level.

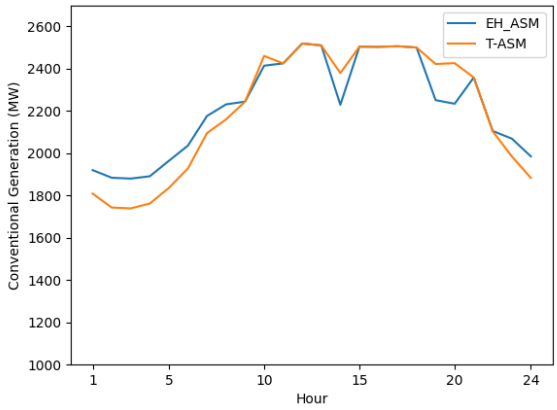

Fig. 3.3. The conventional generation in Quarter 3 at 20% wind penetration level.

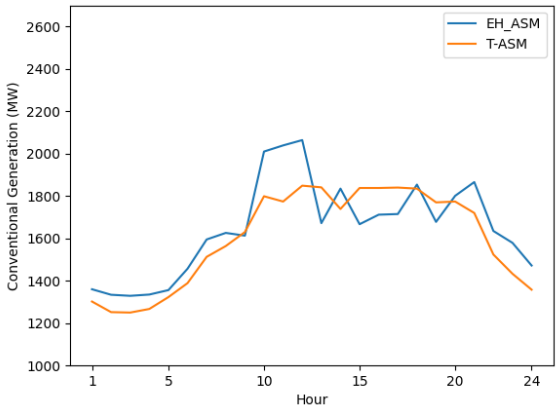

Fig. 3.4. The conventional generation in Quarter 4 at 20% wind penetration level.

The simulation results for EH-ASM and T-ASM at 50% wind penetration level are shown in Tables 3.3 and 3.4. From these two tables, we can observe that the EH-ASM case has lower wind curtailment and total operation cost than the T-ASM case. Since the wind generation is large, the hydrogen storage cannot store all the wind energy. Therefore, wind curtailment still occurred in the EH-ASM case. However, hydrogen storage can store wind energy in daily operation and reduce the conventional generation. Due to the above reasons, the performance of the EH-ASM case is better than the T-ASM case. To be noticed, the total hydrogen storage in the EH-ASM case is 10,000 MWh (two 5,000 MWh hydrogen storage on the EHs), which is the common

salt cavern storage capacity. A larger hydrogen storage capacity may enhance the performance of the EH-ASM case.

Table 3.3 EH-ASM Simulation Result at 50% Wind Penetration Level

	Quarter 1	Quarter 2	Quarter 3	Quarter 4
Wind Curtailment (MWh)	$2.13*10^5$	$5.27*10^5$	$7.15*10^5$	$2.88*10^5$
Conventional Generation (MWh)	$2.68*10^6$	$3.01*10^6$	$4.14*10^6$	$2.52*10^6$
Average Power Flow Percentage (%)	38.2%	41.5%	41.3%	39.6%
Total Cost ($)	193.59M			

Table 3.4 T-ASM Simulation Result at 50% Wind Penetration Level

	Quarter 1	Quarter 2	Quarter 3	Quarter 4
Wind Curtailment (MWh)	$2.17*10^5$	$5.49*10^5$	$7.33*10^5$	$3.01*10^5$
Conventional Generation (MWh)	$2.80*10^6$	$3.09*10^6$	$4.27*10^6$	$2.80*10^6$
Average Power Flow Percentage (%)	37.6%	40.0%	40.8%	39.9%
Total Cost ($)	211.61M			

In the above simulation, the efficiencies of electrolyzers and fuel cells are on the high end of their achievable range. The electrolyzer efficiency is set to 80% and fuel cell efficiency is set to 60%. The round-trip efficiency of electrical-hydrogen exchange is 48%. In more common cases, the round-trip efficiency of electrical-hydrogen exchange is about 37% [81]–[83]. Hence, the simulation for 37% round-trip efficiency at 50% wind penetration level is conducted. The total operational cost of EH-ASM is $195.37 million. For 48% round-trip efficiency, it is $193.59 million. Decreasing the round-trip efficiency from 48% to 37% increases the total cost by

roughly 1%. It indicates that the round-trip efficiency has less impact on the total cost when wind penetration level is high.

3.5 Summary

The proposed Annual Scheduling Model (ASM) for renewable power grids integrated with energy hub (EH) focuses on optimizing the exchange and storage of electrical and hydrogen energy across various seasons. This model leverages the flexibility and long-term storage capabilities of salt caverns to manage the variability and intermittency associated with renewable energy sources. The ASM utilizes four representative days to capture the typical conditions of each quarter, effectively reducing computational complexity while maintaining accuracy. For each representative day, the ASM integrates both power system and EH operations. It incorporates electrical constraints such as generation limits, transmission capacities, and power balance requirements. Additionally, it enforces electrical-hydrogen exchange constraints, specifically addressing the working power of fuel cells and electrolyzers. These constraints ensure that hydrogen generated from surplus electricity can be stored efficiently and reconverted into electricity when needed.

One of the critical aspects of the ASM is the calculation of stored hydrogen for each energy hub at every hourly interval throughout the year. This is achieved using an accumulative stored hydrogen equation, which tracks the hydrogen storage dynamics daily and seasonally. The model's ability to consider both intra-day and cross-season hydrogen exchange allows for better utilization of renewable resources

and enhances the grid's ability to handle seasonal fluctuations in energy demand and supply.

The efficacy of the proposed EH-ASM was demonstrated through simulations on the IEEE 24-bus system. The results revealed that the EH-ASM could effectively mitigate both daily and seasonal variations in loads and renewable generation. By optimizing the use of hydrogen storage, the model reduced the annual operational costs and minimized renewable curtailment. For instance, in scenarios with 20% wind penetration, the EH-ASM showed a 3.17% reduction in total operation cost compared to traditional scheduling models without EHs, despite higher conventional generation due to energy conversion losses between hydrogen and electricity. Furthermore, at 50% wind penetration, the EH-ASM exhibited significant benefits in reducing wind curtailment and operational costs.

The study also examined the impact of round-trip efficiency of electrical-hydrogen exchange on total operational costs. With an ideal efficiency of 48%, the EH-ASM's total cost was $193.59 million, whereas reducing the efficiency to 37% only increased the cost by 1% to $195.37 million. This finding suggests that while round-trip efficiency is an important factor, its impact on total costs diminishes at higher renewable penetration levels.

Overall, by providing both daily and seasonal flexibility, hydrogen storage can address the intermittency and spatial mismatches of renewable energy sources, ensuring a more stable and cost-effective grid operation.

4. POWER SYSTEM TEST CASE FOR SIMULATION-BASED STUDIES

4.1 Literature Review

The Simulation-based studies in power systems frequently utilize publicly available synthetic test cases as benchmark systems due to the scarcity of real system data. These encompass a broad spectrum of research areas, including power system operation and planning [56][69][84], stability and reliability [56][87]. Generally, a test case includes all the relevant information for generation, transmission and load. The commonly used test cases are IEEE and CIGRE benchmarks such as the IEEE 73-bus system and CIGRE medium voltage system [88]. Besides these small-scale test power systems, very few large-scale real power system cases are publicly accessible due to the confidentiality of the power industry. To meet the research requirements of large-scale test cases without access of real large systems, some synthetic test cases are created that resemble the actual systems based on their electrical characteristics. The Polish 2746-bus system is created based on the real power system of Poland [89]. The synthetic grids utilizing the footprint of the western, northeastern, and eastern U.S. regions have been created, and each grid contains more than ten thousand buses [90]. Most existing test cases provide the technical details for steady-state analysis, such as power flow or transient-state analysis such as stability simulation. However, these test cases only provide the data for a certain snapshot in time. The long-term time series system profiles are not provided in these test power system cases. There is a lack of test systems with profiles spanning long continuous periods; such test cases can be

used to demonstrate the versatility of renewable production, load and other grid components and enable more comprehensive grid operations and planning studies. Moreover, the recent trend of applying machine learning (ML) approaches in power systems also requires a test power system with time-series spatio-temporally correlated data over multiple years for ML model training and validation.

Power systems will increasingly confront climate-related challenges in the 21st century [91]. However, despite these emerging challenges, the impact of climate and weather on power system performance and potential mitigation strategies has yet to be explored comprehensively. Furthermore, simulations such as security-constrained unit commitment (SCUC) for large-scale power systems require extensive computational resources. A specifically synthetic test case is required to effectively support simulation-based research with accurate current and future grid profiles considering renewable production, climate and weather impacts. It is essential for future planning studies of high-renewable penetration grids that utilize simulation-based techniques, such as the planning of the hydrogen-integrated transmission network.

4.2 Creation of TX-123BT Current Profiles

A large-scale synthetic test case, the Texas 123-bus backbone transmission (TX-123BT), is developed to mirror actual systems like ERCOT with detailed weather-dependent grid profiles. It offers a dataset with 5-year time span from 2017 to 2021 at one-hour resolution, enabling enriched analysis and validation in diverse power system studies including hydrogen integration studies. TX-123BT is

specifically designed to encompass only the backbone of the high-voltage transmission network. This focus helps manage computational demands efficiently. The created TX-123BT system, including its network and generator configurations, spatio-temporally correlated grid profiles and the associated historical weather data, has been released with free access [92]–[93]. The historical weather data at all bus locations extracted from NLDAS-2 dataset [94]–[95] are also made available, including temperature, solar irradiance, and wind speed. The weather data and created grid profiles are organized by locations, and the associated Geographic Information System (GIS) files are also provided. The TX-123BT includes both the hourly and daily dynamic line rating (DLR) profiles. The performances of these two DLR techniques are examined and compared. SCUC is conducted on the daily profiles for validation. The numerical results including market results are shown to be consistent with the actual ERCOT historical data. The flexibility provided by hydrogen facilities for grid applications is investigated, and suitable hydrogen facilities are included as additional components in TX-123BT. The hydrogen integration simulations are conducted to prove the necessity and importance of incorporating weather-dependent renewable production profiles.

4.2.1 System Design Workflow and Profile Scenarios

The aim of this study is to create a power system test case providing both grid configurations and long-term consecutive profiles, instead of a single time snapshot like other test cases. After grid configurations including the network topology and generator parameters are determined, the long-term profiles are created

based on the configurations and parameters of the transmission and generation components. The workflow of TX-123BT creation is illustrated in Fig. 4.1.

Firstly, we determine the infrastructure details for power system facilities, including the locations and parameters for transmission lines, substations, thermal generators and renewable power plants. The geographic distribution of the TX-123BT transmission network is based on the 345 kV high voltage transmission lines in Texas [96] and is shown in Fig. 4.2. For thermal power plants, the output capacity, ramping rate, and generation costs are crucial for dispatching decisions to ensure reliability while minimizing costs. For renewable power plants such as wind farms, the configurations including locations, wind turbine blade length, and the overall plant capacity are required for creating the wind production pro-files for a long period. We consider their geographic distribution and reasonable capacity range of generators with different fuel types based on the ERCOT fuel mix and EIA generation data. In TX-123BT, the generator and transmission network are located coordinately similar to the real actual power systems.

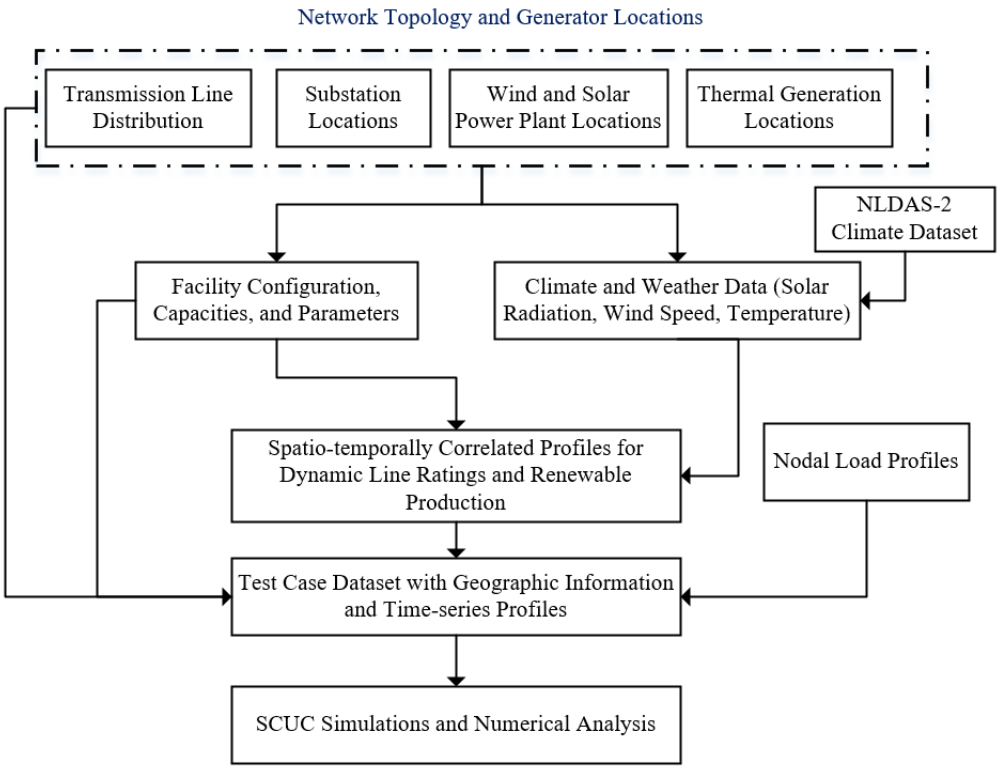

Fig. 4.1. The workflow of TX-123BT test case creation.

Fig. 4.2. Illustration of the 123-bus transmission network topology.

Secondly, we develop weather-dependent profiles based on facility configurations and the historical weather data at the locations of these facilities. Both hourly and daily line ratings are calculated based on the transmission line conductor types, sizes, reactance, as well as the temperature and wind speed data on two terminals of the lines. Wind production is calculated based on the wind turbine parameters such as blade length, cut-in and cut-out wind speed and the estimated wind speed at the wind turbine height. Solar production is calculated based on the solar panel parameters and the estimated solar radiation for the effective wavelength on the panel.

Thirdly, we create the time-sequential load profiles based on the ERCOT historical load data on different weather zones. Then, we organized the above-mentioned profiles and made it readiness for power system both short-term and long-term analysis such as SCUC and long-term transmission planning.

To validate the designed TX-123-BT system, we ran SCUC for the daily profiles in the 5 years and compared the obtained electricity prices with the actual ERCOT electricity market. We also evaluated the transmission network congestion of the TX-123BT during peak load scenarios and analyzed the grid performance with hourly and daily line ratings.

The TX-123BT with high resolution renewable production profiles is utilized to study the configurations and performance of hydrogen facilities in high renewable penetration grids. It is also an example to demonstrate the necessity of the TX-123BT spatio-temporally correlated profiles. Specifically, we have created the TX-123BT

profiles coupled with hydrogen hubs and Hydrogen Energy Transmission and Conversion System (HETCS) separately. The grid operation conditions with different hydrogen solutions are evaluated and compared, with the help of detailed renewable production profiles provided by TX-123BT.

4.2.2 Conventional Generation Profiles

A. The Generation Fuel Mix:

Major generation fuel types in the ERCOT system are natural gas, wind, coal, nuclear, and solar per [96]–[97]. The generation fuel composition may vary in different regions of ERCOT. For example, most wind generators are in the northwest of Texas due to the wind source distribution. The TX-123BT is created to have a very similar system-wide as well as region-wide generation fuel mix with the actual ERCOT system. Based on the generation characteristics of various fuel types for different weather zones and the whole ERCOT [98]–[100], fuel types of the generators in the TX-123BT system are assigned accordingly and the generator's power capacity is within the capacity range of the corresponding type of generators. Based on the data provided by Energy Information Administration (EIA) [99], ten hydro power plants, each of which is over 10 MW, are also added to the generation profiles.

The statistical data of TX-123BT generation profiles are shown in Table 4.1 and Table 4.2. The system-wide generation fuel mix (last row in Table II) is similar to the actual fuel mix provided by ERCOT [101]. It is worth noting that the renewable generation capacity has grown rapidly in ERCOT. We have adjusted the wind and solar capacity to match the actual ERCOT renewable capacity in 2019.

B. Conventional Generator Costs & Operation Parameters:

1) Coal & Natural Gas Generator

The quadratic function is used to model the thermal power plant's operation cost c_g and can be expressed as

$$c_g = C_0 + C_1 * P + C_2 * P^2, \tag{4.1}$$

where the coefficients C_0, C_1 and C_2 of typical coal generators and natural gas generators are determined per [102].

The generator startup cost c_g^{SU} can be calculated and expressed as

$$c_g^{SU} = \eta_g^{SU} * P_g^{Max} * C^F + P_g^{SU} * C_g^O, \tag{4.2}$$

where P_g^{Max} is the generator active power capacity, η_g^{SU} is the startup fuel per unit capacity, C^F is the fuel price, P_g^{SU} is the startup power and C_g^O is another startup cost related to the required startup power.

Table 4.1 Total Number of Different Fuel Type Generators

Weather Zone	Natural Gas	Wind	Coal	Solar	Nuclear	Hydro
Coast	31	0	2	8	1	0
East	15	0	2	0	0	0
Far West	4	11	0	17	0	0
North	4	9	1	6	0	1
North Central	14	10	4	9	1	1
South	11	18	1	3	0	1
South Central	29	0	3	23	0	6
West	5	34	0	6	0	1
Total	113	82	13	72	2	10

Table 4.2 Total Capacities (MW) of Different Fuel Type Generators

Weather Zone	Natural Gas	Wind	Coal	Solar	Nuclear	Hydro

Table 4.2 Continued

Coast	11925	0	2373	37	2709	0
East	6385	0	3089	0	0	0
Far West	3892	2341	0	1760	0	0
North	2236	3990	802	256	0	80
North Central	12093	1277	4529	42	2431	42
South	7480	6717	410	97	0	31
South Central	11075	0	3560	159	0	287
West	920	10157	0	131	0	58
Total	56006	24480	14761	2480	5139	498

The coal price used in creating the TX-123BT system is 1.78 $/MMBtu based on EIA [102]. The annual average natural gas price in Texas is 2.29 $\frac{\$}{Kft^3}$. As the natural gas heat content is set to be 1000 $\frac{Btu}{ft^3}$ [103], then the natural gas price becomes 2.29 $/MMBtu. Based on the above information, the total startup cost is calculated for the coal and natural gas generators in the TX-123BT test system. Tables 4.3 show the cost range for coal generators in TX-123BT.

In addition, the shutdown costs are calculated following [100]. The ramping rate, minimum off time, and maximum on time of coal and natural gas generators are obtained per [101]. The startup time and shutdown time are obtained from [104].

Table 4.3 Costs for Various Scale Coal Power Plants

Capacity (MW)	C0 ($/h)	C1 ($/h/ MW)	C2 ($\frac{\frac{\$}{h}}{MW^2}$)	Startup ($/Installed MW)	Shutdown ($/Installed MW)
0-75	0-238	18.28-19.98	0.0016	80-380	8-38
75-150	238-745				
150-350	745-1213				
>350	1213-3043				

2) Nuclear Power Plants

Texas has two nuclear power plants. Per expense of nuclear power plants [105], we assume the operation cost of the nuclear power plants is 17.44 $/MWh. The nuclear power plants are generally online most of the time. Most nuclear power plants require more than 12 hours to reach full operation, and they can ramp up or down in the load following mode [106].

3) Hydroelectric Power Stations

The average operation cost of hydroelectric power plants is 12.3 $/MWh per [107]. Hydroelectric power stations can ramp up rapidly and require much less time to startup and shutdown. As an example, hydroelectric power plants provided flexible ramping during the generation shortage in Texas in February 2021 [108]. Thus, we assume the startup and shutdown time, minimum on and off time of hydroelectric power stations are zeros.

4.2.3 Weather-dependent Spatio-temporally Correlated Renewable Power Production Profiles

A. The Weather-dependent Wind Model and Production Profiles:

The TX-123BT renewable production profiles depend on the weather data at the plant locations, and we obtain these data from NLDAS-2. The NLDAS-2 climate dataset includes the shortwave and longwave solar radiation, air temperature and wind speed near the ground surface at one-hour resolution. Since this study aims to create

the time-series profiles that resemble the ERCOT in the 5-year period from 2017-2021, the historical weather data for all the hours in the period are extracted.

In the ERCOT system, the full capacity up to the high sustained limit (HSL) of wind generation resources is considered available to be dispatched in the reliability unit commitment (RUC) [109]. However, ERCOT only provides limited data for the HSL in the current operating plan (COP), which is not the actual HSL. Instead of determining the wind hourly HSL for daily grid operations, we use the wind hourly production data [110] to create the wind profiles.

The available wind power output is calculated when wind speed is between the cut-in speed and rated-speed using the equations expressed by

$$P^{W,Max} = \frac{1}{2} \cdot \rho \cdot A \cdot V^3 \cdot C_p \tag{4.3}$$

$$\text{and } A = \frac{\pi}{4} \cdot D^2, \forall i, t, \tag{4.4}$$

where V is the wind speed, ρ is the air density, C_p is the wind turbine efficiency, A is the turbine blade swept area, and D is the turbine diameter. For all the wind turbines in the TX-123BT system, the cut-in speed is set to 3.5m/s, the rated speed is set to 13m/s, and the cut-out speed is set to 25m/s.

The extracted historical wind speed data in NLDAS-2 is the measured wind speed at 10m height and most wind turbines on land are about 80m high [111] to determine wind speed at 80m, we use log wind profile [112] to estimate the wind speed at the wind turbines' height. The equation for the log wind profile is

$$u(z_2) = u(z_1) \cdot \frac{\ln\left(\frac{z_2 - d}{z_0}\right)}{\ln\left(\frac{z_1 - d}{z_0}\right)}, \tag{4.5}$$

where the wind speeds at two different heights z_1 and z_2 are represented by $u(z_2)$ and $u(z_2)$ respectively. Zero-plane displacement *d* is the height that zero-wind speed is achieved because of flow obstacles. It can be approximated as 2/3 to 3/4 of the average height of the obstacles [111]. Roughness length z_0 is the roughness of the surface. Based on the terrain of Texas, z_0 is set to 0.3 and *d* is set to 6. The wind speed at 80m is about 2.13 times of wind speed at 10m.

To create more practical weather-dependent wind production profiles, the capacities and geographic locations of the wind power plants in the TX-123BT should be close to the actual ERCOT system. Thus, the wind plant capacities in the TX-123BT system are adjusted to match the actual ERCOT wind generation using the least square method, and can be described as follows:

$$\min \sum_h^H \left(\sum_i^{N^W} p_{i,h}^{W,Case} - p_h^{ERCOT}\right)^2, \tag{4.6}$$

$$P_{i,h}^{W,Case} = k_{i,h}^W \cdot C_i^W \cdot V_{i,h}^3 \quad \forall\, i \in N^W, h \in H, \tag{4.7}$$

$$k_{i,h}^W = k_{i,h+24}^W \quad \forall\, i \in N^W, h \in H, \tag{4.8}$$

$$-E_k^{max} \le k_{i,h}^W - k_{i,h-1}^W \le E_k^{\max} \quad \forall\, i \in N^W, h \in H, \tag{4.9}$$

$$-E_c^{max} \le C_i^W - C_i^{W0} \le E_c^{max} \; \forall\, i \in N^W, h \in H, \tag{4.10}$$

$$\text{and } C_i^W \ge 0 \quad \forall\, i \in N^W. \tag{4.11}$$

The least square method can adjust the wind power plant capacities in the TX-123BT to minimize the square error between the wind production of the TX-

123BT and the ERCOT per Equation (4.6). $p_{i,h}^{W,Case}$ is the power output of wind farm i in hour h in the TX-123BT. p_h^{ERCOT} is the total wind output power of the actual ERCOT system in hour h. Hour h is an hour in the period. The aggregated wind power production in a wind farm is related to the adjusted capacity of wind farm C_i^W and the wind speed $V_{i,h}$ per Equation (4.7).

The wind turbine coefficient k is a comprehensive coefficient considering various factors including the wind direction and wind turbine efficiency. The wind turbine coefficient k is assumed to be a constant for a specific wind turbine for each hour of the day per Equation (4.8). The changing magnitude of k is limited to E_k^{max}er two consecutive hours. Besides, the adjustment of the capacity for each wind farm in TX-123BT is less than the maximum error E_c^{max} per Equation (4.10). The adjusted wind capacity should be non-negative per Equation (4.11). The least square method can find the most realistic wind turbine coefficients and capacities for wind farms in the TX-123BT system.

The created wind production hourly time series profiles are compared to the corresponding real ERCOT wind production in 2019 in Fig. 4.3. The mean hourly wind power profile (within a day), averaged over 365 days in 2019, is compared to the actual ERCOT hourly statistics in Fig. 4.4. According to the comparison, we can conclude that the created wind production profiles are very similar to the actual situation. The hourly wind power production from seven wind farms at bus 119 on January 3, 2019, is illustrated in Fig. 4.5.

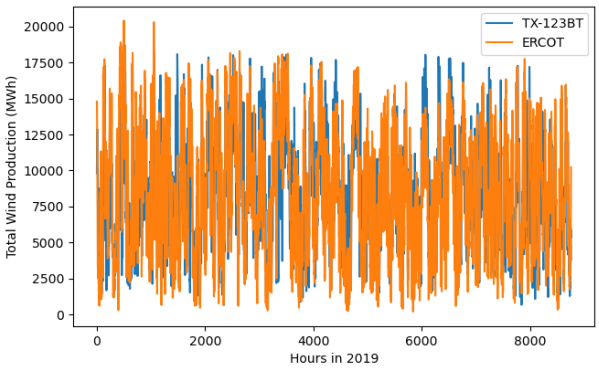

Fig. 4.3. Wind power production for all hours in 2019.

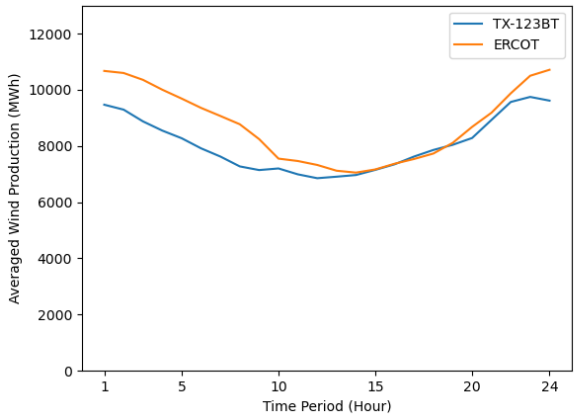

Fig. 4.4. Hourly wind power profiles comparison.

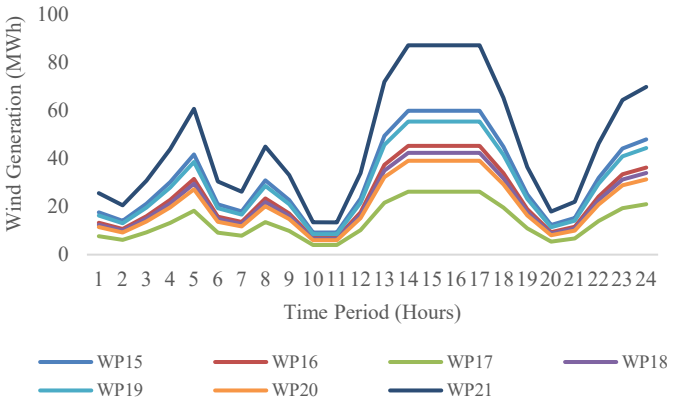

Fig. 4.5. Output power of seven wind plants (WP) on January 3, 2019.

B. The Weather-dependent Solar Model and Production Profiles:

A five-parameter single diode equivalent circuit is commonly used and suitable for PV cell, module and array [113], the operation condition variables (temperature, radiation, and air mass) are used in a five-parameter equation. Since we are mainly interested in the maximum available solar power output at different radiation and temperature, we can calculate the maximum power point [114] and expressed as

$$P_{mp} = \frac{E_e}{E_0} \cdot P_{mp0} \cdot [1 + \gamma \cdot (T_c - T_0)], \tag{4.12}$$

where P_{mp} is the maximum power output for the certain operation condition. E_e and T_c are the effective radiation and temperature on the solar cells respectively. P_{mp0} is the maximum power output at the standard testing condition (STC). E_0 and T_0 are the radiation and temperature at STC respectively. γ is the temperature coefficient that indicates the influence of the temperature on solar power transfer efficiency.

The NLDAS-2 provides the historical data for shortwave and longwave solar radiation flux downwards. Based on the widely used solar panel's spectral response range, we use the radiation flux downwards to estimate the effective solar radiation on the solar panels. We also estimate the solar cell temperature using the ambient air temperature at the corresponding solar panel.

Based on the processed weather data and solar power production model, the solar power production for all the solar farms in the TX-123BT system is calculated. The system-wide hourly solar production of the TX-123BT is compared with ERCOT solar production in 2022 (the historical data is not accessible). The hourly solar

productions averaged over all the days in Quarter 1 for the synthetic TX-123BT system and the actual ERCOT system are shown in Fig. 4.6. We can observe that the deviation is within a reasonable range. The hourly solar power production for four solar farms in TX-123BT is shown in Fig. 4.7.

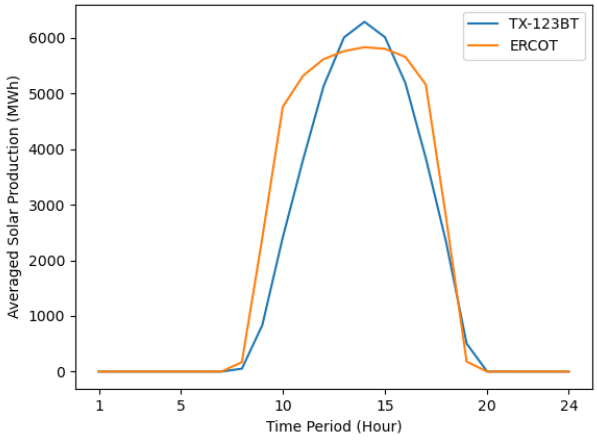

Fig. 4.6. Averaged hourly solar power production in Quarter 1.

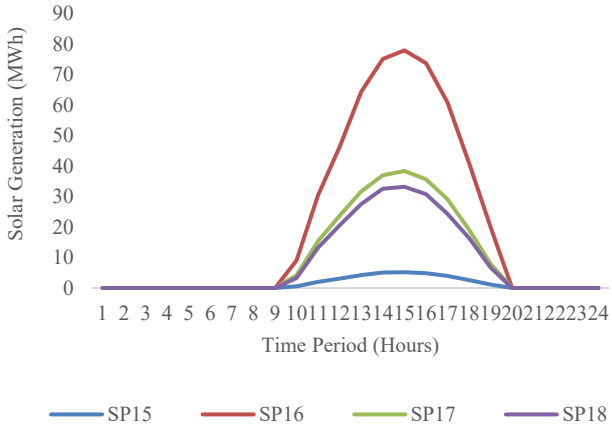

Fig. 4.7. Hourly power output of four solar plants (SP) on January 1, 2019.

4.2.4 Creation of Load Profiles

The ERCOT historical load data includes the hourly total load in each weather zone for all hours in different years. The hourly load profiles at the nodal

level are created for the TX-123BT system such that they match the total zonal load amount in each weather zone for each hour from 2017 to 2021. Part of the load profiles are illustrated in Table 4.4.

Table 4.4 Sample Load Profiles for Different Hours on December 31, 2019

Bus Number	Hour 1	Hour 5	Hour 9	Hour 13	Hour 17	Hour 21
Bus 1	96.51	102.39	118.19	91.76	84.25	96.28
Bus 2	97.86	103.56	116.47	95.4	87.29	97.41
Bus 3	171.3	172.01	173.67	161.79	158.4	165.91
Bus 4	198.59	202.18	231.79	213.28	208.4	212.48
Bus 5	25.58	24.5	28.54	28.53	28.73	28.21
Bus 6	606.36	641.1	754.35	608.1	555.7	613.43
Bus 7	42.61	45.05	53.01	42.73	39.05	43.11

4.2.5 Weather-Dependent Transmission Line Rating

The transmission line thermal capacity in the three-phase system can be calculated given the line ampacity and line voltage. The IEEE Std 738-2012 [115] is used to calculate ampacity of lines at different temperature, solar radiation and wind speed conditions. The detailed calculation is described as follows:

$$q_c + q_r = q_s + I^2 \cdot R\left(T_{\text{avg}}\right), \tag{4.13}$$

$$I = \sqrt{\frac{q_c + q_r - q_s}{R\left(T_{\text{avg}}\right)}}, \tag{4.14}$$

$$q_{c1} = K_{angle} \cdot [1.01 + 1.35 \cdot N_{Re}^{0.52}] \cdot k_f \cdot (T_s - T_a), \tag{4.15}$$

$$q_{c2} = K_{angle} \cdot 0.754 \cdot N_{Re}^{0.6} \cdot k_f \cdot (T_s - T_a), \tag{4.16}$$

$$K_{\text{angle}} = 1.194 - \cos(\varphi) + 0.194 \cdot \cos(2\varphi) + 0.368 \cdot \sin(2\varphi), \tag{4.17}$$

$$q_r = 17.8 \cdot D_0 \cdot \varepsilon \cdot \left[\left(\frac{T_s + 273}{100}\right)^4 - \left(\frac{T_a + 273}{100}\right)^4\right], \tag{4.18}$$

$$q_s = \alpha \cdot Q_{se} \cdot \sin(\theta) \cdot A', \tag{4.19}$$

$$\text{and } \theta = \cos^{-1}[\cos(H_c) \cdot \cos(Z_c - Z_l)]. \tag{4.20}$$

Equation (4.13) is the heat balance equation of the conductor. q_c is the convective heat loss. q_r is the radiated heat loss rate. q_s is the rate of solar heat gain. I is the current in the conductor and R(T_{avg}) is the conductor resistance at temperature T_{avg}, which is the average temperature in the conductor. Equation (4.13) can be transformed into Equation (4.14), which can be used to calculate the current in the conductor at the conductor maximum temperature. In Equation (4.15) – (4.17), q_{c1} and q_{c2} are the forced convection and the higher value of q_{c1} and q_{c2} will be used as the value of q_c. N_{Re} is the dimensionless Reynolds number. K_f is the thermal conductivity of air. T_s is the conductor surface temperature, and T_a is the ambient temperature. K_{angle} is wind direction factor and φ is the angle between the wind direction and the conductor axis. In Equation (4.18), the radiated heat loss is related to the diameter of the conductor D_0, the emissivity ε, the conductor surface temperature T_s, and ambient temperature T_a. The rate of solar heat gain can be calculated by Equation (4.19). α is the solar absorptivity. Q_{se} is total solar and sky radiated heat intensity corrected for the elevation. A' is the projected area of the conductor. θ is the effective angle of incidence of the sun's rays. In Equation (4.20), θ is determined by the altitude of the sun H_c, the azimuth of the sun Z_c, and the azimuth of the line Z_l.

There are three types of aluminum conductor steel reinforced (ACSR) conductors used for the transmission lines in the TX-123BT: Kiwi, Bobolink and Finch. Different types of ACSR conductors have different conductor diameters and

resistances versus temperature characteristics. The linear approximation determines the conductor resistance at a certain temperature, and can be expressed as

$$R(T_{\text{avg}}) = \left[\frac{R(T_{\text{high}}) - R(T_{\text{low}})}{T_{\text{high}} - T_{\text{low}}}\right] \cdot (T_{\text{high}} - T_{\text{low}}) + R(T_{\text{low}}), \qquad (4.21)$$

where $R(T_{\text{high}})$ and $R(T_{\text{low}})$ are the conductor resistance at temperature T_{high} and T_{low} respectively.

Although the extracted historical weather data have detailed nodal information at one-hour resolution, they do not perfectly meet the needs of transmission line calculation. Several assumptions are made as follows. First, the line ambient temperature is assumed to be the same as the temperature 2 meters above ground. Second, since most long-distance transmission lines are overhead lines and the transmission towers are generally 55-150 feet (16.8m-45.72m), the wind speed at the transmission line's height is estimated using the aforementioned log wind profile method. Third, the angle between the wind direction and the transmission line is assumed to be 45-degrees. The wind speed perpendicular to the conductor V_w can be calculated and given by

$$V_{wind} = \sqrt{{V_z}^2 + {V_m}^2} \qquad (4.22)$$

$$\text{and } V_w = V_{wind} * \sin(\theta). \qquad (4.23)$$

In Equation (4.22), V_z and V_m is the zonal and meridional wind speed extracted from NLDAS-2. V_{wind} is the composite speed, and θ is the angle between the wind turbine blade and wind direction.

The total heat intensity corrected for elevation Q_{se} is calculated and described as follows:

$$Q_s = A + B \cdot H_c + C \cdot {H_c}^2 + D \cdot {H_c}^3 + E \cdot {H_c}^4 + F \cdot {H_c}^5 + G \cdot {H_c}^6, \quad (4.24)$$

$$Q_{se} = K_{solar} \cdot Q_s, \quad (4.25)$$

$$\text{and } K_{solar} = A + B \cdot H_e + C \cdot {H_e}^2. \quad (4.26)$$

In Equation (4.24) – (4.26), Q_s is the total heat flux density by a surface at sea level. K_{solar} is the elevation corrective factor. *A*, *B*, *C*, *D*, *E*, *F*, and *G* are polynomial coefficients.

The total heat flux by the Earth's surface Q_s is assumed to be the summation of the downward shortwave radiation Q_{short} and longwave radiation Q_{long}, which are the data extracted from NLDAS. Radiation from the Earth's surface is omitted. Thus, Q_s can be calculated by

$$Q_s = Q_{short} + Q_{long}. \quad (4.27)$$

In the calculation, the environmental parameters are determined based on the actual Texas conditions. The altitude and azimuth of the sun at noon are used in the calculation. The altitude of the sun H_c is calculated based on the average latitude of Texas which is 30.5° N. The elevation of the conductor above the sea level H_e is set to Texas average elevation. For ACSR transmission lines, the common continuous operational maximum temperature is 90℃. The parameters for the Texas line ampacity calculation are listed in Table 4.5.

Table 4.5 Some Input Data for Texas Line Ampacity Calculation

Notation	Explanation	Value
H_c	The altitude of the sun	30.5

Table 4.5 Continued.

Z_c	The azimuth of the sun	180 deg
H_e	The elevation of conductor above sea level	520 m
ε	The emissivity	0.8
α	Solar absorption	0.8
μ_f	The air viscosity	2.04e-5
T_{film}	Average temperature of the boundary layer	70 °C
K_f	The thermal conductivity of air	0.0295W/(m-°C)
T_c	The conductor maximum temperature	90 °C

Dynamic line rating is an effective strategy in power system operations to fully utilize the available transmission capacity of the lines under various environmental conditions. In this paper, we have created two profiles using the daily DLR and the hourly DLR, respectively. The daily DLR profile has the same fixed line ratings for the entire day, which is used by many power system operators. We use the highest hourly temperature, solar radiation, and the lowest hourly wind speed as the environmental values in the daily line rating calculation. The daily line rating profiles are calculated for all the days in the 5-year period. The daily thermal ratings of line 15 during 2019 are shown as an example in Fig. 4.8.

The hourly line rating method captures the suitable line ratings for each hour in the daily operation. Each hour's temperature, solar radiation, and wind speed are used in the line rating calculation for the corresponding hour. Hourly line ratings are higher than the daily line rating in most instances. Hence, using hourly line rating can reduce operational costs and improve system operational efficiency. The hourly line

ratings are calculated for all the hours in the 5-year period. The hourly ratings of line 15 for different quarters are shown in Fig. 4.9.

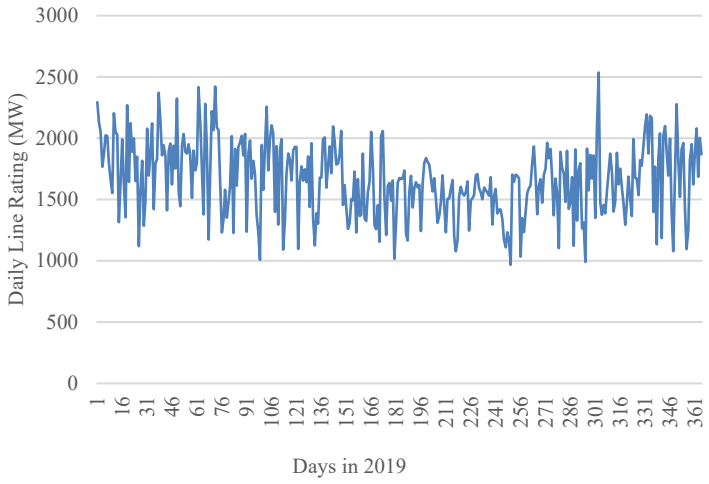

Fig. 4.8. The daily thermal ratings of line 15 during the year 2019.

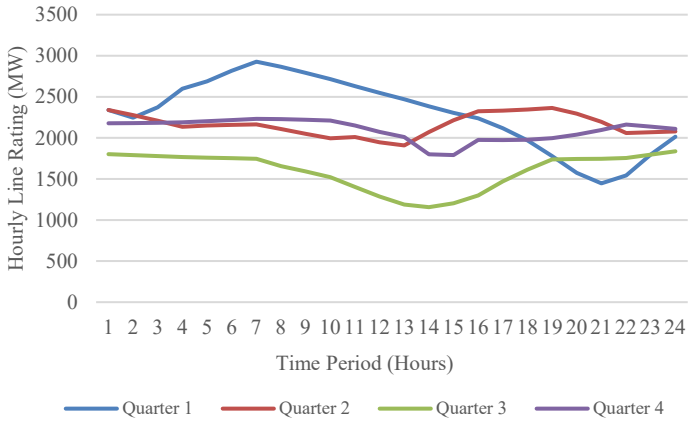

Fig. 4.9. Hourly ratings of line 15 in four typical days for different quarters.

4.2.6 SCUC Simulation and Analysis

A. SCUC Model:

To analyze the daily operational conditions of the created TX-123BT system, a standard SCUC model in [116] is used and simulation is conducted on the TX-123BT. The objective of the daily operational model is to minimize the total cost of

the power system, which includes the generator operation cost, no-load cost and startup cost. The generator related constraints such as maximum output, reserve, and ramping constraints are included. The line flow equation and nodal power balance equation are also included. In the SCUC model, the line thermal limit for fixed line rating during a day can be expressed as

$$-P_k^{max} \leq P_{kt} \leq P_k^{max} \ \forall k, t. \tag{4.28}$$

The SCUC simulations are conducted to verify daily system profiles of the TX-123BT test case with daily line ratings. Since the renewable production, line rating and loads vary differently in the 5-year period, the feasibility of SCUC optimization problems can imply the created test system is practical and reliable.

B. Comparison of the Electricity Market:

Since the locational marginal prices (LMPs) can be obtained from the SCUC simulations, the electricity market results of the TX-123BT and actual ERCOT can be compared.

1) Actual ERCOT Electricity Market

Electricity prices are affected by many factors and one year's price data may not well reflect the actual electricity market. Hence, we collect and analyze the day ahead market (DAM) price data in a 5-year period. After observing DAM prices for different hours and load zones under different scenarios, some characteristics of the actual ERCOT electricity prices are observed and summarized as: i) Electricity prices on weekends are usually lower than the prices on weekdays; ii) Quarter 3 has the highest electricity price while Quarter 1 has the lowest electricity price; iii) The

electricity prices at different load zones are slightly different during off-peak hours, but the electricity prices usually have larger locational variety during peak hours, especially in Quarter 3; iv) For the peak hours around 15:00-18:00, the electricity prices are much higher than the off-peak hour prices in Quarter 3.

2) Synthetic TX-123BT Electricity Market

The LMPs of the TX-123BT are obtained using the dual variables of the nodal power balance constraints in SCUC simulation. After the analysis of the TX-123BT LMPs and the ERCOT DAM prices, we conclude that the two systems have very similar nodal electricity prices range under different scenarios, which is shown in Table 4.6.

Table 4.6 Electricity Price Range ($/MWh) Under Different Scenarios

Scenario	Trough Hour	Normal Hour	Peak Hour
Quarter 1, Weekday	15-24	24-30	30-45
Quarter 1, Weekend	15-20	20-25	25-33
Quarter 2, Weekday	16-25	25-35	35-55
Quarter 2, Weekend	16-25	25-30	30-50
Quarter 3, Weekday	18-25	25-50	50-220
Quarter 3, Weekend	18-25	25-45	45-110
Quarter 4, Weekday	17-25	25-30	30-40
Quarter 4, Weekend	15-24	24-28	28-45

The system-wide electricity prices for different typical seasonal days are shown in Figs. 4.10 a – d. We can observe that, in Quarters 3, the electricity prices are higher than in Quarters 1. This disparity can be explained by the larger demands in Quarters 3. The high demands require generators which are more expensive for

electricity production to come online, resulting in higher electricity prices in these quarters.

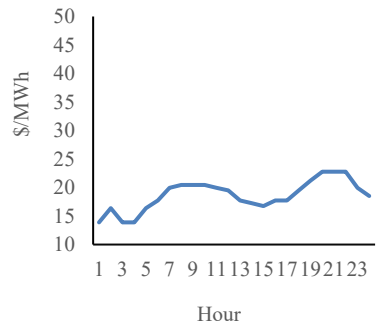

(a) Hourly LMPs for Quarter 1.

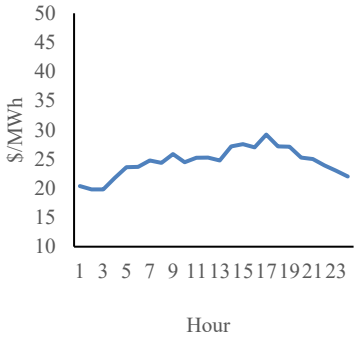

(b) Hourly LMPs for Quarter 2.

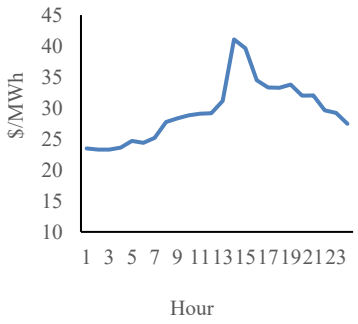

(c) Hourly LMPs for Quarter 3.

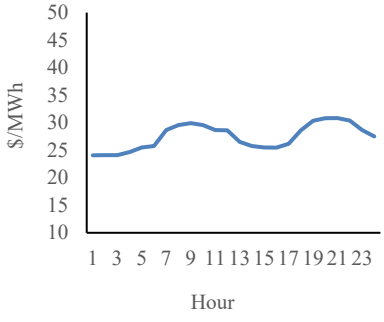

(d) Hourly LMPs for Quarter 4.

Fig. 4.10. Daily electricity prices for different quarters.

The day with the highest load among all the days is selected as the peak load day. Two scatter plots of nodal LMPs for the normal load day and peak load day are shown in Fig. 4.11 – 4.12. From the simulation results, we can conclude that the electricity prices at different load zones are slightly different during low load demand scenarios (for most buses). However, the electricity prices locational variety is large during peak hours in Quarter 3. The characteristics of the LMPs are in line with the

actual ERCOT electricity price characteristics that we summarized in the above subsection.

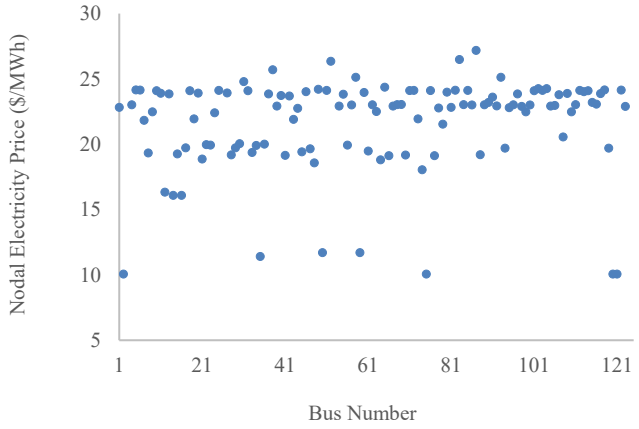

Fig. 4.11. Nodal LMPs for Hour 15 in a normal load day.

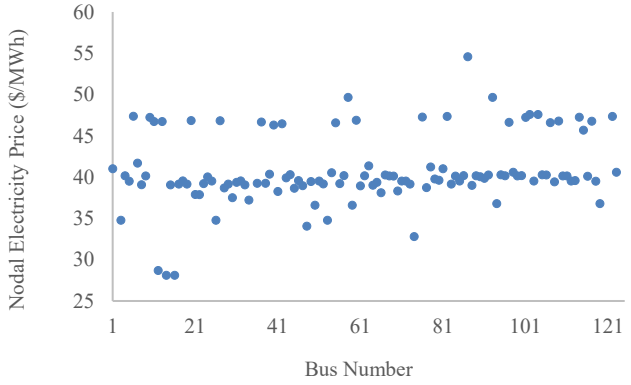

Fig. 4.12. Nodal LMPs for Hour 15 in the peak load day.

C. Peak Load Scenarios and Line Congestion Analysis:

Congested lines are classified based on the power flow results of the SCUC simulations. Two types of congested lines are classified: (i) 100% loaded lines and (ii) 90%+ loaded lines. The 100% loaded lines are the transmission lines on which the active power flow is 100% of the line capacity. The 90%+ loaded lines are the transmission lines on which the active power flow is over 90% but less than 100% of

the line capacity. The numbers of congested lines at different hours during the peak load day are shown in Fig. 4.13. We can observe more transmission lines are congested in the peak hours.

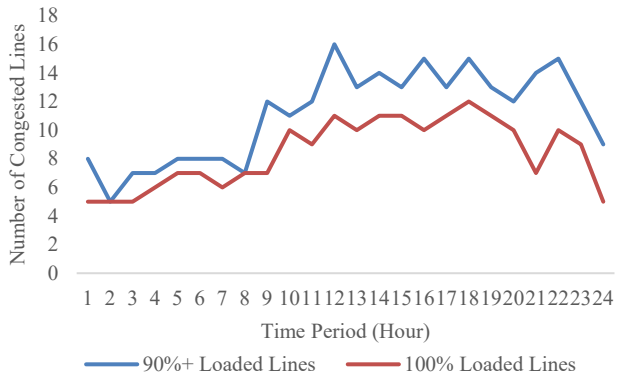

Fig. 4.13. Number of congested lines during the peak load day.

D. DLR Performance Analysis:

The SCUC simulation is also conducted on the TX-123BT with hourly DLR profiles. Since the line limits P_{kt}^{max}e now different for different hours and need an extra index of time interval t, the line thermal limit constraint is replaced by the following constraint:

$$-P_{kt}^{max} \leq P_{kt} \leq P_{kt}^{max} \; \forall k, t. \tag{4.29}$$

The SCUC simulation results including total operational cost, renewable generation, LMPs, and transmission congestion, are analyzed and compared with SCUC using daily DLR profiles. The overall numerical results are shown in Table 4.7.

Table 4.7 SCUC Simulation Results for a Normal Day in Quarter 2

Numerical Results	Daily DLR	Hourly DLR
Total Operational Cost ($)	8.09M	7.95M (-1.7%)
Total Renewable Generation (GWh)	271.95	275.48 (+1.3%)

Table 4.7 Continued

Average LMPs ($/MWh)	18.66	17.98 (-3.6%)
ANCLPH	6.9	8.2

*ANCLPH denotes the average number of congestion lines per hour.

The total operational cost of the hourly DLR case is lower than the daily line rating case, and the cost saving is about 1.7% with hourly DLR. One reason is that the increased transmission capacity can relieve network congestion and reduce the curtailment of renewable energy that has a much lower (zero) cost than the conventional generation. The average LMP of the hourly DLR case is also lower than the case using conservative daily DLR. The systemwide average LMPs for a normal day in Quarter 2 are shown in Fig. 4.14. We can observe that the average LMPs of hourly DLR is lower than the LMPs of daily DLR for majority of the hours.

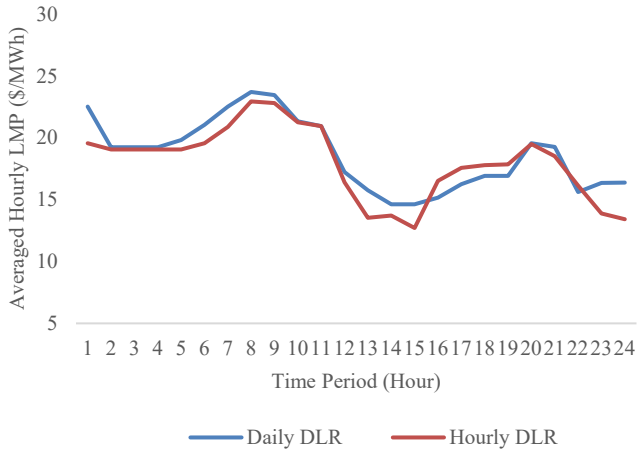

Fig. 4.14. Hourly average LMPs for a normal day in Quarter 2.

4.2.7 Hydrogen Profiles and Initial Studies

The TX-123BT test case features spatio-temporal renewable production profiles. These profiles are particularly valuable for studies requiring detailed, long-term data on renewable energy production which address its versatility. In this section, we explored potential hydrogen facility investments in TX-123BT. We examined two possible integration configurations: a hydrogen hub (HB) and a Hydrogen Energy Transmission and Conversion System (HETCS). We analyze how the TX-123BT operates with these hydrogen facilities and further investigate how the level of detail in renewable production profiles affects the operation performance.

A. Hydrogen Investments in TX-123BT:

The hydrogen hub is a localized plant which includes hydrogen tank, electrolyzers and fuel cells [117]. This setup allows for electrical energy to be converted and stored locally, then converted back when needed. The hydrogen hub can realize energy storage functions from the grid's perspective and be deployed near renewable resources to mitigate the intermittency and uncertainty associated with renewable production. Within the territory of TX-123BT, we have deployed two hydrogen hubs close to areas of renewable production. The incorporation of these two potential hydrogen hubs into TX-123BT is henceforth referred to as TX-123BT HB.

The Hydrogen Energy Transmission and Conversion System (HETCS) encompasses hydrogen pipelines, with electrolyzers and fuel cells installed at the terminal ends of the pipelines [116]. This configuration enables the conversion and transmission of electrical energy in the form of hydrogen for an HETCS-integrated grid. HETCS can

be particularly advantageous in grids with high renewable energy penetration for the long-distance transmission of surplus renewable energy. Consequently, we have deployed two HETCS lines extending from the renewable resource areas located in the northeast of Texas to the cities in the southwest. The integration of HETCS into TX-123BT is henceforth referred to as TX-123BT HT.

B. Operation of TX-123BT with Hydrogen Facilities:

For grids integrated with HB or HETCS, grid operation should consider not only the scheduling and dispatch of generators but also the working status of related hydrogen facilities, such as fuel cells, electrolyzers, hydrogen pipelines, and storage units. Co-optimizing the operations of both electrical and hydrogen facilities can maximize the overall benefits from a grid perspective. The enhanced SCUC models for hydrogen-integrated grids in Chapter 2 are utilized for daily operation simulations on TX-123BT HB and HT scenarios. These grid operation conditions are compared with those of TX-123BT without any hydrogen facilities, with findings presented in Table 4.8. Across all four quarters, the inclusion of hydrogen facilities consistently reduces daily operation costs. This confirms the specific locations and configurations of HB and HT are economically advantageous. Depending on the daily grid conditions, either the HB or HT configuration may offer the lowest daily operation costs.

Table 4.8 Daily Operation Costs of TX-123BT with Various Hydrogen Integration in Different Quarters (M$)

Quarter	No Hydrogen Case	HB Case	HT Case
Quarter I	16.748	16.728	16.722

Table 4.8 Continued.

Quarter II	7.528	7.508	7.537
Quarter III	22.714	19.546	19.506
Quarter IV	11.267	11.240	11.229

C. Evaluation on the Temporal Resolution of Profiles:

The TX-123BT dataset is distinguished by providing hourly profiles for renewable production and line ratings, which other datasets do not offer. To investigate the necessity of these high temporal resolution profiles and their effect on power system operations, SCUC simulations were performed on the HB and HETCS cases under the assumption that these spatio-temporal profiles were not accessible. The results were then contrasted with the SCUC results that included these profiles.

Table 4.9 Comparison of Daily Operation Costs (M$) for Hydrogen Studies Utilizing TX-123BT DLR Profiles

Quarter	HB with HLRP	HB without HLRP	HT with HLRP	HT without HLRP
Quarter I	16.728	17.483	16.722	17.536
Quarter II	7.508	8.838	7.537	8.028
Quarter III	19.546	22.502	19.506	21.824
Quarter IV	11.240	11.723	11.229	11.729

*HLRP represents hourly line rating profiles

In Table 4.9, the costs of daily operation with and without the dynamic line rating information are compared. It is inferred that the absence of hourly line rating data compromises the ability to accurately gauge the economic advantages of integrating hydrogen. Specifically, without access to DLR profiles, the costs associated with daily operations can surpass those incurred prior to hydrogen

integration. This suggests the critical role of DLR information in optimizing economic benefits in energy systems integrating hydrogen.

Table 4.10 Comparison of Daily Operation Costs (M$) for Hydrogen Studies Utilizing TX-123BT Weather-Dependent Renewable Production Profiles

Quarter	HB Case with WRP	HB Case without WRP	HT Case with WRP	HT Case without WRP
Quarter I	16.728	20.888	16.722	20.887
Quarter II	7.508	12.832	7.537	12.830
Quarter III	19.546	19.546	19.506	19.506
Quarter IV	11.240	15.399	11.229	15.466

*WRP represents weather-dependent renewable production profiles

The daily operation costs, both with and without considering the weather-dependent renewable production profiles, are presented in Table 4.10. Both the HB and HT cases, without the inclusion of hourly renewable production profiles based on the weather information, result in higher operation costs. However, an exception is noted in Quarter III, where loads are high and most renewable energy sources are utilized. In such situations, the detailed information on renewable production becomes less significant.

4.3 Creation of TX-123BT Future Profiles

The transmission planning requires both comprehensive technical data of the current grid configurations and future prospective information. Typically, the transmission planning needs to consider the future power system operation conditions under different scenarios in future periods. Thus, the future gird profiles including forecast load and generation information are critical for TEP to give a suitable transmission investment plan. Hence, we create the climate impacted power system

profiles based on the future climate data extracted from Coupled Model Intercomparison Project Phase 6 (CIMP6) for 2020-2050. The CIMP6 is an advanced, comprehensive, coupled model global climate change project [118]. The extracted data are for meteorological variables such as wind speed, solar radiation, and temperature under Representative Concentration Pathway (RCP) 8.5, which is considered as the most likely global warm conditions if the world makes usual efforts on emission reduction in future [119]. We compare the forecast climate data from CIMP6 model with the historical climate data from North American Land Data Assimilation System (NLDAS-2) [120] for the same period 2019-2022, and we verify that these meteorological variables in CIMP6 is coherent with the historical observations. Fig. 4.15. displays a year-long comparison of temperature data from the two datasets at a bus location.

The CIMP6 climate data has 3-hour resolution. In each 3-hour period, the wind speed, solar radiation, and temperature data for all bus locations in TX-123BT are extracted. Based on the weather dependent models for dynamic line rating, solar production and wind production, the corresponding profiles are created for 2019-2050, and have the same 3-hour resolution.

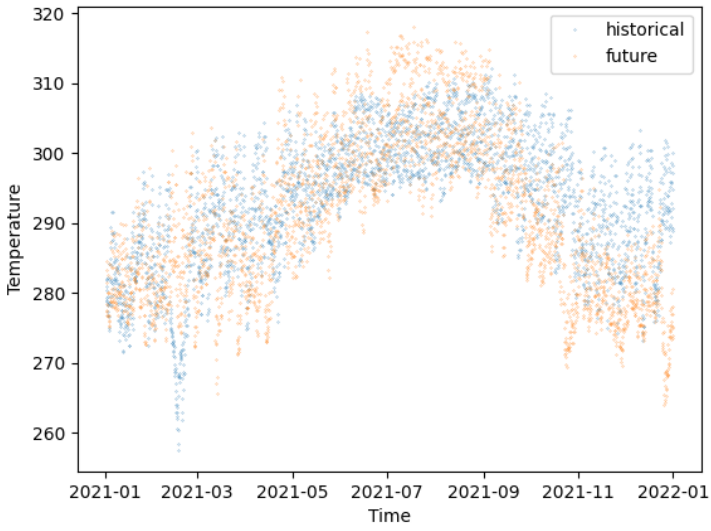

Fig. 4.15. Comparison of temperature data in CIMP6 and NLDAS-2.

For dynamic line rating, the lower wind speed, higher temperature and solar radiation on the two terminal buses of the transmission line are averaged respectively and then used in the calculation. The monthly average line ratings of a transmission line for 2019-2024 are plotted and shown in Fig. 4.16.

The gross power output for a wind farm is the aggregation of all the wind turbines in it. To simplify the relationship between the wind speed at the wind farm location and wind farm power output, we assume the wind turbines in one wind farm are the same type. Besides, the wind speed at the wind turbine height is required. Since the wind speed in CIMP6 is the wind speed at the 'surface' of earth, we estimate the wind speed at 80m using the log wind profile [121]. The monthly average wind power production of a wind plant is plotted in Fig. 4.17.

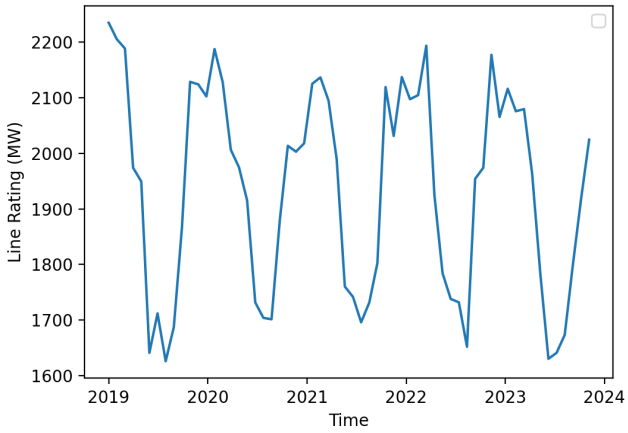

Fig. 4.16. Plot of the averaged dynamic line rating at line 1.

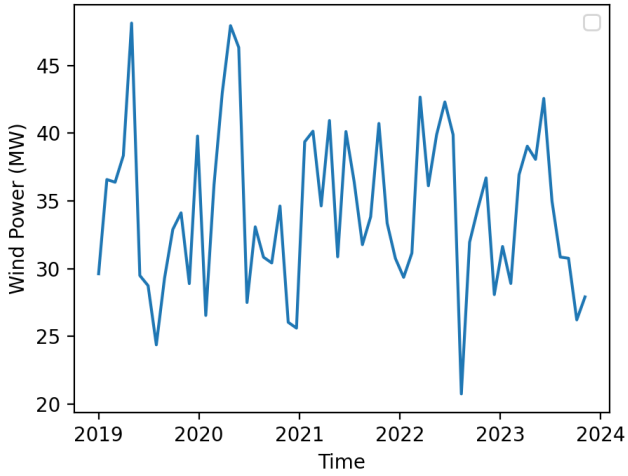

Fig. 4.17. Monthly averaged wind production at wind plant 72.

The solar production is calculated using both shortwave and longwave radiation data extracted from CIMP6. The effective radiation on the solar panel is estimated based on the frequency range of the commonly used solar panels. The solar production of solar plant 66 is plotted and shown in Fig. 4.18.

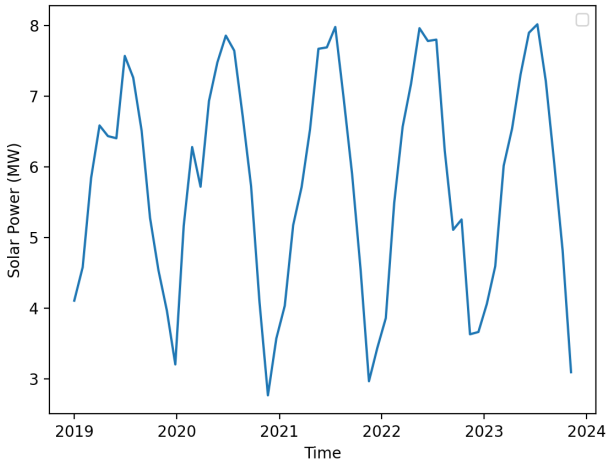

Fig. 4.18. Monthly averaged solar production at solar plant 66.

Due to the computation burden, future power system planning models such as TEP often consider a limited number of representative future scenarios. Hence, we create the representative daily profiles for every quarter of each 5-year period from 2021 to 2050. Each representative profile encapsulates the average renewable production and line ratings derived from identical hours across all days within the same quarter. Since electric demand is significantly affected by social activities, we establish representative load profiles for weekdays and weekends within each quarter. The line rating, wind production, solar production, and load profiles for quarter 1, 2021-2025 are shown in Fig. 4.19 (a) – (d).

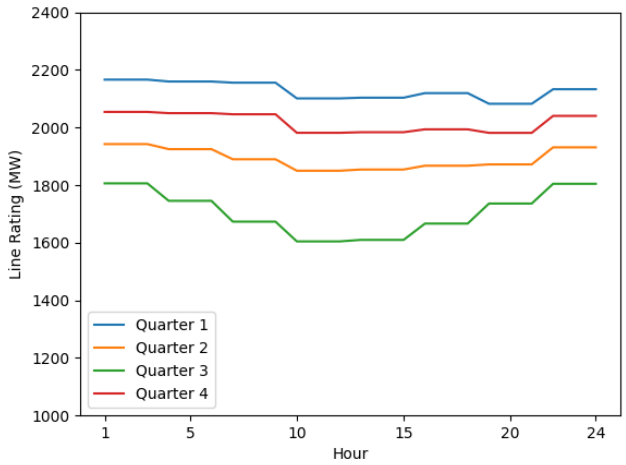

Fig. 4.19. (a) Representative line ratings of a transmission line in 2021-2025.

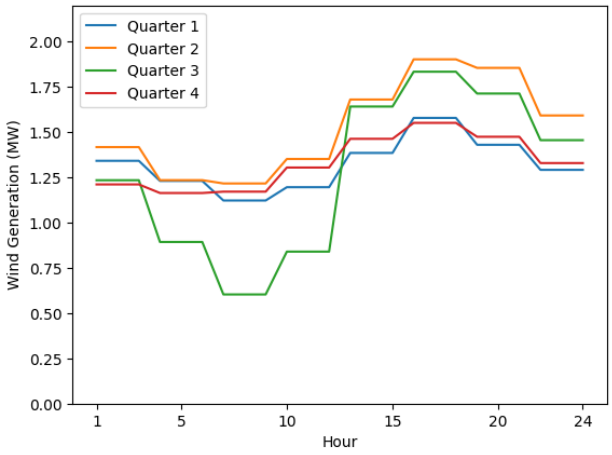

Fig. 4.19. (b) Representative power production of a wind plant in 2021-2025.

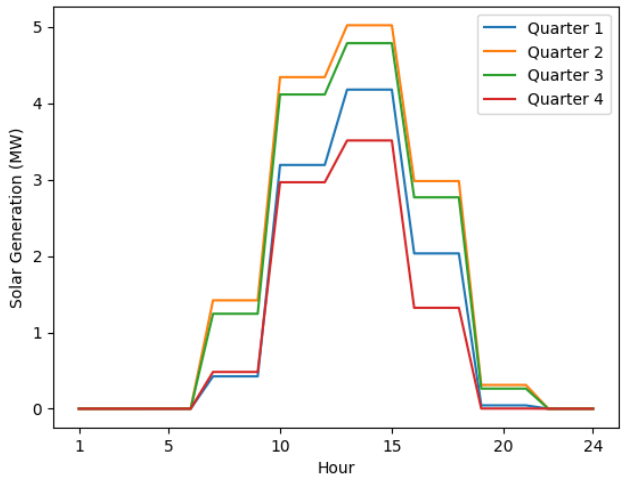

Fig. 4.19. (c) Representative power production of a solar plant in 2021-2025.

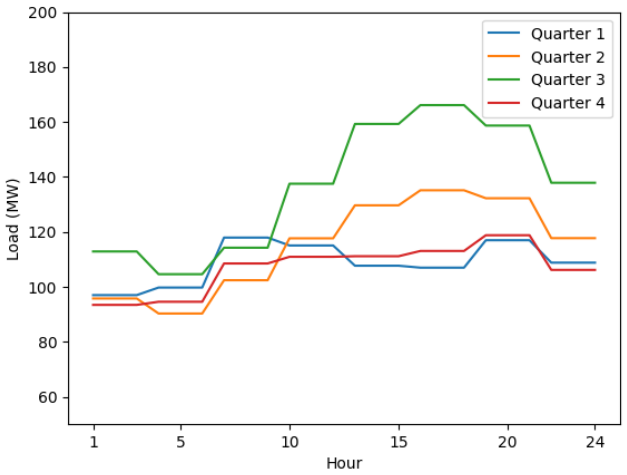

Fig. 4.19. (d) Representative loads on a bus on weekday, 2021-2025.

In Fig. 4.19. (a), the line rating in Quarter I is higher than other quarters due to the low temperature. In Quarter III, the line rating is the lowest and drops obviously during noon time due to the high temperature. According to Fig. 4.19. (b) – (c), the wind production is obviously lower in summer, while load is obviously higher. The plots illustrate why summer and winter (high wind and low load) scenarios are

necessary to be both analyzed in some industrial applications in Electric Reliability Council of Texas (ERCOT).

Since the created representative profiles don't include the future new invested power plants and transmission lines, they will be regarded as the benchmark case for the TEP simulation, referred to as TX-123BT Future (FR) case. The new power plants, including renewable resources, are interconnected with the power system through queue systems by various entities in United States. An agent-based model (ABM) is used to mimic the generation investment behavior by the market participators [122]. Each market participator is regarded as an agent and can make their own investment decisions based on the market and grid operation information. The future generation investment for TX-123BT including the capacity and plant type of different market participator, are obtained based on the ABM model. Then, the future production of the new renewables is calculated. The future TX-123BT with new generation investment and related profiles is named as the TX-123BT future generation investment (FGI) case.

5. PLANNING OF HYBRID TRANSMISSION NETWORK

5.1 Literature Review

Power systems need to expand to accommodate the rising demands, and the enhanced systems should possess the necessary transmission capability for reliable operation. New investments or upgrades in transmission and generation need to be well planned to maintain the reliability of the power systems. The transmission expansion planning (TEP) typically looks several decades ahead due to the long construction time of transmission lines and the necessity to account for long-term shifts in grid load and generation. Generally, the TEP considers multiple scenarios of the future grids for the planning period, and the associated daily operation conditions under these scenarios are estimated and evaluated. Therefore, successful transmission planning relies on detailed and accurate prediction of the future grids at the nodal or facility level for load and generation. The loads are complicated and hard to precisely forecast in long-term, due to various factors including weather and climate, socio-economics and electrification in transportation and other industry sectors [123]–[124]. Generation expansion including the locations and types of new generations is often a prerequisite for TEP. However, predicting the future generation investments at facility level is also complicated. Taking U.S. as an example, different entities usually make their own decisions for developing new power plants [125]. After determining the generation expansion plan, the forecast of future renewable generation is also essential for a comprehensive TEP study on a high renewable penetration future grid [126].

The planning horizon for TEP usually spans decades, and it is widely acknowledged that climate changes will be more pronounced compared to long-standing historical patterns [127]–[128]. Climate change can affect multiple sectors of the future grids including load, generation, and transmission [129]–[131]. While the modern grids are becoming cleaner and greener, renewable production is highly dependent on the environmental variables such as wind speed, solar radiation, and temperature which may be affected by climate change. Besides, the electrical demands, especially the loads for heating, ventilation, and air conditioning, are highly correlated with the temperature [132]. Climate change may affect both the peak demand and the average demand. Moreover, the transmission line transfer capability is influenced by the weather conditions including temperature and wind. While dynamic line rating (DLR) technique is becoming more adopted in short-term grid operations, the impact of climate change on the transmission network should also be considered in long-term grid planning studies. Based on the above-mentioned reasons, the needs of considering the climate impact on future renewable energy-dominated grids in the TEP are raised.

The trend of decarbonization in the energy field may lead to the change in both generation and consumption sides. Due to the incentive policies and other factors, more variable renewable energy (VRE) will be invested and deployed into the future power system. On the other hand, the conventional generations including coal and natural gas thermal plants are expected to be reduced. Per National Renewable Energy Laboratory, 70% of U.S. total energy are expected to be generated by renewables by

2035, and it will rise to 90% by 2050 [133]. While the future grids are expected to have this high level of renewable penetration, the current TEP strategies need improvements to adapt the large versatility and uncertainties of VRE when it becomes the dominant resource in the grids. Therefore, the U.S. Department of Energy (DOE) are proposing the state-of-the-art TEP techniques to address challenges arising from high renewable penetration [134]. Besides, climate change will directly influence the weather conditions in future, and thus influence renewable production. The impact may also increase the versatility and uncertainties of VRE, and thus increase the difficulties of operation and planning of future grids. An intuitive method to adapt to the versatility is increasing the resolution of the VRE in the TEP model.

In the literature, very few research addresses the creation of accurate future grid profiles and performs numerical analysis on the impact of climate change to the renewable grids and how it will influence the transmission planning. In [135], the climate impact on various components of power system is discussed and concluded, however no numerical analysis is conducted. In [136], the future planning of the climate-impacted Indonesia power system is studied. However, the system consists of less than 20% renewable resources, and the effects of climate change on transmission network are not considered. In [137], the climate impact on generation mix of Portuguese power systems is studied. Since the generation is not studied at facility level, the study cannot capture the spatio-temporal characteristics of the climate impacts on energy production. Existing models in current literatures do not consider

higher temporal resolution and capture temporal changes for comprehensive grid conditions including wind and solar production, and transmission line capacity.

5.2 Offshore Hybrid Energy Transmission Configuration and Sizing

5.2.1 Offshore Wind Power Delivery

Wind power is currently one of the most efficient and fast-growing renewable sources, however, it is limited primarily by land space and competing site usage. This is a factor that can be resolved with offshore wind farms. Offshore wind has experienced continuous growth in the last years, and this trend is expected to continue in the next future [138]. Despite the high efficiency and high wind power potential found offshore, one main challenge this technology presents is bringing power into shore for distribution. Offshore wind farms can be connected to onshore grids via AC or DC power transmission, and the current common trend in research is that for relatively long distances High Voltage Direct Current (HVDC) is the option with lower losses as well as minimal impact on grid disturbances [139]–[140]. Moreover, a HVDC point-to-point connection via voltage source converters (VSC) offers the cheapest option in terms of capital cost, in addition to operational advantages such as voltage control for a controlled DC power flow [140]. Another way that power can be transmitted is in the form of hydrogen. This process is known as power-to-gas, in which electrical power is used to generate hydrogen gas to be used as an energy carrier. In this way, energy can be delivered using hydrogen gas as a fuel, which inherently can be used as a means of energy storage, representing a cost-effective

solution that can compete with battery energy storage systems [141]. Also, studies show that hydrogen integrated grids can reduce both operation costs and CO2 emissions [116][142]. Based on current research trends and practices, two main paths for wind power transmission from offshore to onshore can be via HVDC transmission lines or hydrogen pipelines. Both methods of offshore power transmission have been studied and compared in literature [143]–[145], and the general consensus indicates that after certain distances from shore, hydrogen transmission becomes the most economical solution. Both HVDC transmission and power-to-gas hydrogen transmission from wind farm to onshore were analyzed and compared in [143]. This paper concludes that hydrogen is less expensive than HVDC at distances larger than 740 km. However, the study only considers power-to-gas on both cases, and there is no consideration of the advantage to use hydrogen as a means for energy storage. Moreover, some important factors such as leakage from hydrogen and drops in pressure throughout the pipelines were not considered, which can provide useful information when demonstrating which transmission technology provides the best economic benefits.

A more thorough investigation and comparison between long-distance energy transport via hydrogen pipelines and HVDC transmission is performed in [144]. Here the results indicate that overall, at long distances, hydrogen transmission yields a lower levelized cost of energy compared to HVDC offshore transmission. However, although this study does consider hydrogen energy storage, both cases involve the generation of hydrogen gas, either at the wind farm or onshore, thus the costs of both

cases involve the capital costs of main components, making the comparison exclusively about the path of transmission, i.e., the power lines and the pipelines along with the components these require. In [145], a more separate comparison between these two means of power transmission is performed, and the technologies involved with HVDC transmission and hydrogen transport via pipelines are considered separate. HVDC transmission does not involve any hydrogen generation, and hydrogen transmission only converts back to electrical power onshore and takes advantage of the energy storage aspect of hydrogen gas. However, [145] considers only transmission of power from one wind farm location to onshore, and the possibility of interconnecting multiple wind farm projects is not explored.

5.2.2 Configuration of Offshore Energy Transmission

To further investigate under which conditions hydrogen transport via pipelines provides greater cost-benefits than HVDC power transmission as well as provide different configuration options for offshore transmission networks, this study proposes an offshore hydrogen super grid topology that couples multiple offshore wind projects via a hydrogen super center (HSC) located offshore and transmits the combined power to an onshore substation.

Three different cases will be considered for comparison: a) HVDC case: direct point-to-point HVDC transmission from each wind farm location to an onshore substation; b) Hybrid case: point-to-point HVDC transmission from each wind farm location to a HSC offshore, then power transmission via high pressure hydrogen pipelines (HPHP) from the HSC to the onshore substation; and c) Hydrogen pipelines

(HP) case: hydrogen generation at each wind farm location and transmission via low pressure hydrogen pipelines (LPHP) to the offshore HSC, then all hydrogen collectively transmitted via HPHP from the HSC to the onshore substation. Diagrams for these three configurations are given in Fig. 5.1.

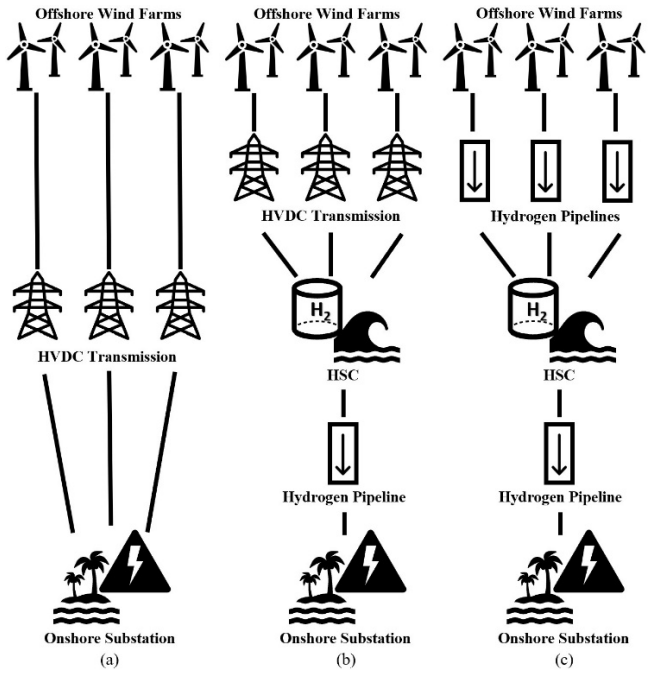

Fig. 5.1. Offshore power transmission comparison cases: (a) Benchmark point-to-point HVDC transmission, (b) Hybrid HVDC and hydrogen pipeline transmission, (c) Full offshore hydrogen pipeline transmission.

5.2.3 Model Formulation of Offshore Transmission Planning and Sizing

The optimal planning for the three different cases being considered in this paper is carried out by an optimal sizing mixed integer quadratically constrained optimization problem. This formulation will vary depending on the case as each will require different components. Still all three will derive from the same general objective and constraint expressions.

The objective of this model is to maximize the net cost-benefit of implementing the offshore wind power system following the respective configuration and selling the generated power at the onshore substation. Therefore, the objective function is given by

$$\max 365 * Y * \sum_{t \in T} C_t^{LMP} P_t^{Del} - C^T. \tag{5.1}$$

It consists of the product of the locational marginal price and the net effective power delivered at the onshore substation subtracted by the total capital and operation costs of all components involved in the configuration being considered.

Both the HVDC and the hybrid cases involve power lines; therefore, these will include constraints that describe the limit of each power line as well as the number of lines needed running from each wind farm location, which is described as

$$0 \leq P_{out,k,t}^L \leq P_{lim,k}^L N_k^L \ , \qquad \forall k = 1, \dots, N^{WF}, t \in T. \tag{5.2}$$

DC power flow is based on the steady-state DC flow of power between two nodes, which is given by

$$\eta^{DC} P_{in,k,t}^L - P_{out,k,t}^L = 1000 \left(\frac{P_{out,k,t}^L}{V^O} \right)^2 \frac{d_k^L R^L}{N_k^L} \ , \qquad \forall k = 1, \dots, N^{WF}, t \in T. \tag{5.3}$$

This power flow formulation intrinsically involves losses on the line, and the equation is formulated with converter power losses already factored in.

The constraints related to hydrogen facilities are described as follows:

$$P_{in,k,t}^E \cdot \Delta t = CP^E H_{out,k,t}^E \ , \ \forall k = 1, \dots, N^{WF}, t \in T, \tag{5.4}$$

$$P_{out,t}^{FC} \cdot \Delta t = CP^{FC} H_{in,t}^{FC} \ , \forall t \in T, \tag{5.5}$$

$$P_{k,t}^{C} \cdot \Delta t = CP^{C} H_{k,t}^{C} \ , \ \forall k = 1, \dots, N^{WF}, t \in T, \tag{5.6}$$

$$0 \leq H_{out,k,t}^{P} \leq H_{lim,k}^{P} N_{k}^{P} \ , \qquad \forall k = 1, \dots, N^{WF}, t \in T, \tag{5.7}$$

$$\left(p_{k,t}^{I}\right)^{2} - (p^{O})^{2} = 5007.7 \frac{\lambda Z T'}{\rho^{H}} \left(\frac{H_{out,k,t}^{P}}{N_{k}^{P}}\right)^{2} \frac{d_{k}^{P}}{(D^{P})^{5}} \ , \ \forall k = 1, \dots, N^{WF}, t \in T, \tag{5.8}$$

$$HS_{t} = HS_{t-1} + H_{in,t}^{S} - H_{out,t}^{S} \ , \ \forall t \in T, \tag{5.9}$$

$$HS_{min} \leq HS_{t} \leq HS_{max}, \tag{5.10}$$

$$P_{in,k,t}^{E} \leq P_{rated,k}^{E} N_{k}^{E} \ , \ \forall k = 1, \dots, N^{WF}, t \in T, \tag{5.11}$$

$$\text{and } P_{out,t}^{FC} \leq P_{rated}^{FC} N^{FC} \ , \ \forall k = 1, \dots, N^{WF}, t \in T. \tag{5.12}$$

The Hybrid and HP cases must involve Constraints (5.4) and (5.5) that describe the energy efficiencies of electrolyzers and fuel cells. The power consumption of compressors constraints is Constraint (5.6), and number of pipelines and pipeline limits is shown in Constraint (5.7). The hydrogen flow in a pipeline is formulated in Constraint (5.8) based on the equation derived in [146] and implemented in [147] for the design of hydrogen transmission networks. In addition, these two cases also involve hydrogen storage and constraints describing the storage level and limits by Constraint (5.9) and Constraint (5.10).

The decisions on the number of electrolyzers and fuel cells from Constraint (5.11) and (5.12) are obtained similar to the number of power lines and pipelines in parallel from Constraint (5.2) and Constraint (5.7), respectively, which depend on the limits and rated power of each component, increasing the number according to the needs determined by the optimal sizing model.

According to the above, the constraint formulations of the three cases are concluded in Table 5.1. Moreover, all three cases are subject to the same objective function (5.1).

Table 5.1 Formulation of the Three Cases.

Case Name	HVDC Case	Hybrid Case	HP case
Constraints	(5.2)-(5.3)	(5.2)-(5.12)	(5.4)-(5.12)

All the capacities and number of components are what will help determine the total costs based on the capital and operation costs reported in literature [148]-[150]. As per the physical quantities associated with the pipeline characteristic and hydrogen gas featured in Constraint (5.8), the hydrogen compressibility factor Z and density ρ^H are based on the thermodynamic analyses and mathematical models for hydrogen flow from [151]-[152], and the coefficient of friction λ is estimated based on the theory of the Colebrook-White equation for transitional flow presented in [151].

5.2.4 Result Analysis

In the test cases for the simulation, we select a substation located at the shore in Texas, U.S. Three wind farms with 720MW of capacity each are located in the offshore area. The onshore substation has an energy storage with 4×10^5 kg H2. The sample transmission systems of the three cases are illustrated in Fig. 5.2–5.4. The HVDC lines are in red, and the HPs are in green.

In the expected future scenario, the electrolyzer, fuel cell and hydrogen pipeline costs are halved. Under this assumption, the relationship between the total

revenue (Billion $) and hydrogen-electric conversion round-trip efficiency are shown in Table 5.2.

When the round-trip efficiency of the hydrogen-electric conversion is higher than 73%, the Hybrid case and HP case have a higher total revenue than the HVDC case. When the efficiency is 80%, the sizing results of HVDC lines, LPHPs, and HPHPs for different cases are shown in Table 5.3.

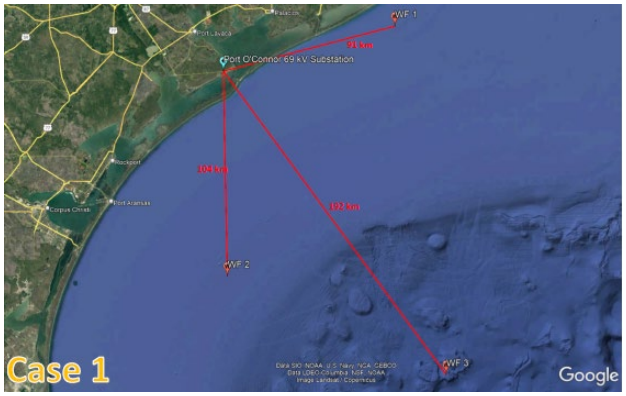

Fig. 5.2. Map of transmission system of HVDC case.

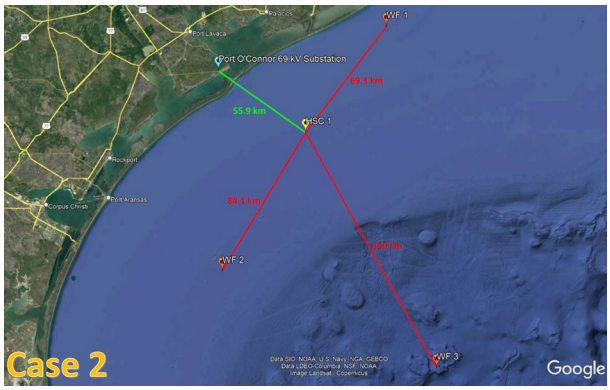

Fig. 5.3. Map of transmission system of hybrid case.

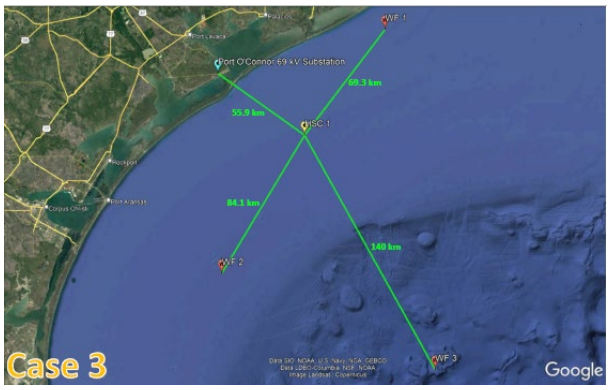

Fig. 5.4. Map of transmission system of HP case.

Table 5.2 Total Revenue (Billion $) vs. Hydrogen Round-trip Efficiency

Round-trip Efficiency	37.7% (Current)	40%	50%	60%	70%	80%	90%
HVDC case	17.2	17.2	17.2	17.2	17.2	17.2	17.2
Hybrid case	7.5	8.1	11.0	13.9	16.8	19.8	22.7
HP case	7.0	7.7	10.6	12.5	16.5	19.5	22.4

Table 5.3 The Sizing Results of Different Cases

Round-trip Efficiency	Number of HVDC Lines	Number of LPHP	Number of HPHP	Number of Electrolyzers	Number of Fuel Cells
HVDC case	3	-	-	-	-
Hybrid case	3	-	2	7,993	13,183
HP case	-	3	2	8,730	12,540

Although the HVDC and Hybrid cases have the same number of HVDC lines, the total distance of HVDC lines in the Hybrid case is much lower than HVDC case. The reason is that the HVDC lines in the Hybrid case only deliver the electric power

from the wind farms to the HSC. The distance between the HSC and wind farms is lower than the distance between the onshore substation and wind farms.

The hourly hydrogen-power exchanging conditions including the electrical energy consumed or generated by electrolyzers and fuel cells, and the energy stored in the hydrogen storage are plotted in Fig. 5.5. and Fig. 5.6. for Hybrid case and HP case separately. From the plots, we can observe that Hybrid case and HP case have very similar hydrogen-power exchanging operations. The reason is that both models optimize the hourly energy exchanging operations to maximize the revenue.

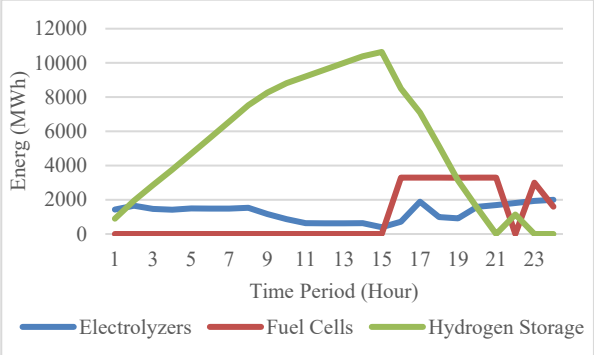

Fig. 5.5. Hydrogen-power exchange of hybrid case.

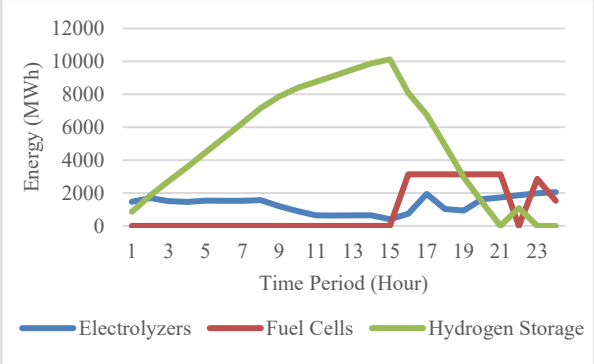

Fig. 5.6. Hydrogen-power exchange of HP case.

In the second expecting scenario, we assume the round-trip efficiency can be improved to 70%. With this assumption, the relationship between the total revenue

and electrolyzer or fuel cell costs is shown in Table 5.4. The results show that electrolyzer and fuel cell cost is an important factor affecting the total revenue.

Table 5.4 The Total Revenue (Billion $) vs. Electrolyzer and Fuel cell costs

Electrolyzer and Fuel Cell Cost Reduction	0	20%	40%	60%	80%
HVDC case	17.2	17.2	17.2	17.2	17.2
Hybrid case	13.3	14.7	16.1	17.6	19.4
HP case	12.9	14.3	15.8	17.3	18.9

To study how the transmission distance may affect the performance of different cases, we scale the network in different proportions and run the simulations. The assumptions are that the fuel cell and electrolyzer cost and hydrogen line cost are halved. The round-trip efficiency is 70%. The revenue for different transmission distances is concluded in Table 4.5. The plot of revenue vs. network distance is shown in Fig. 5.7. We can observe that for longer distance, the pure hydrogen system has higher revenue. Both HVDC case and Hybrid case have obviously revenue reduction due to the existence of long distance HVDC lines.

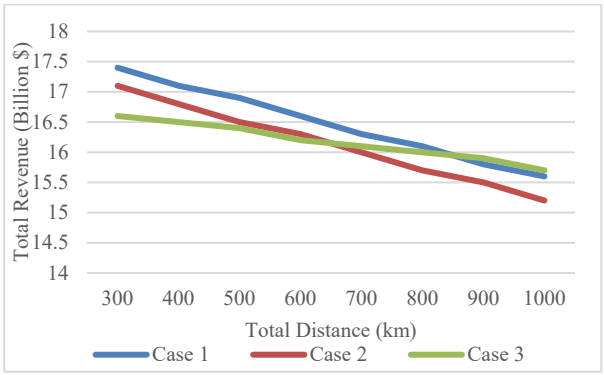

Fig. 5.7. Total revenue vs. total transmission distance.

Table 5.5 The Total Revenue (Billion $) vs. Transmission Distance.

Distance from Wind Farms to Substation (km)	300	400	500	600	700	800	900	1000
HVDC case	17.4	17.1	16.9	16.6	16.3	16.1	15.8	15.6
Hybrid case	17.1	16.8	16.5	16.3	16.0	15.7	15.5	15.2
HP case	16.6	16.5	16.4	16.2	16.1	16.0	15.9	15.7

We also study the influence of the wind farm capacity to the different cases. We select the future scenario with halved electrolyzer and fuel cell, as well as hydrogen pipeline cost. The round-trip efficiency is 70%. The total revenue vs. wind farm capacity is shown in Table 5.6. We can observe that wind farm capacity increase, both Hybrid case and HP case have much lower total revenue than HVDC case. The increased wind farm capacity leads to more wind energy generation. The Hybrid case and HP case require more hydrogen-power exchanging through electrolyzers and fuel cells. Due to the energy dissipated in the conversion, the Hybrid case and HP case will sell less energy to the bulk grid and have less total revenue. Hence, the limitation of the hydrogen integrated offshore transmission configuration is caused by the energy consumption in the hydrogen-electric conversion.

Table 5.6 The Total Revenue (Billion $) vs. Wind Farm Capacity

Each Wind Farm Capacity (MW)	360	720	1,080	1,440	1,800
HVDC case	7.7	17.2	24.9	34.4	43.8
Hybrid case	7.5	16.8	23.1	28.2	33.3
HP case	7.8	16.5	24.6	29.4	33.5

5.2.5 Summary of Offshore Energy Transmission Planning

This study explores three different topologies of offshore wind power transmission to shore, aiming to compare and analyze the benefits of implementing power transmission in the form of hydrogen gas via pipelines. The three topologies examined are HVDC transmission, a hybrid of HVDC and hydrogen pipelines, and purely hydrogen pipeline transmission. The focus is on assessing the economic and efficiency impacts of each method to identify the most cost-effective solution under various conditions. The study begins by considering HVDC transmission as the benchmark. HVDC technology is well-established for long-distance power transmission due to its lower losses and minimal impact on grid disturbances. The second topology, the hybrid approach, combines HVDC transmission from offshore wind farms to a hydrogen supercenter (HSC) located offshore. From the HSC, power is converted to hydrogen gas and transmitted to the onshore substation via high-pressure hydrogen pipelines (HPHP). The third topology involves direct hydrogen generation at each wind farm location, followed by transmission via low-pressure hydrogen pipelines (LPHP) to the HSC. From the HSC, the hydrogen is collectively transmitted via HPHP to the onshore substation.

Numerical simulations were conducted over a 30-year planning period using the proposed optimization models for each topology. The study used an offshore scenario with three wind farms located in the Gulf of Mexico and one onshore substation. The simulations showed that hydrogen-based methods could effectively transmit offshore energy to the onshore substation. The results indicated that the

distance between wind farms and the onshore substation significantly influences the selection and configuration of the transmission system. The numerical results also highlight the critical need for higher efficiencies and cost reductions in electrolyzer and fuel cell components for hydrogen transmission topologies to outperform HVDC transmission. The simulation results also showed that revenue improves for both the hybrid and HP cases compared to the HVDC case after around 1000 km. This study also indicates that with ongoing improvements in electrolyzer and fuel cell efficiencies and costs, hybrid or pure hydrogen transmission could become more economical at distances as short as 100 km in the future.

In summary, this paper provides a comprehensive comparison of different offshore wind power transmission methods, highlighting the potential economic benefits of hydrogen-based systems under certain conditions. It emphasizes the importance of technological advancements in electrolyzer and fuel cell efficiencies and cost reductions to make hydrogen transmission a viable alternative to HVDC. The findings contribute to the ongoing discourse on optimizing offshore wind power transmission.

5.3 Improved TEP for Climate-impacted Renewable Energy-Dominated Grids

Traditionally, the TEP model considers the future grid and market trends such as increasing loads and fuel price, whereas the weather and climate impact is not considered. The climate may impact the grid on various sectors such as transmission, generation, and loads. In Chapter 4, the representative profiles including the renewable

production and dynamic line ratings of the future climate impacted grid are created. In this study, we address the timely changing characteristics of the renewable production and dynamic line ratings due to the meteorological variables in the TEP model. The modeling of the proposed TEP-CI and its transmission investment plan on the TX-123BT are presented.

5.3.1 TEP-CI Model for Climate-Impacted Grids

In order to consider these climate-impacted components in the TEP-CI, we have made the following updates to the TEP model: i) The line flow capacity constraints now include the changing line ratings for different hours in the representative scenario; ii) The constraints are added to describe the available renewable resources in the system; iii) The power balance equation is modified to include the weather-dependent renewable production and load profiles. After the update, the TEP-CI can utilize the representative profiles created. The detailed TEP-CI model is shown as follows:

$$\min C^{OP} + C^{CAP}, \tag{5.13}$$

$$\begin{aligned} C^{OP} = {} & N^{Y} \cdot B^{MVA} \cdot \frac{365}{N^{D}} \cdot \sum_{g \in G, t \in T, d \in D^{T}, p \in P} p^{G}_{g,t,d,p} \cdot C^{G}_{g}, \\ & + N^{Y} \cdot B^{MVA} \cdot \frac{365}{N^{T}} \cdot \sum_{g \in G', t \in T, d \in D^{T}, p \in P} p^{G'}_{g,t,d,p} \cdot C^{G'}_{g}, \end{aligned} \tag{5.14}$$

$$C^{CAP} = \sum_{k \in L', p \in P} V^{L'}_{k,p} \cdot C^{L'}_{k} (1 + (N^{P} - p + 1) R^{M} \cdot N^{Y}), \tag{5.15}$$

$$\sum_{j \in L^{T(n)}} p^{L}_{j,t,d,p} - \sum_{j \in L^{F(n)}} p^{L}_{j,t,d,p} + \sum_{j \in L^{N,T(n)}} p^{L'}_{j,t,d,p}, \tag{5.16}$$

$$- \sum_{j \in L^{N,F(n)}} p^{L'}_{j,t,d,p} + \sum_{g \in G^{B(n)}} p^{G}_{g,t,d,p} + \sum_{g \in G^{N,B(n)}} p^{G'}_{g,t,d,p},$$

$$+ \sum_{r \in R^{B(n)}} p^{R}_{r,t,d,p} + p^{R'}_{n,t,d,p} = p^{D}_{n,t,d,p}$$

$$\forall n \in B, t \in T, d \in D^{T}, p \in P,$$

$$p^{Min}_{g} \leq p^{G}_{g,t,d,p} \leq p^{Max}_{g} \tag{5.17}$$

$$\forall g \in G, t \in T, d \in D^{T}, p \in P,$$

$$p^{Min}_{g,p} \leq p^{G'}_{g,t,d,y} \leq p^{Max}_{g,p} \tag{5.18}$$

$$\forall g \in G', t \in T, d \in D^{T}, p \in P,$$

$$p^{Min,R}_{r} \leq p^{R}_{r,t,d,p} \leq p^{Max,R}_{r,t,d,p} \tag{5.19}$$

$$\forall r \in R, t \in T, d \in D^{T}, p \in P,$$

$$p^{Min,R'}_{r} \leq p^{R'}_{r,t,d,y} \leq p^{Max,R'}_{r,t,d,p} \tag{5.20}$$

$$\forall r \in R', t \in T, d \in D^{T}, p \in P,$$

$$-p^{Max}_{k,t,d,p} \leq p^{L}_{k,t,d,p} \leq p^{Max}_{k,t,d,p} \tag{5.21}$$

$$\forall k \in L, t \in T, d \in D^{T}, p \in P,$$

$$-M\left(1 - u^{L'}_{k,p}\right) \leq p^{L'}_{k,t,d,p} - \frac{\theta^{F}_{k,t,d,p} - \theta^{T}_{k,t,d,p}}{x^{L'}_{k}} \leq M\left(1 - u^{L'}_{k,p}\right), \tag{5.22}$$

$$\forall k \in L', t \in T, d \in D^{T}, p \in P,$$

$$-p_{k,t,d,p}^{Max,NL} * u_{k,p}^{NL} \leq p_{k,t,d,p}^{NL} \leq p_{k,t,d,p}^{Max,NL} * u_{k,p}^{NL}) \quad (5.23)$$
$$\forall k \in L', t \in T, d \in D^T, p \in P,$$

$$\sum_{p' \in P, p' \leq p} u_{k,p'}^{L'} \leq u_{k,p}^{L'} \quad \forall k \in L', p \in P, \quad (5.24)$$

$$v_{k,p}^{L'} \geq u_{k,p}^{L'} - u_{k,p-1}^{L'}, \forall k \in L', p \in P, p > 1, \quad (5.25)$$

$$\text{and } v_{k,1}^{L'} = u_{k,1}^{L'} \quad \forall k \in L'. \quad (5.26)$$

The TEP-CI can minimize the operation and transmission investment cost for the studied period by Equation (5.13). The operation cost includes both the existing and new thermal generators in Equation (5.14). The capital cost of the transmission line is simplified by assuming the yearly maintenance cost is a partial of the total construction cost in Constraint (5.15). The nodal power balance addresses the available renewable resources for each time interval by Constraint (5.16). The power output constraint for existing thermal generators and newly invested generators obtained from the ABM are described by Constraint (5.17) and Constraint (5.18) separately. The renewable power output for each time interval should be under its available amount. To be noticed, $p_{r,t,d,p}^{\mathrm{Max,R}}$ is the maximum available renewable output in the representative profiles, which is calculated using the CIMP6 climate data. The power output constraints for both existing and new renewables are Constraint (5.19) – (5.20). The line flow limit for existing transmission line is in Constraint (5.21), and $p_{k,t,d,p}^{\mathrm{Max}}$ is the dynamic line ratings in the representative profiles. To model the line flow limit of the new transmission line, we use a big number M and the binary variable $u_{k,p}^{NL}$ to enforce the DC power flow constraint when the line is constructed, as

described in Constraint (5.22). The flow limit of the new lines is described by Constraint (5.23). The constraints related to the binary variables for line construction are shown in Constraint (5.24) – (5.26).

While this model integrates a wide range of general physical constraints related to power flow and generators, it demands accurate forecasts for future renewable energy production and dynamic line ratings affected by weather variations. The reliability of these forecasts hinges on specific climate models that may not encompass every potential future climate scenario, along with detailed geographic data at the facility level for the transmission network and renewable power plants.

5.3.2 Transmission Investment for TEP-CI

The TEP models are implemented using Python with Pyomo package [153]. Since the models are formulated as mixed-integer linear programming (MILP) problem, the commercial solver Gurobi [154] is used to find optimal solutions for the models. Our proposed TEP model is designed to accommodate various resolution profiles, such as one-hour or three-hour intervals, denoted by t periods within a day. Given that our profiles are created at a 3-hour resolution, preserving this granularity in the model helps to shorten simulation duration without compromising the quality of the solutions. In the first TEP-CI simulation, we set the number of year-epoch to 3, and each epoch represents a 5-year period. Thus, it determines the transmission planning of TX-123BT for the period 2021-2035. Even for the TX-123BT FR case, which has no generation investments made during this planning period, the TEP-CI can easily find a feasible solution. The transmission line investment results are shown

in Table 5.8. The total cost, generation costs and transmission line investment cost are presented in Table 5.7.

The TEP-CI finds 15 transmission lines to be invested. The transmission line investment cost is $3B, which is about 2.94% of the total cost for TX-123BT FR during 2021-2035.

In the second TEP-CI simulation, we set the number of year-epoch to 6, which means the TEP-CI will give the transmission investment results for 2021-2050. For this future period, the safety-secured operation cannot be maintained without load shedding for FR case. The electricity demands are expected to increase rapidly in 2035-2050, and existing generation resources cannot meet the needs for such large amounts of loads. Using the representative profiles under FGI case as input for TEP-CI, the simulation results are shown in Table 5.9 and 5.10.

Table 5.7 TEP Investment and System Operation Costs in 2021-2035 for FR Case

Costs	Amount ($)
Generation Cost	102.87B
Transmission Line Investment Cost	3.02B
Total Cost	105.89B

Table 5.8 New Transmission Lines Investment in 2021-2035 for FR Case

New Line Number	Construction Period	New Line Number	Construction Period
2	2021-2025	68	2025-2030
6	2026-2030	72	2021-2025
7	2021-2025	74	2026-2030
22	2025-2030	165	2026-2030
31	2021-2025	171	2026-2030
50	2025-2030	233	2031-2035

Table 5.8 Continued.

56	2025-2030	249	2021-2025
58	2025-2030		

Table 5.9 Transmission Lines Investment in 2021-2050 for FGI Case

New Line Number	Construction Period	New Line Number	Construction Period
3	2036-2040	80	2041-2045
6	2041-2045	74	2021-2025
7	2031-2035	82	2041-2045
8	2036-2040	83	2021-2025
9	2031-2035	112	2036-2040
30	2041-2045	147	2021-2025
49	2041-2045	189	2021-2025
57	2041-2045	191	2021-2025
72	2021-2025	247	2021-2025

Table 5.10 The TEP Investment and System Operation Costs (2021-2050)

Costs	Amount ($)
Generation Cost	146.76B
Transmission Line Investment Cost	6B
Total Cost	152.76B

We calculate the dynamic ratings of the new lines in the investment plan, for the future periods after they are constructed. The new transmission lines and their dynamic rating profiles are then integrated into the TX-123BT FGI case and form the future scenario that includes both generation and transmission investments. It is called the TX-123BT future generation and transmission investment (FGTI) case.

The comparisons between TEP-CI and traditional TEP method [155] are concluded in Table 5.11. TEP-CI results in greater transmission investments due to its

utilization of detailed and high-resolution climate-impacted profiles. While this approach leads to higher initial transmission costs, it significantly lowers generation costs over the planning periods.

Table 5.11 TEP and TEP-CI Results for FGI case in 2021-2035

	TEP	TEP-CI
Total Costs	$ 79.34B	$ 55.73B (-29.7%)
Transmission Line Investment Costs	$ 0.24B	$ 0.47B (+ 95.8%)
Generation Costs	$ 79.1B	$ 55.26B (-30.1%)
Total Flow on Transmission Lines	18,727 MWh	22,988 MWh (+22.75)

Table 5.12 presents the solving times for TEP-CI compared to traditional TEP models. For shorter planning spans, such as 15 years, TEP-CI does not significantly extend solving times. However, due to TEP-CI model considers higher resolution of climate-impacted profiles, TEP-CI solving times increase markedly for longer spans.

Table 5.12 The Solving Time (Seconds) for TEP-CI and Traditional TEP

Planning Span	TEP	TEP-CI
15 Years	209.5	214.7 (+2.48%)
30Years	6235.6	8821.1 (+41.4%)

Adapting our methodology to power systems across various geographic regions necessitates precise predictions for future renewable energy production and dynamic line rating profiles. Achieving such accuracy may involve integrating region-specific climate and weather forecast data and utilizing the ABM approach or other regionally appropriate methods, to accurately forecast future renewable energy investments.

5.3.3 SCUC Simulation for TEP Evaluation

The SCUC model is modified and customized specifically for the future climate-impacted study and TEP performance evaluation. Firstly, to study the reliability performance of the grid under different investment plans, also due to the potential reliability issues in the future grid, the load shedding should be considered in the SCUC model. Specifically, the load shedding variables are introduced to the power balance equations, and the constraints describing the maximum shedding amount are added to the SCUC model. The loads will be shedded only when the power systems cannot be operated safely. The shedding should happen when the physical constraints cannot be satisfied, because it may cause both economic losses and social disturbance. Hence, a penalty term is added to the objective function of the SCUC model, to make sure the load shedding can only happen when it is necessary. With the improved model, the SCUC solutions can give us information about the unserved load amount due to the electrical demand increasing and climate change in the future.

Secondly, the climate-dependent grid profiles have the same 3-hour resolution as the climate data, while the commonly used SCUC has hourly resolution. We can simply transfer the 3-hour resolution profiles into hourly profiles by assuming all the 3 hours have the same data and used as hourly data input for SCUC. However, for both SCUC simulations on a large number of future profiles and the TEP for climate-impacted grids, the number of time intervals in models will significantly influence the computation time. Hence, the SCUC model is adjusted from hourly resolution to 3-hour resolution. Besides, the SCUC input data such as generator costs

c0, *c1* and generator ramping rate data are updated for 3-hour resolution. The detailed formulation of SCUC for TEP evaluation is shown as follows:

$$\min \sum_{g\in G(p)} \sum_{t\in T} \left(c_g P_{g,t} + c_g^{\mathrm{On}} u_{g,t} + c_g^{\mathrm{SU}} v_{g,t}\right) + M \cdot \sum_{b\in B\ t\in T} p_{n,t}^{\mathrm{S}}, \tag{5.27}$$

$$p_{n,t}^{\mathrm{RC}} = 0, \qquad \forall (n,t) \in ST^1, \tag{5.28}$$

$$ST^1 = \{(n,t) \mid n \in B, t \in T, s.t.\ \ p_{n,t}^{LD} - \sum_{r\in R(b)} p_{r,t}^{R} \geq 0\} \tag{5.29}$$

$$p_{n,t}^{\mathrm{RC}} \leq \sum_{r\in R(b)} p_{r,t}^{\mathrm{R}} - p_{n,t}^{\mathrm{D}}, \qquad \forall (n,t) \in ST^2, \tag{5.30}$$

$$ST^2 = \{(n,t) \mid n \in B, t \in T, s.t.\ \ p_{n,t}^{LD} - \sum_{r\in R(n)} p_{r,t}^{R} < 0\} \tag{5.31}$$

$$p_{n,t}^{\mathrm{RC}} \leq p_{n,t}^{\mathrm{D}} - \sum_{r\in R(n)} p_{r,t}^{\mathrm{R}} \quad \forall (n,t) \in ST^1, \tag{5.32}$$

$$p_{n,t}^{\mathrm{RC}} = 0 \quad \forall (n,t) \in ST^2, \tag{5.33}$$

$$P_g^{\min} \cdot u_{g,t} \leq P_{g,t} \quad \forall g,t, \tag{5.34}$$

$$P_{g,t} + r_{g,t} \leq P_g^{\max u_{g,t}} \quad \forall g,t, \tag{5.35}$$

$$0 \leq r_{g,t} \leq R_g^{10} u_{g,t} \quad \forall g,t, \tag{5.36}$$

$$\sum_{m\in G} r_{m,t} \geq P_{g,t} + r_{g,t} \quad \forall g,t \tag{5.37}$$

$$-R_g \leq P_{g,t} - P_{g,t-1} \leq R_g \quad \forall g,t, \tag{5.38}$$

$$P_{k,t} = \theta_{k,t}/x_k \quad \forall k,t, \tag{5.39}$$

$$-P_{k,t}^{\max} \leq P_{k,t} \leq P_{k,t}^{\max} \quad \forall k,t, \tag{5.40}$$

$$\sum_{g\in G(n)} P_{g,t} + \sum_{k\in K(n-)} P_{k,t} - \sum_{k\in K(n+)} P_{k,t} + \sum_{r\in R(n)} p_{r,t}^{\mathrm{R}} \tag{5.41}$$

$$= p_{n,t}^{\mathrm{D}} + p_{n,t}^{\mathrm{RC}} - p_{n,t}^{\mathrm{S}} \quad \forall n, t\ ,$$

$$\text{and } v_{gt} \geq u_{gt} - u_{g,t-1} \quad \forall g, t > 1. \tag{5.42}$$

In Equation (5.27), the SCUC will optimize the operation cost for the day, and an additional term is added to ensure load shedding is employed strictly as a last resort. There will be no renewable curtailment on a bus when the total renewable power is less than the load at the location according to Constraints (5.28) – (5.29). The maximum renewable curtailment is constrained by Equation (5.30) – (5.31). Similarly, the load shedding can only be made when the renewable power on the bus is not sufficient in Constraints (5.32) – (5.33). The thermal generator minimum and maximum power output, the reserve constraints, and ramping limits are in Constraints (5.34) – (5.38). The DC power flow and line flow limits are in Constraints (5.39) – (5.40). The nodal power balance equation includes both the load shedding and renewable curtailments by Constraint (5.41). The generator online and starting binary variables are constrained by Constraint (5.42).

In each FR, FGI and FGTI case, the future representative profiles from 2021 to 2050 includes 48 daily profiles, for weekdays and weekends in each quarter in each 5-year planning epoch. The SCUC simulations are run on all the daily profiles for different scenarios. The weekday highest load shedding for different quarters in 2041-2045, 2046-2050 are shown in Fig. 5.8.

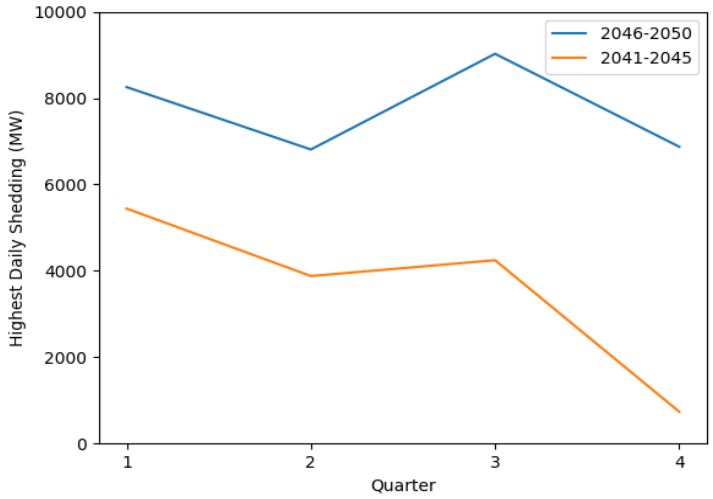

Fig. 5.8. Highest daily load shedding for weekdays under FR scenario.

We observe that under FR scenario, the grid must necessarily shed loads after 2040. The required load shedding amount grows rapidly due to the increasing load demand. It indicates that the current system conditions cannot handle the increasing loads in 20 years later. It is reasonable given the absence of expansions and developments in generation and transmission infrastructure under FR scenario.

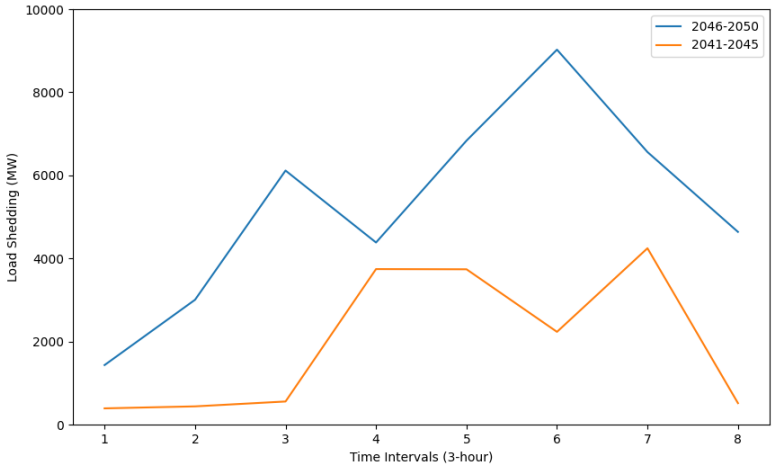

Fig. 5.9. Load sheddings for Quarter 3 weekends in 2041-2045 and 2046-2050.

The load sheddings for weekends in Quarter 3 in periods 2041-2045 and period 2046-2050 under FR scenario are plotted in Fig. 5.9. Load shedding for 2046-2050 is substantially greater than that of 2041-2045, and the daily shedding patterns differ significantly between the two five-year spans.

Table 5.13 Total Operation Costs and Generation in Quarter 3 under FGTI Scenario for Different 5-year Periods

	Total Operation Costs (M $)		Total Generation (GWh)	
5-year Period	Weekdays	Weekends	Weekdays	Weekends
2021-2025	11.55	11.62	711.1	714.2
2026-2030	13.94	13.90	810.27	808.6
2031-2035	17.41	15.31	940.3	858.5
2036-2040	21.52	17.90	1090.7	956.4
2041-2045	26.83	21.18	1263.9	1070.2
2046-2050	33.43	25.17	1462.1	1199.1

Under the FGTI scenario, Table 5.13 summarizes the daily operation costs and total scheduled generation from thermal plants. A comparison between the weekdays in periods 2021-2025 and 2046-2050 reveals that the total generation approximately doubled, while the total operation costs have roughly tripled. This discrepancy is attributable to the higher marginal prices associated with generator's high power output level. This situation arises because few thermal power plants are invested in the future, while the total generation is increasing.

5.3.4 Reliability Evaluation

To evaluate the reliability of future grids under different investment scenarios, we develop several reliability indices which can be calculated based on SCUC numerical results of the operation conditions for all days in future. We select

the concepts of reliability indices which are widely used in industry and academics as the indices for our risk analysis. These indices include the expected unserved energy (EUE), loss of load probability (LOLP) and loss of load expectation (LOLE). The three indices are the implications of the power system's ability to reliably meet energy demand from different aspects. Each index offers a unique lens through which the robustness and resilience of the grid can be assessed, catering to the intricate dynamics of power supply and demand. Expected unserved energy (EUE) quantifies the total energy that cannot be supplied due to system limitations within a specified timeframe, serving as a direct measure of the magnitude of energy deficit. A higher EUE indicates more significant instances where the grid fails to meet demand, pointing towards potential weaknesses in generation capacity or transmission infrastructure. This index is especially crucial in evaluating the system's performance during peak demand periods or in scenarios with high renewable energy variability, where the balance between supply and demand is most delicate. Loss of load probability (LOLP) assesses the likelihood that the power system will not meet the demand at any given time, essentially reflecting the system's overall reliability. An increase in LOLP suggests a greater risk of power shortages, signaling the need for enhanced system planning and investment in reliability improvements. It underscores the importance of having sufficient reserve margins and flexible resources that can quickly respond to fluctuations in demand and supply. Loss of load expectation (LOLE), expressed in hours per year, estimates the expected duration of load not being served. This index complements LOLP by providing insight into the length of time the system might be

under stress, thus affecting consumer experience and economic activities. A lower LOLE value is indicative of a power system that, while it may occasionally fail to meet demand, does so for a minimal duration, minimizing disruption to end-users.

In synthesizing the insights derived from EUE, LOLP, and LOLE, decision-makers and stakeholders gain a comprehensive understanding of the power system's operational challenges and areas requiring attention.

The EUE is an index that can evaluate the amount of total unserved energy for a given period, such as one year. It can evaluate the scale of the outage by calculating the total unserved energy amount, which is described as

$$\mathrm{EUE} = \sum_{p\in P, d\in D^{T(D)}, n\in B, t\in T} p^{\mathrm{S}}_{p,d,n,t} \cdot N^{\mathrm{D}} + \sum_{p\in P, d\in D^{T(E)}, n\in B, t\in T} p^{\mathrm{S}}_{p,d,n,t} \cdot N^{\mathrm{E}}. \tag{5.43}$$

The LOLP is the probability of load loss / shedding occurrence. Specifically, it measures how often the power system cannot serve all the loads, such as load curtailment or black out. The LOLP is usually calculated for a specific period such as one year, and can be expressed as

$$\mathrm{LOLP} = \mathrm{EUE}/\Big(\sum_{p\in P, d\in D^{T(D)}, n\in B, t\in T} p_{p,d,n,t} \cdot N^{\mathrm{D}} + \sum_{p\in P, d\in D^{T(E)}, n\in B, t\in T} p_{p,d,n,t} \cdot N^{\mathrm{E}}\Big). \tag{5.44}$$

The LOLE can indicate the expected total outage duration for a specific period, such as one year. In our LOLE calculation, we calculate the average outage hour on a bus for the entire year and it is given by

$$\mathrm{LOLE} = \Big(\sum_{p\in P, d\in D^{T(D)}, n\in B} N^{\mathrm{H}}_{p,d,n} \cdot N^{\mathrm{D}} + \sum_{p\in P, d\in D^{T(E)}, n\in B} N^{\mathrm{H}}_{p,d,n} \cdot N^{\mathrm{E}} \Big) / N^{\mathrm{B}}. \qquad (5.45)$$

Compared with LOLP, the LOLE can give us an insight on how long the load loss will last, instead of the occurrence probability of the load loss. As a brief conclusion, the LOLP, LOLE and EUE can comprehensively evaluate the load loss occurrence probability, duration, and the scale.

The results of calculated reliability indices based on the SCUC results for FR, FGI and FGTI cases, are shown in Tables 5.14 – 5.16. With the transmission investments planned by TEP-CI, all three reliability indices for 2041-2045 decreased significantly. For the period 2046-2050, the LOLP and EUE both reduced significantly due to the transmission investments. LOLE has not decreased as substantially as the other two indicators, this suggests that while the severity of outages has been significantly mitigated, their durations remain prolonged. Based on the results and analysis, future grid reliability sees marked improvement with the transmission investments obtained by the TEP-CI strategy.

Table 5.14 Different Risk Indices of Future TX-123BT without Investment

Index	P1	P2	P3	P4	P5	P6
Annual LOLP	0%	0%	0%	0.013%	0.81%	4.06%
LOLE (Hours/Bus)	0	0	0	2.92 (0.036%)	25.36 (0.32%)	125.26 (1.55%)
EUE (MWh)	0	0	0	69,105.24	4,803,316	27,233,362

P1 to P6 denotes the future periods from 2021-2025 to 2046-2050.

Table 5.15 Different Risk Indices of Future TX-123BT with TEP-CI

Index	P1	P2	P3	P4	P5	P6
Annual LOLP	0%	0%	0%	0%	0.0716%	2.56%
LOLE (Hours/Bus)	0	0	0	0	2.92 (0.036%)	100.48 (1.24%)
EUE (MWh)	0	0	0	0	380,304	17,148,794

Table 5.16 Different Risk Indices of Future TX-123BT with TEP and Generation Investment

Index	P1	P2	P3	P4	P5	P6
Annual LOLP	0%	0%	0%	0%	0%	0.0626%
LOLE (Hours/Bus)	0	0	0	0	0	24.0 (0.29%)
EUE (MWh)	0	0	0	0	0	419,486

5.4 Integrated Expansion Planning Strategy for Renewable Energy Systems

5.4.1 Cooperation of Hydrogen and Electric Transmission

In power grids with high renewable energy penetration, substantial transmission capacity is required to carry renewable energy to load areas. Anticipating a significant increase in renewable power plants in the near future, the transmission capability of current power grids needs substantial enhancement. In the electrical transmission network, renewable energy is transferred through transmission lines. Conversely, in the hydrogen transmission network, electrical energy is first converted into hydrogen energy via electrolyzers, then transmitted through hydrogen pipelines. Near the load areas, hydrogen energy is reconverted into electrical energy through fuel

cells. Fig. 5.10 illustrates the pathways of electric, hydrogen, and hybrid transmission configurations.

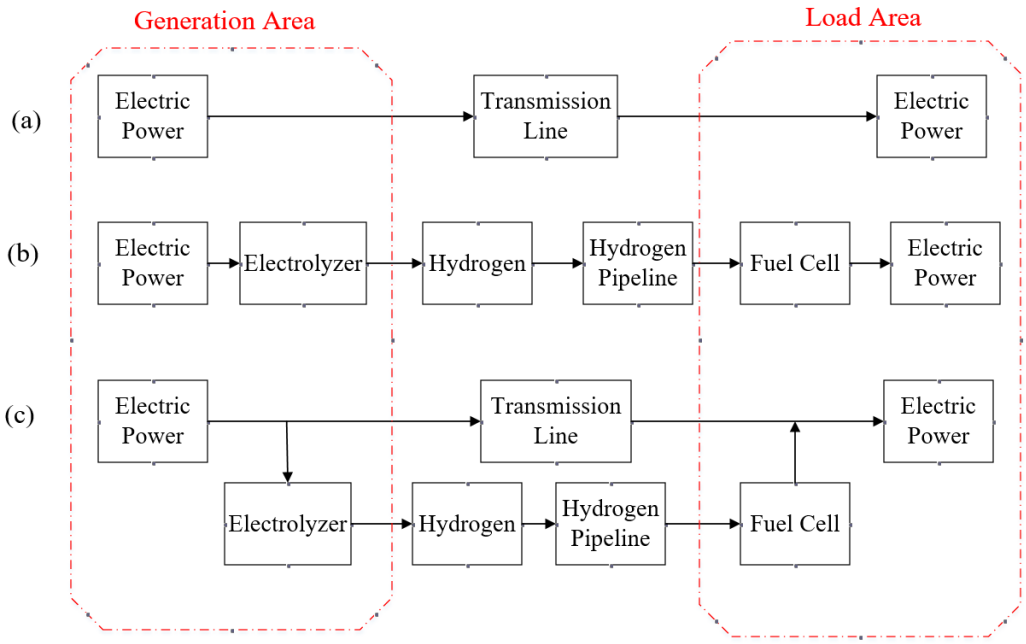

Fig. 5.10. Different transmission configurations: (a) electrical transmission (b) hydrogen transmission (c) hybrid transmission.

Electrical transmission energy losses are mainly Joule losses, which are 2-3% of the total power transmitted [156]. In contrast, hydrogen transmission, involving electric-to-hydrogen energy conversion, experiences round-trip conversion losses exceeding 50% under ideal conditions. Therefore, in current scenarios, electrical transmission is often more practical and advantageous than hydrogen transmission. However, in future grids with excess renewable energy that may be simply curtailed and thus wasted, the significance of transmission losses may diminish, making hydrogen or hybrid transmission viable alternatives. These methods can ensure utilization of renewable energy that might otherwise be curtailed. Hybrid transmission

leverages both electric and hydrogen transmission facilities, potentially achieving a higher maximum transfer capacity — the sum of the capacities of both electrical and hydrogen transmission. This configuration becomes increasingly relevant when existing transmission lines require additional capacity, which can be supplemented by new hydrogen transmission facilities during expansion.

Future renewable grids may employ these three transmission configurations to expand transmission capabilities in various local areas and scenarios. Electric transmission investments might be prioritized where significant capacity is needed, and less loss of transmission is required. Hydrogen transmission could be more suitable in areas where existing natural gas pipelines can be upgraded for hydrogen transmission or for long-distance transmission from renewable generation sites, depending on advancements in hydrogen technology. Hybrid transmission could be implemented when a new hydrogen pipeline is constructed alongside an existing electrical transmission line. Moreover, determining optimal sending and receiving locations for transmission is not straightforward. Reference [116] suggests that the ideal receiving location for hydrogen transmission, also the location of fuel cells, may be a transitional area between load and generation zones. An example follows to elucidate the concept of transmission expansion with hybrid transmission and to illustrate the scenarios where such transmission is beneficial.

In Fig. 5.11 (a), an electrical transmission line transfers the electric power to meet 950 MW load demand. In the future, the load demand is expected to reach 1,450 MW in some peak load conditions, and 1,000 MW renewables are deployed in the

generation area. In this case, we can invest in the transmission facilities illustrated in Fig. 5.11 (b), which is equivalent to transferring 500 MW electrical power and it is represented by the blue line in Fig. 5.11 (b). In this case, we assume the round-trip efficiency of hydrogen transmission is 50%, and the increased load is covered by the developed renewables and the hydrogen transmission. With this transmission investment, the combined transmission in Fig. 5.11 (b) is considered a form of hybrid transmission. If there is an existing natural gas line between the two buses, this transmission investment becomes even more economically advantageous.

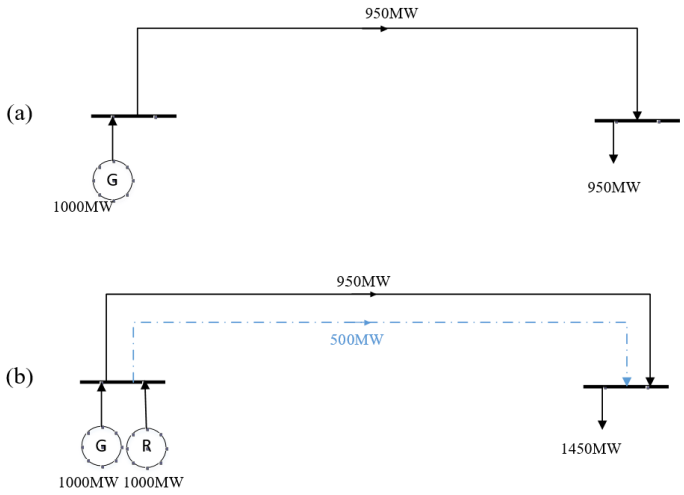

Fig. 5.11. (a) An example of point-to-point transmission (b) The future scenario with hydrogen transmission investment.

During periods of low demand, for certain seasons or times of day, hydrogen facilities can be used to produce hydrogen, utilizing surplus renewable energy. This hydrogen can then supply both bus locations. Fig. 5.12 demonstrates this scenario, where the natural gas power plant operates at its minimum output, and renewable

energy covers additional loads not met by natural gas generation, while also producing hydrogen for both locations.

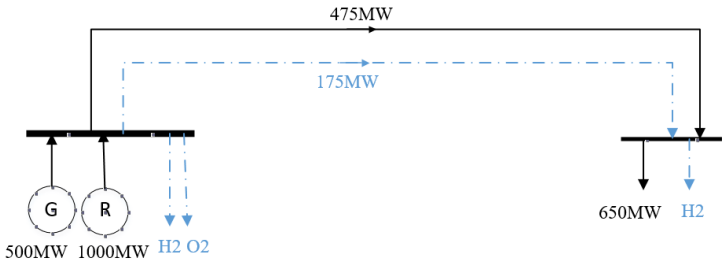

Fig. 5.12. The hydrogen facilities provide H2 to both locations in low demand time.

5.4.2 TEP with Hydrogen Transmission Facilities

Transmission expansion is a crucial long-term planning problem aimed at identifying optimal transmission investment for future periods. The future grids upgraded with the transmission investments should remain reliable throughout all planned periods, and minimize instances of load shedding. Reliability, while fundamental to TEP, is not the sole consideration. Cost-effectiveness is equally important, encompassing both the system-wide operational costs and the capital costs of new transmission investments. The objective function of TEP-H and the related costs calculation are shown as follows:

$$\min C^{\mathrm{NL}} + C^{\mathrm{G}} + C^{\mathrm{H}} + M * \sum_{n\in N, t\in T, d\in D^{T}, p\in P} p^{\mathrm{SD}}_{b,t,d,p} \tag{5.46}$$

$$C^{\mathrm{G}} = N^{\mathrm{Y}} * B^{\mathrm{MVA}} * \frac{365}{N^{\mathrm{D}}} * \sum_{g\in G, t\in T, d\in D^{T}, p\in P} p^{\mathrm{G}}_{g,t,d,p} * C^{\mathrm{G}}_{g} \tag{5.47}$$

$$+N^{\mathrm{Y}} * B^{\mathrm{MVA}} * \frac{365}{N^{\mathrm{D}}} * \sum_{g \in NG, t \in T, d \in D^{T}, p \in P} p_{g,t,d,p}^{\mathrm{NG}} * C_{g}^{\mathrm{NG}},$$

$$C^{\mathrm{NL}} = \sum_{k \in NL, p \in P} V_{k,p}^{\mathrm{NL}} * C_{k}^{\mathrm{NL}} * (1 + (N^{\mathrm{P}} - p + 1) * R^{\mathrm{M}} * N^{\mathrm{Y}}), \tag{5.48}$$

$$\text{and } C^{\mathrm{H}} = \sum_{h \in H, p \in P} V_{h,p}^{\mathrm{H}} * C_{h}^{\mathrm{H}} * (1 + (N^{\mathrm{P}} - p + 1) * R^{\mathrm{MH}} * N^{\mathrm{Y}}) \tag{5.49}$$

$$+ \sum_{h \in H, p \in P} V_{h,p}^{\mathrm{H}} * C_{h}^{\mathrm{F}} + \sum_{h \in H, p \in P} V_{h,p}^{\mathrm{H}} * C_{h}^{\mathrm{E}}.$$

In TEP-H, the planning encompasses multiple representative periods, each spanning N^{Y} years, under the assumption that grid conditions remain relatively consistent throughout these years. Each period includes four typical days, symbolizing different seasonal conditions within a year. The objective function of TEP-H, as shown in Equation (5.46), comprises various cost components: the production cost of thermal generator C^{G}, the capital cost of new transmission line C^{NL}, the capital cost of hydrogen facilities C^{H}, and a penalty term for the load sheddings. The penalty term includes the load shedding amount along all the periods $p_{b,t,d,p}^{\mathrm{SD}}$, and a big number M as weight coefficient.

The thermal generator production cost C^{G} accounts for the total operation costs of both existing and future generators, as detailed in Equation (5.47). The total cost of new lines C^{NL} outlined in Equation (5.48), includes both initial capital and ongoing maintenance costs. Here, $V_{k,p}^{\mathrm{NL}}$ is a binary variable indicating the construction of a candidate line k during a specific period p. Once constructed, line k incurs maintenance costs for $N^{P} - p + 1$ periods, with these costs being proportional to the

initial capital expense. Equation (5.49) details the capital costs associated with hydrogen facilities, encompassing pipelines, fuel cells, and electrolyzers, applicable when a candidate hydrogen pipeline is slated for construction.

In an electrical transmission system, each node should be power balanced. This balance is given by

$$\begin{aligned}
&\sum_{j\in L^{T(n)}} p^{\mathrm{L}}_{j,t,d,p} - \sum_{j\in L^{F(n)}} p^{\mathrm{L}}_{j,t,d,p} + \sum_{j\in NL^{T(n)}} p^{\mathrm{NL}}_{j,t,d,p} \\
&- \sum_{j\in NL^{F(n)}} p^{\mathrm{NL}}_{j,t,d,p} + \sum_{g\in G^{B(n)}} p^{\mathrm{G}}_{g,t,d,p} + \sum_{g\in NG^{B(n)}} p^{\mathrm{NG}}_{g,t,d,p} \\
&+ \sum_{r\in R^{B(n)}} p^{\mathrm{R}}_{r,t,d,p} + p^{\mathrm{NR}}_{n,t,d,p} - \sum_{r\in R^{B(n)}} p^{\mathrm{RCUR}}_{r,t,d,p} - p^{\mathrm{NR,CUR}}_{n,t,d,p} \\
&+ \sum_{h\in H^{F(n)}} p^{\mathrm{F}}_{h,t,d,p} - \sum_{h\in H^{E(n)}} p^{\mathrm{E}}_{h,t,d,p} - \sum_{h\in H^{C(n)}} p^{\mathrm{C}}_{h,t,d,p} = p^{\mathrm{LOAD}}_{n,t,d,p} - p^{\mathrm{SD}}_{n,t,d,p} \\
&\forall n \in B, t \in T, d \in D^T, p \in P.
\end{aligned} \tag{5.50}$$

On each node, the power $p^{\mathrm{L}}_{j,t,d,p}$ flows along transmission lines connected to it. Additionally, power flowing on new transmission lines, represented by $p^{\mathrm{NL}}_{j,t,d,p}$, is also taken into account. The power generated by existing and new generators or renewable power plants are symbolized by $p^{\mathrm{G}}_{g,t,d,p}$, $p^{\mathrm{NG}}_{g,t,d,p}$, $p^{\mathrm{R}}_{r,t,d,p}$, $p^{\mathrm{NR}}_{n,t,d,p}$. Given the possibility of high renewable energy penetration in future grids, there may be instances where renewable production has to be curtailed to ensure matching between system load and generation. This curtailment is represented by $p^{\mathrm{RCUR}}_{r,t,d,p}$ and $p^{\mathrm{NR,CUR}}_{n,t,d,p}$. The power generated or consumed by fuel cell, electrolyzers, and compressors are

represented by $p^{\mathrm{F}}_{h,t,d,p}$, $p^{\mathrm{E}}_{h,t,d,p}$, and $p^{\mathrm{C}}_{h,t,d,p}$. The load demand and shedding are represented by $p^{\mathrm{LOAD}}_{n,t,d,p}$ and $p^{\mathrm{SD}}_{n,t,d,p}$.

The maximum amount of load shedding and the renewable curtailment are described by Constraints as follows:

$$0 \le p^{\mathrm{SD}}_{b,t,d,p} \le p^{\mathrm{LOAD}}_{n,t,d,p} \quad \forall n,t,d,p \in N,T,D^T,P, \tag{5.51}$$

$$0 \le p^{\mathrm{RCUR}}_{r,t,d,p} \le p^{\mathrm{R}}_{r,t,d,p} \quad \forall r,t,d,p \in R,T,D^T,P, \tag{5.52}$$

$$\text{and } 0 \le p^{\mathrm{NR,CUR}}_{r,t,d,p} \le p^{\mathrm{NR}}_{r,t,d,p} \quad \forall r,t,d,p \in NR,T,D^T,P. \tag{5.53}$$

Besides, the maximum thermal generation output power and the renewable production are described as follows:

$$\mathrm{p}^{\mathrm{Min}}_{g} \le \mathrm{p}^{\mathrm{G}}_{g,t,d,p} \le \mathrm{p}^{\mathrm{Max}}_{g} \quad \forall \mathrm{g,t,d,p} \in \mathrm{G,T,D^T,P}, \tag{5.54}$$

$$p^{\mathrm{Min}}_{g,p} \le p^{\mathrm{NG}}_{g,t,d,y} \le p^{\mathrm{Max}}_{g,p} \quad \forall g,t,d,p \in NG,T,D^T,P, \tag{5.55}$$

$$p^{\mathrm{Min,R}}_{r} \le p^{\mathrm{R}}_{r,t,d,p} \le p^{\mathrm{Max,R}}_{r,t,d,p} \; \forall r,t,d,p \in R,T,D^T,P, \tag{5.56}$$

$$p^{\mathrm{Min,NR}}_{r} \le p^{\mathrm{NR}}_{r,t,d,y} \le p^{\mathrm{Max,NR}}_{r,t,d,p} \tag{5.57}$$

$$\forall r \in NR, t \in T, d \in D^T, p \in P.$$

Other constraints in TEP-H are shown as follows:

$$-p^{\mathrm{Max}}_{k,t,d,p} \le p^{L}_{k,t,d,p} \le p^{\mathrm{Max}}_{k,t,d,p} \tag{5.58}$$

$$\forall k \in L, t \in T, d \in D^T, p \in P,$$

$$p^{\mathrm{L}}_{k,t,d,p} = \frac{\theta^{\mathrm{F}}_{k,t,d,p} - \theta^{\mathrm{T}}_{k,t,d,p}}{x^{\mathrm{L}}_{k}} \tag{5.59}$$

$$\forall k \in L, t \in T, d \in D^T, p \in P,$$

$$-M * (1 - u_{k,p}^{\mathrm{NL}}) \leq p_{k,t,d,p}^{\mathrm{NL}} - \frac{\theta_{k,t,d,p}^{\mathrm{F}} - \theta_{k,t,d,p}^{\mathrm{T}}}{x_k^{\mathrm{NL}}} \leq M * \left(1 - u_{k,p}^{\mathrm{NL}}\right), \tag{5.60}$$

$$\forall k \in NL, t \in T, d \in D^T, p \in P,$$

$$-p_{k,t,d,p}^{\mathrm{Max,NL}} * u_{k,p}^{\mathrm{NL}} \leq p_{k,t,d,p}^{\mathrm{NL}} \leq p_{k,t,d,p}^{\mathrm{Max,NL}} * u_{k,p}^{\mathrm{NL}} \tag{5.61}$$

$$\forall k \in NL, t \in T, d \in D^T, p \in P,$$

$$\sum_{p' \in P, p' \leq p} u_{k,p'}^{\mathrm{NL}} \leq u_{k,p}^{\mathrm{NL}} \quad \forall k \in NL, p \in P, \tag{5.62}$$

$$v_{k,p}^{\mathrm{NL}} \geq u_{k,p}^{\mathrm{NL}} - u_{k,p-1}^{\mathrm{NL}}, \forall k \in NL, p \in P, p > 1, \tag{5.63}$$

$$v_{k,1}^{\mathrm{NL}} = u_{k,1}^{\mathrm{NL}} \quad \forall k \in NL, \tag{5.64}$$

$$\eta_h^{\mathrm{E}} * p_{h,t,d,p}^{\mathrm{E}} * B^{\mathrm{MVA}} * \Delta t = h_{h,t,d,p}^{\mathrm{H}} \tag{5.65}$$

$$\forall h \in H, t \in T, d \in D^T, p \in P,$$

$$\eta_h^{\mathrm{F}} * h_{h,t,d,p}^{\mathrm{H}} * B^{\mathrm{MVA}} = p_{h,t,d,p}^{\mathrm{E}} * \Delta t \tag{5.66}$$

$$\forall h \in H, t \in T, d \in D^T, p \in P,$$

$$\eta_h^{\mathrm{C}} * h_{h,t,d,p}^{\mathrm{H}} = p_{h,t,d,p}^{\mathrm{C}} * B^{\mathrm{MVA}} * \Delta t \tag{5.67}$$

$$\forall h \in H, t \in T, d \in D^T, p \in P,$$

$$h_{h,t,d,p}^{\mathrm{H}} \leq h_h^{\mathrm{Max}} * u_{h,y}^{\mathrm{H}} \tag{5.68}$$

$$\forall h \in H, t \in T, d \in D^T, p \in P,$$

$$p_{h,t,d,p}^{\mathrm{E}} \leq p_h^{\mathrm{E,Max}} * u_{h,y}^{\mathrm{H}} \tag{5.69}$$

$$\forall h \in H, t \in T, d \in D^T, p \in P,$$

$$p_{h,t,d,p}^{\mathrm{F}} \leq p_h^{\mathrm{F,Max}} * u_{h,y}^{\mathrm{H}} \tag{5.70}$$

$$\forall h \in H, t \in T, d \in D^T, p \in P,$$

$$\sum_{p' \le p} v^{\mathrm{H}}_{h,p'} \le u^{\mathrm{H}}_{h,p} \quad \forall h \in H, \tag{5.71}$$

$$v^{\mathrm{H}}_{h,p} \ge u^{\mathrm{H}}_{h,p} - u^{\mathrm{H}}_{h,p-1}, \forall h \in H, p \in P, p > 1, \tag{5.72}$$

$$\text{and } v^{\mathrm{H}}_{h,1} = u^{\mathrm{H}}_{h,1} \quad \forall h \in H. \tag{5.73}$$

Power flow on transmission lines must adhere to thermal limits as outlined in (5.58) – (5.59). For candidate transmission lines, power flow constraints become applicable only after their construction, as specified in Equation (5.60). Equation (5.61) ensures that the maximum power flow on an unbuilt candidate line is zero. The binary variables governing candidate transmission lines are further constrained by Constraints (5.62) – (5.64). Efficiency of conversions between electrical and hydrogen energy, involving electrolyzers and fuel cells, is modeled through Constraints (5.65) – (5.66). Moreover, compressors consume electrical energy to pressurize hydrogen for pipeline transmission, as detailed in Constraint (5.67). Hydrogen pipelines, electrolyzers, and fuel cells have maximum transmission and working power capacities, respectively, as described in Constraints (5.68) – (5.70). Constraints for binary variables associated with candidate hydrogen facilities are laid out in Constraints (5.71) – (5.73).

The TEP-H model takes into account long-term variations in renewable production $p^{\mathrm{Max,R}}_{r,t,d,p}$, load $p^{\mathrm{LOAD}}_{n,t,d,p}$, and dynamic line ratings $p^{\mathrm{Max}}_{k,t,d,p}$ over the planning period. Based on these projections, TEP-H determines the construction and online status of both electric and hydrogen transmission investments, represented by variables $v^{\mathrm{NL}}_{k,p}$, $u^{\mathrm{NL}}_{k,p}$, $v^{\mathrm{H}}_{h,p}$, and $u^{\mathrm{H}}_{h,p}$. The model outputs future grid operation

conditions, including renewable curtailment $p^{\mathrm{RCUR}}_{r,t,d,p}$, load shedding $p^{\mathrm{SD}}_{b,t,d,p}$, generation dispatching $p^{\mathrm{G}}_{g,t,d,p}$, and both electric power flow $p^{\mathrm{L}}_{k,t,d,p}$ and hydrogen flow $h^{\mathrm{H}}_{h,t,d,p}$ in the hybrid system for various scenarios. It also calculates the system's operational and investment costs, including thermal generator production cost C^{G}, new transmission line capital cost C^{NL}, and hydrogen facilities capital cost C^{H}, thereby providing a comprehensive view of transmission investments, future grid operations, and associated costs.

To validate TEP-H and compare transmission investments with and without hydrogen facilities, a traditional TEP model (TEP-T) is also formulated. TEP-T, similar in structure to TEP-H but excluding hydrogen-related constraints, omits hydrogen facility costs in its objective function, which can be expressed as

$$\min C^{\mathrm{NL}} + C^{\mathrm{G}} + M * \sum_{n\in N, t\in T, d\in D^{T}, p\in P} p^{\mathrm{SD}}_{b,t,d,p}. \tag{5.74}$$

TEP-T also excludes electrical energy generated or consumed by fuel cells and electrolyzers in its power balance, which is given by

$$\begin{aligned} &\sum_{j\in L^{T(n)}} p^{\mathrm{L}}_{j,t,d,p} - \sum_{j\in L^{F(n)}} p^{\mathrm{L}}_{j,t,d,p} + \sum_{j\in NL^{T(n)}} p^{\mathrm{NL}}_{j,t,d,p} \\ &- \sum_{j\in NL^{F(n)}} p^{\mathrm{NL}}_{j,t,d,p} + \sum_{g\in G^{B(n)}} p^{\mathrm{G}}_{g,t,d,p} + \sum_{g\in NG^{B(n)}} p^{\mathrm{NG}}_{g,t,d,p} \\ &+ \sum_{r\in R^{B(n)}} p^{\mathrm{R}}_{r,t,d,p} + p^{\mathrm{NR}}_{n,t,d,p} - \sum_{r\in R^{B(n)}} p^{\mathrm{RCUR}}_{r,t,d,p} - p^{\mathrm{NR,CUR}}_{n,t,d,p} \\ &= p^{\mathrm{LOAD}}_{n,t,d,p} - p^{\mathrm{SD}}_{n,t,d,p,} \end{aligned} \tag{5.75}$$

$$\forall n \in B, t \in T, d \in D^T, p \in P.$$

The complete formulations of both TEP-T and TEP-H are summarized in Table 5.17.

Table 5.17 The Model Formulations of TEP-T and TEP-H.

Proposed TEP-H	Benchmark TEP-T
(5.46) – (5.73)	(5.47) – (5.48), (5.51) – (5.64), (5.74) – (5.75)

5.4.3 Case Studies

The effectiveness of TEP-H, like many other planning strategies, hinges on reliable prediction data for different grid sections. However, due to the sensitivity and confidentiality of power system data, obtaining such information can be challenging or necessitate confidential authorization. A notable exception is the TX-123BT test system created in Chapter 4. This dataset provides detailed renewable and thermal generation data at the facility level, along with transmission network and dynamic line rating data at the nodal or line level. Consequently, TX-123BT serves as the test system for our TEP-H simulations. We conducted the TEP-H simulations using Python with the Pyomo package. As TEP-H is a mixed-integer linear programming (MILP) problem, we employed the Gurobi solver, setting the optimality gap at 0.1%.

TEP-H necessitates predictions of future hydrogen-related conditions, such as capital costs for hydrogen facilities and the efficiency of fuel cells and electrolyzers. These parameters critically influence the investment decisions of hydrogen transmission and the co-expansion of hydrogen and electric transmission system.

Hydrogen technology, being state-of-the-art and rapidly evolving, presents challenges in accurately predicting future developments and conditions. Therefore, we conducted TEP-H simulations under various hydrogen technology development scenarios, providing insights into how advancements in hydrogen technology might influence the expansion of future renewable grids. A key aspect of hydrogen improvements is the round-trip efficiency, representing the efficiency of converting electrical energy to hydrogen and then back to electrical energy via electrolyzers and fuel cells. For instance, with an electrolyzer efficiency of 60% and a fuel cell efficiency of 80%, the round-trip efficiency would be 48%. Since renewable energy may offset the low efficiency issues of the hydrogen transmission, renewable penetration is also an important factor for TEP with hydrogen transmission investment.

Our first investigation focused on identifying the renewable penetration level at which hydrogen becomes a feasible solution for future grid transmission. We ran TEP-H simulations on the TX-123BT with varying levels of renewable penetration, assuming a round-trip efficiency of 40%, indicative of the most ideal current hydrogen technology. The findings, presented in Table 5.18, suggest that hydrogen transmission becomes more viable in grids with high renewable penetration. Under the most ideal conditions for current hydrogen technology, hydrogen transmission is feasible at a renewable penetration level of around 60%.

Table 5.18 The Hydrogen Transmission Investment for TX-123BT with Various Renewable Penetrations

Renewable Penetration Level	Number of Hydrogen Pipelines	Construction Period	Total Hydrogen Investment (Million $)
40%	0	N/A	0

Table 5.18 Continued

60%	1	2036-2040	2,050
80%	1	2031-2035	2,065

In our second set of simulations, we explored the TEP-H model under various assumptions regarding advancements in hydrogen technology, focusing on aspects such as round-trip efficiency and the costs of hydrogen facilities. Notably, we discovered that the efficiency of fuel cells and electrolyzers plays a more critical role in the application of hydrogen transmission compared to reductions in capital and maintenance costs of hydrogen facilities. This is because conversion efficiency is directly tied to the potential waste of a large amount of generated energy, which poses a greater economic burden than the costs associated with hydrogen facilities. Our findings, detailed in Tables 5.19 – 5.20, illustrate the investment trends in hydrogen transmission against different round-trip efficiency levels. Notably, higher round-trip efficiency leads to increased investment in hydrogen transmission, particularly when efficiency levels approach 70%-80%.

Table 5.19 The Hydrogen Investments for Various Round-trip Efficiency When Renewable Penetration Level is 80%

Round Trip Efficiency	Number of Hydrogen Pipelines	Construction Period	Total Hydrogen Investment (Million $)
40%	1	2031-2035	2,065
50%	1	2031-2035	2,065
60%	1	2031-2035	2,065
70%	2	2031-2035, 2036-2040	4,127
80%	4	2021-2025, 2031-2035, 2036-2040, 2031-2035	8,418

Table 5.20 The Hydrogen Investments for Various Round-trip Efficiency When Renewable Penetration Level is 60%

Round Trip Efficiency	Number of Hydrogen Pipelines	Construction Period	Total Hydrogen Investment (Million $)
40%	1	2036-2040	2,050
50%	1	2041-2045	2,035
60%	1	2031-2035	2,065
70%	1	2036-2040	2,050
80%	3	2036-2040, 2041-2045, 2036-2040	6,201

The TEP-H simulations under various round-trip efficiency and cost assumptions revealed that when round-trip efficiency is low, the cost of hydrogen facilities has minimal impact on hydrogen transmission investment decisions. However, as the round-trip efficiency escalates to 70%-80%, cost reduction becomes a significant factor influencing hydrogen investment decisions. The investments under various cost reduction scenarios are presented in Table 5.21.

Table 5.21 The Hydrogen Investments for Various Cost Reduction With 60% Renewable Penetration Level and 70% Round-trip Efficiency

Hydrogen Facilities Cost Reduction	Number of Hydrogen Pipelines	Total Hydrogen Investment (Million $)
0%	2	4,127
20%	2	3,301
40%	2	2,476
60%	3	2,514
80%	3	1,257

We also compared the future grid conditions under both TEP-T and TEP-H investments, focusing on scenarios where the renewable penetration level is high (60%). For this comparison, we assumed a 40% round-trip efficiency in the TEP-H simulation. The results of this simulation, as illustrated in Table 5.22, show that TEP-H involves investment in hydrogen transmission and requires less electrical transmission investment compared to TEP-T. The total cost for TEP-H amounted to 473,965 million dollars, which is 3,029 million dollars less than that of TEP-T.

Table 5.22 The Transmission Investments by TEP-H and TEP-T

TEP Model	TEP-T	TEP-H
Number of Hydrogen Pipeline	N/A	1
Hydrogen Investments (M$)	N/A	2,050
Transmission Line Number	11	8
Transmission Investments (M$)	4,285	3,433
Generation Costs (M$)	469,680	465,453
Total Costs (M$)	473,965	470,936

Further analysis was conducted on the grid operation conditions of the TX-123BT under TEP-H investments, with a scenario where renewable penetration is very high (80%) and hydrogen technology has significantly improved (80% round-trip efficiency). The detailed expansion planning for hydrogen transmission as determined by TEP-H is displayed in Table 5.23. The various associated costs are listed in Table 5.24. Notably, the generation cost, accounting for planning over 30 years and all

thermal power plants in the ERCOT, is substantially larger than the transmission investment cost.

Table 5.23 The Planning of Hydrogen Transmission

Hydrogen Pipeline Number	Construction Period	From Bus Number	To Bus Number
1	2021-2025	98	1
2	2031-2035	98	1
3	2036-2040	91	31
6	2031-2035	78	63

Table 5.24 The Operation and Investment Costs

Total Cost	Generation Cost	Hydrogen Facilities Investment
467.43B	459.02B	8.41B

TEP-H also provides scheduled operations for hydrogen transmission. The daily hydrogen transmission and associated operations of fuel cells and electrolyzers for a typical day in Quarter I, spanning the years 2046-2050, are depicted in Fig. 5.13 and Fig. 5.14.

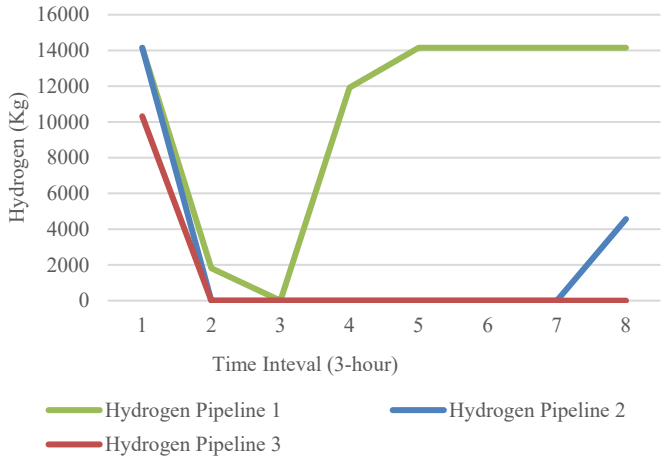

Fig. 5.13. Daily operation of hydrogen pipelines in Quarter I, 2046-2050.

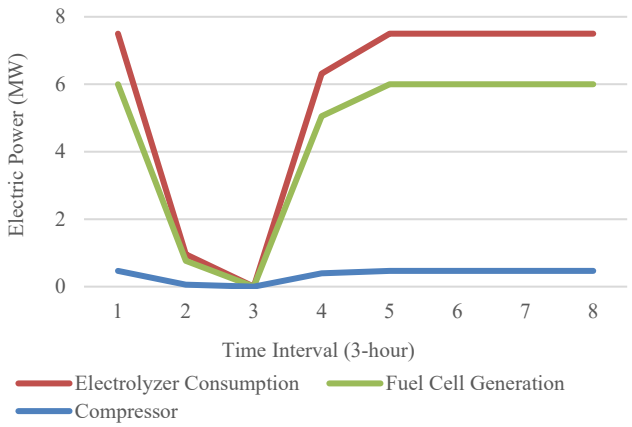

Fig. 5.14. Daily operation of fuel cells, electrolyzers and compressors in Quarter I, 2046-2050.

5.5 Summary

The proposed TEP-CI addresses the weather and climate impact on the future power system. The improved TEP-CI model is proposed by considering the representative profiles in each planning epoch. The SCUC simulations are conducted on the future grids under different investment cases including FR, FGI, and FGTI. The reliability indices are proposed and calculated for each future planning epoch based on the daily operation conditions. The reliability of the grid under FR, FGI, and FGTI are compared and analyzed.

The proposed TEP-H model delves into the expansion planning for renewable energy grids, with a particular focus on integrating both electric and hydrogen transmissions. The proposed TEP-H model accounts for hydrogen facilities related physical constraints and long-term shifts in future grids, enabling the determination of an optimal investment plan for both electric and hydrogen transmission. This approach aims to minimize the total system costs, encompassing both operational expenses and

expansion investments, while striving to maintain system reliability. The proposed TEP-H model incorporates constraints of both power grids and hydrogen facilities, including hydrogen pipelines, electrolyzers, and fuel cells. By including capital and maintenance costs of these hydrogen facilities, TEP-H can evaluate the hydrogen transmission from the economic aspect.

Since the hydrogen related costs and the conversion efficiency are modeled in TEP-H, we are able to figure out the how the hydrogen technology improvement will influence the future hydrogen integration in the renewable grids. Based on the numerical results of TEP-H simulations on the TX-123BT, we confirm that electric-hydrogen energy conversion efficiency is the key point for the hydrogen to be applied to the future grids. TEP-H lays the groundwork and can serve as a benchmark for other planning strategies in hydrogen integration into renewable grids. It also paves the way for the industry level prospecting on practical applications of hydrogen in renewable enriched future grids.

6. ENHANCING POWER SYSTEM RESTORATION WITH FUEL CELLS AS BLACK START RESOURCES

6.1 Literature Review

With the development and expansion of the power system, grid reliability and resilience are of vital significance. However, a number of large-scale blackouts still occur around the world. Many different factors can cause a blackout, such as natural disasters and equipment failure [157]. An effective power restoration strategy is one of the keys to achieving a resilient bulk power system against outages.

The aim of the restoration strategy is to restore the maximum loads in the shortest time under the power system safety constraints. Power system restoration is a multi-objective, multi-stage, multi-variable and multi-constraint optimization problem [158]. Traditionally, the restoration process is separated into three stages: black-start, network reconfiguration and load restoration. In the black-start stage, the non-black-start (NBS) generators will be recovered by utilizing the black-start generator. In the network reconfiguration stage, a stable backbone network with majority substations is established to enable load restoration in the next stage. In the load restoration stage, large-scale load restoration can be carried out [159]. Reference [160] proposes a general restoration strategy consisting of six restoration steps called generic restoration milestones. In [161], a two-stage adaptive restoration decision support system is proposed. The optimal planning function determines the operation sequence and the optimal real-time function adjusts values of generation and load pickup. In addition to the research on the entire restoration process, many studies focus on a

single stage of the restoration. For instance, [162]–[165] investigate the black-start stage to find the generator start-up sequence (GSUS); [166]–[168] explore the network reconfiguration stage while [169]–[171] examine the load pickup stage.

Many studies focus on utilizing batteries for black start [172]–[173]. For the hydrogen-integrated grids, an operation strategy in [174] focus on the proactive scheduling of hydrogen facilities, particularly for the distribution network to enhance the grid reliability. Few existing studies utilize fuel cells as black-start resources to facilitate the black start process.

In the second stage of power system restoration, the reconstruction of the backbone network can be divided into two steps: (a) determine the target skeleton-network and (b) identify the optimal restoration sequence of the network determined in the previous step. A number of prior works have been conducted to determine the target network. In [175], it introduces node importance degree to evaluate the importance for every single bus. The network reconfiguration efficiency is defined based on the node importance degree and the average clustering coefficient of the network. The target skeleton-network with maximum network reconfiguration efficiency is obtained using discrete particle swarm optimization. In [176], it defines a new network index considering both node importance and line charging reactive power, the target skeleton-network is obtained by genetic algorithm. In [177], it defines a new network index as a linear combination of four different network indexes considering the cost of blackout in market environments. In [178], seven types of network indexes are synthesized using criteria importance through intercriteria

correlation to comprehensively evaluate the node importance. In [179], it identifies the network restoration sequence based on the determined target network. It proposes a comprehensive skeleton-network restoration strategy that includes three models for GSUS, skeleton-network and load pickup respectively. A traditional skeleton-network model, namely the transmission line restoration (TLR) model, is used in [179] and it can attain the restoration sequence based on the target network obtained by the method in [175] and the GSUS solution achieved from the GSUS model. However, the skeleton-network obtained by [169] does not consider its restoration performance such as the total restoration time of the skeleton-network.

6.2 Black Start Strategy for Hydrogen-integrated Renewable Grids

Modern power systems integrate various clean generation sources and utilize storage solutions to enhance grid resilience and mitigate associated challenges. For power system restoration, black start may now leverage these new technologies, such as fuel cells in hydrogen hybrid systems and battery storage. This study proposes black start models for grids incorporating fuel cells and battery storage, focusing on their distinct characteristics and contributions. The models address the restoration of electrical grids, including energization paths and time of transmission network, and specific traits of fuel cells and battery storage as black start resources. Key considerations include the power output characteristics of fuel cells and the energy storage capacity of batteries, meticulously integrated into each model. Black start simulations are performed on the IEEE 39-bus system, comparing the generator startup sequence (GSUS) for systems equipped with fuel cells versus batteries.

Sensitivity analyses on fuel cell capacity, battery storage capacity and initial SOC, and resource locations are conducted to determine the most suitable scenarios for black start operations.

6.2.1 Black Start Model Considering Fuel Cells as BS Resources

During a blackout, generators may shut down and transmission lines may become deenergized, resulting in significant load unserved. A resilient power system should quickly recover from a total blackout and restore service to all loads. The first critical step is to start all shutdown power plants as soon as possible, as restoring generation capability is essential for energizing the transmission infrastructure and facilitating further load pickup.

For the black start stage, the objective is to restore all the generation capability as soon as possible, which is given by

$$\min \sum_{g \in G} \sum_{t \in} \left(p_g^{max} - p_g^{start}\right) \cdot t_g^{start} - \beta \cdot \sum_{b \in B} \sum_{t \in T} \frac{\left(u_{b,t}^{B} \cdot D_b\right)}{t}, \tag{6.1}$$

where p_g^{max} is the maximum generation power of a power plant, and p_g^{start} is the cranking power required by the plant. t_g^{start} is the time it takes for the power plant to start up after the blackout. The second term prioritizes the restoration of critical loads on specific buses, with $u_{b,t}^{B}$ as a binary variable indicating whether bus b is restored as time t. Besides, D_b is the bus importance degree of bus b, and β is the weight coefficient for the second term.

At any given time, the restored generation resources, including fuel cells, should be sufficient for the cranking power required to start up generators. It is described as

$$\sum_{g} p_{g,t} + \sum_{f} p_{f,t} \geq 0 \qquad \forall t \in T. \tag{6.2}$$

The minimum and maximum time limitations for starting up a power plant successfully are described by

$$t_g^{start} \geq t_g^{Min} \qquad \forall g \in G \tag{6.3}$$

$$\text{and } t_g^{start} \leq t_g^{Max} \qquad \forall g \in G. \tag{6.4}$$

We use binary variables $u_{f,t}^{start}$, $u_{f,t}^{on}$, $u_{f,t}^{max}$ to indicate different generation status of the fuel cell *f*. When $u_{f,t}^{start}$ is 1, it indicates the fuel cell is starting up. When $u_{f,t}^{on}$ is 1, it indicates the fuel cell is generating power. When $u_{f,t}^{max}$ is 1, it indicates fuel cell is operating at the high end of its range. In order to model the actual generation power from fuel cells injected into the grid, the multiplication of binary variables will be required. In order to linearize it, three ancillary variables $y_{f,t1,t2}^{start}$, $y_{f,t1,t2}^{on}$, $y_{f,t1,t2}^{max}$ are utilized. The definition and constraints for these variables are described as follows:

$$y_{f,t1,t2}^{start} = u_{f,t1}^{start} \cdot u_{f,t2}^{start} \qquad \forall f \in F, t1, t2 \in T, \tag{6.5}$$

$$y_{f,t1,t2}^{start} \geq u_{f,t1}^{start} + u_{f,t2}^{start} - 1 \qquad \forall f \in F, t1, t2 \in T, \tag{6.6}$$

$$y_{f,t1,t2}^{start} \leq u_{f,t1}^{start} \qquad \forall f \in F, t1, t2 \in T, \tag{6.7}$$

$$y_{f,t1,t2}^{start} \leq u_{f,t2}^{start} \qquad \forall f \in F, t1, t2 \in T, \tag{6.8}$$

$$y_{f,t1,t2}^{on} = u_{f,t1}^{on} \cdot u_{f,t2}^{on} \quad \forall f \in F, t1, t2 \in T, \tag{6.9}$$

$$y_{f,t1,t2}^{on} \geq u_{f,t1}^{on} + u_{f,t2}^{on} - 1 \quad \forall f \in F, t1, t2 \in T, \tag{6.10}$$

$$y_{f,t1,t2}^{on} \leq u_{f,t1}^{on} \quad \forall f \in F, t1, t2 \in T, \tag{6.11}$$

$$y_{f,t1,t2}^{on} \leq u_{f,t2}^{on} \quad \forall f \in F, t1, t2 \in T, \tag{6.12}$$

$$y_{f,t1,t2}^{max} = u_{f,t1}^{max} \cdot u_{f,t2}^{max} \quad \forall f \in F, t1, t2 \in T, \tag{6.13}$$

$$y_{f,t1,t2}^{max} \geq u_{f,t1}^{max} + u_{f,t2}^{max} - 1 \quad \forall f \in F, t1, t2 \in T, \tag{6.14}$$

$$y_{f,t1,t2}^{max} \leq u_{f,t1}^{max} \quad \forall f \in F, t1, t2 \in T, \tag{6.15}$$

$$\text{and } y_{f,t1,t2}^{max} \leq u_{f,t2}^{max} \quad \forall f \in F, t1, t2 \in T. \tag{6.16}$$

The operation times at different stages of fuel cell generation are constrained as follows:

$$T - \sum_{t} u_{f,t}^{start} \geq T_t^N \cdot \left(1 - u_{f,t}^{start}\right) \quad \forall f \in F, t \in T, \tag{6.17}$$

$$\begin{aligned} T \cdot u_{f,t2}^{start} - T \cdot u_{f,t2}^{on} - \sum_{t1 \in T} y_{f,t1,t2}^{start} \\ + \sum_{t1 \in T} y_{f,t1,t2}^{on} \leq T_{t2}^N \quad \forall f \in F, t2 \in T, \end{aligned} \tag{6.18}$$

$$T - \sum_{t} u_{f,t}^{start} \geq \left(T_t^N - T_f^{Crank}\right) \cdot \left(u_{f,t}^{start} - u_{f,t}^{on}\right) \quad \forall f \in F, t \in T, \tag{6.19}$$

$$\begin{aligned} T \cdot \left(u_{f,t2}^{on} - u_{f,t1}^{max}\right) - \sum_{t1 \in T} y_{f,t1,t2}^{on} + \sum_{t1 \in T} y_{f,t1,t2}^{max} \leq \\ \left(T_t^N - T_g^{Crank}\right) \cdot \left(u_{f,t2}^{on} - u_{f,t2}^{max}\right) \quad \forall f \in F, t2 \in T, \end{aligned} \tag{6.20}$$

$$T \cdot \left(u_{f,t}^{on} - u_{f,t}^{max}\right) \leq T - \sum_{t1 \in T} u_{f,t1}^{start} \tag{6.21}$$

$$+T_f^{crank} + T_f^{ramp} \quad \forall f \in F, t \in T,$$

$$T \cdot u_{f,t2}^{max} - \sum_{t1 \in T} y_{f,t1,t2}^{max} \leq \tag{6.22}$$

$$\text{and } \left(T_t^N - T_f^{Crank} - T_f^{Ramp}\right) \cdot u_{f,t2}^{max} \quad \forall f \in F, t2 \in T.$$

Using ancillary variables, the actual power injected into the grid from fuel cells is formulated in Equation (6.23).

$$-p_f^{start} \cdot u_{f,t2}^{start} - u_{f,t2}^{on} + \left(T_f^{ramp} \cdot T_{t2}^N - T_f^{Crank} - p_f^{start}\right) \tag{6.23}$$

$$* \left(u_{f,t2}^{on} - u_{f,t2}^{max}\right) + T_f^{ramp} \cdot T \cdot \left(u_{f,t2}^{max} - u_{f,t2}^{on}\right)$$

$$+T_f^{ramp} \cdot \sum_{t1 \in T} y_{f,t1,t2}^{on} - T_f^{ramp} \cdot \sum_{t1 \in T} y_{f,t1,t2}^{max}$$

$$+\left(p_f^{max} - p_f^{start}\right) \cdot u_{f,t2}^{max} = p_{f,t2} \quad \forall f \in F, t2 \in T.$$

The time durations for different operational stages of the fuel cells are described as follows:

$$u_{f,t}^{start} - u_{f,t+1}^{start} \leq 0 \qquad \forall t \in T, f \in F, \tag{6.24}$$

$$u_{f,t}^{Max} - u_{f,t+1}^{Max} \leq 0 \qquad \forall t \in T, f \in F, \tag{6.25}$$

$$t_f^{Start} = \sum_{t' \in T} (1 - u_{f,t'}^{Start}) \qquad \forall f \in F, \tag{6.26}$$

$$\sum_{t' \in T} (1 - u_{f,t'}^{On}) - t_f^{Start} - t_f^{Crank} \geq 0 \qquad \forall f \in F, \tag{6.27}$$

$$\text{and } \sum_{t' \in T} (1 - u_{f,t'}^{Max}) - t_f^{Start} - t_f^{Ramp} - t_f^{Crank} \geq 0 \qquad \forall f \in F. \tag{6.28}$$

When the transmission infrastructure is deenergized, it can be restored once its connected transmission lines or substations are energized. The energization of the transmission paths is constrained as follows:

$$u_{g,t}^{start} + u_{f,t}^{start} \leq u_{b,t}^{B} \qquad \forall t \in T, b \in B, g \in G_b, f \in F_b, \tag{6.29}$$

$$u_{k,t} - u_{b,t}^{B} \leq 0 \qquad \forall t \in T, g \in G, b \in B_k^F, \tag{6.30}$$

$$u_{k,t} - u_{b,t}^{B} \leq 0 \qquad \forall t \in T, g \in G, b \in B_k^T, \tag{6.31}$$

$$u_{k,t} - u_{k,t+1}^{B} \leq 0 \qquad \forall t \in T, k \in K, \tag{6.32}$$

$$u_{k,t+1} - u_{b1,t}^{B} - u_{b2,t}^{B} \leq 0 \qquad \forall t \in T, k \in K, b1 \in B_k^F, b1 \in B_k^T, \tag{6.33}$$

$$\text{and } u_{b,t}^{B} - \sum_{k \in K(b)} u_{k,t} - \sum_{g \in G(b)} u_{g,t} - \sum_{f \in F(b)} u_{f,t}^{On} \leq 0 \qquad \forall b \in B, t \in T. \tag{6.34}$$

In the event of a complete blackout in the area, we assume that all generators, transmission lines, and substations are deenergized, and can be expressed as follows:

$$u_{g,1}^{start} = 0 \qquad \forall\, g \in G, \tag{6.35}$$

$$u_{f,1}^{start} = 0 \qquad \forall\, f \in F, \tag{6.36}$$

$$u_{b,1}^{B} = 0 \qquad \forall\, b \in B, \tag{6.37}$$

$$\text{and } u_{k,1} = 0 \qquad \forall\, k \in K. \tag{6.38}$$

The black start generators and fuel cells, which can self-start, are described by

$$u_{g,2}^{start} = 1 \qquad \forall\, g \in G^S \tag{6.39}$$

$$\text{and } u_{f,2}^{start} = 1 \qquad \forall\, f \in F. \tag{6.40}$$

6.2.2 Black Start Model Considering Battery as BS Resources

For comparison of the performance of fuel cells as black start resources, a black start model considering battery as BS resources is also proposed. The binary variables $w_{b,t}^S$ and $w_{b,t}^E$ are introduced to indicate the start and end of the discharging status of the battery. These variables are constrained as follows:

$$w_{b,t}^S \geq w_{b,t}^E \qquad \forall\, b \in B^A, t \in T, \tag{6.41}$$

$$w_{b,t}^S \geq w_{b,t-1}^S \qquad \forall\, b \in B^A, t \in T, t \geq 2, \tag{6.42}$$

$$\text{and } w_{b,t}^E \geq w_{b,t-1}^E \qquad \forall\, b \in B^A, t \in T, t \geq 2. \tag{6.43}$$

The time t_b^S at which the battery starts discharging after the blackout can be calculated using the $w_{b,t}^S$, which is described as

$$t_b^S = \sum_t (1 - w_{b,t}^S) \qquad \forall\, b \in B^A. \tag{6.44}$$

The battery starting time is constrained by

$$t_b^S \geq t_b^{Min} \qquad \forall\, b \in B^A. \tag{6.45}$$

The maximum and minimum discharging power of the battery is described by

$$\begin{gathered} \left(w_{b,t}^S - w_{b,t}^E\right) \cdot P_b^{Min} \leq p_{b,t}^{BA} \leq \left(w_{b,t}^S - w_{b,t}^E\right) \cdot P_b^{Max} \\ \forall\, b \in B^A, t \in T. \end{gathered} \tag{6.46}$$

When the battery is discharging, $w_{b,t}^S - w_{b,t}^E$ will be 1, and the discharging power $p_{b,t}^{BA}$ will be constrained by P_b^{Min} and P_b^{Max}. When battery is not discharging, $p_{b,t}^{BA}$ will be 0.

The current battery SOC should be greater than the minimum SOC limits, which is described by

$$SOC_b^S - \sum_t p_{b,t}^{BA} \cdot T^M/60 \geq SOC_b^{Min} \qquad \forall\, b \in B^A. \tag{6.47}$$

In this case, the bus can also be energized when the connected battery is discharging, as described by

$$u_{b,t}^B - \sum_{k \in K(b)} u_{k,t} - \sum_{g \in G(b)} u_{g,t} - \sum_{b \in BA(b)} w_{b,t}^S \leq 0 \qquad \forall b \in B, t \in T. \tag{6.48}$$

Additionally, the black start power is provided by the restored generators and batteries, as described by

$$\sum_{g \in G} p_{g,t} + \sum_{b \in BA} p_{b,t}^{BA} \geq 0 \qquad \forall t \in T. \tag{6.49}$$

6.2.3 GSUS of the Enhanced Black Start Strategy

The proposed black start with fuel cells (BS-FC) and black start with batteries (BS-BT) models are tested, along with the benchmark black start model on the grid without fuel cells and batteries, using the modified IEEE 39-bus system shown in Fig. 6.1 [180]. This test case contains ten generators and are suitable for the study of black start especially for evaluation of the generator start up sequence (GSUS). Generator 1 on bus 30 is the only black start generator in the system.

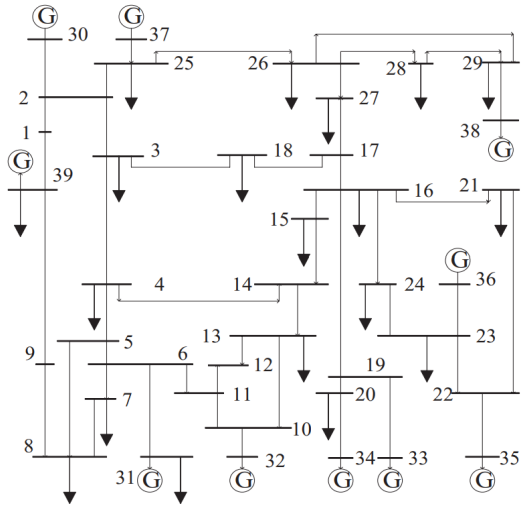

Fig. 6.1. The IEEE 39-bus system architecture [180].

In the simulation, the cranking time of the generators is set to one hour. In the first comparison, two fuel cells or batteries are located on bus 6 and bus 16, which have the highest bus degree importance. Both fuel cells and batteries have 50MW power output capability. The batteries have 50MWh storage with a minimum output of 10% of their maximum output capability. The simulation results are shown in Table 6.1. The systemwide restored power during the black start are plotted in Fig. 6.2. We can observe that BS-FC and BS-BT cases can significantly improve the startup time of the generators. Compared to the case without fuel cells and batteries, the FC and BT cases provide restoration resources at these two locations, aiding in the restoration of the transmission network and providing initial power for generator startup. The FC case performs better than the BT case due to the limitations of battery storage.

Table 6.1 Generator Startup Time for IEEE 39-bus System with Different Black Start Resources

	Without Fuel Cells and Batteries	Fuel Cells (50MW)	Batteries (50MW)
Generator 2	140 min	40 min	40 min
Generator 3	220 min	120 min	120 min

Table 6.1 Continued.

Generator 4	160 min	60 min	60 min
Generator 5	240 min	140 min	160 min
Generator 6	180 min	80 min	80 min
Generator 7	200 min	100 min	100 min
Generator 8	80 min	140 min	140 min
Generator 9	220 min	120 min	120 min
Generator 10	200 min	100 min	100 min
System Average	182.2 min	100 min	102.2 min

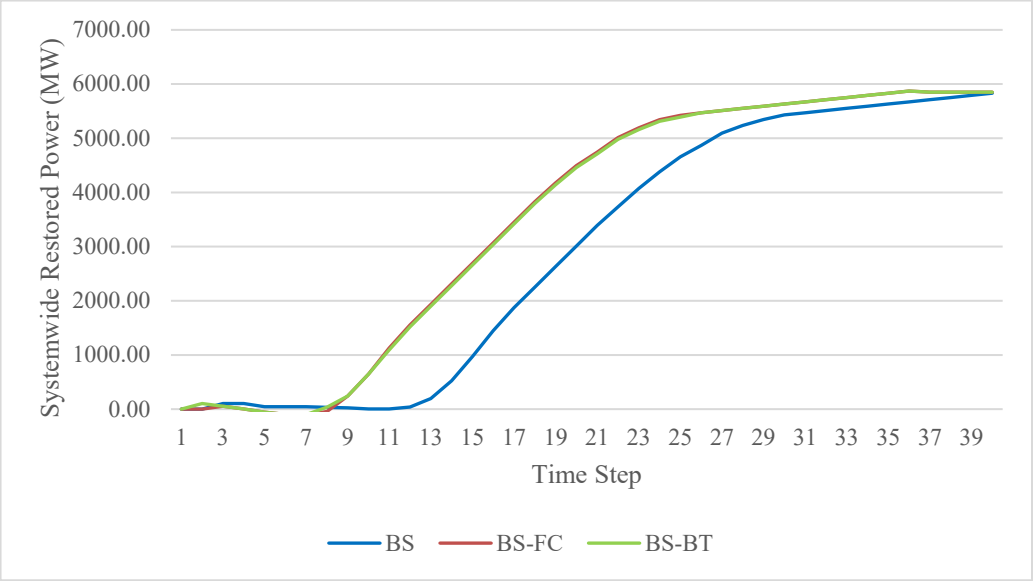

Fig. 6.2. Systemwide restored power of IEEE 39-bus system during the black start.

We also investigate how the capacity of fuel cells influences restoration performance. Since fuel cells can obtain hydrogen from pipelines, they do not face storage limits like batteries. As shown in Table 6.2, when the output capacity is reduced, some generators experience startup delays. However, not all generators are delayed; some may start earlier. This is because the strategy optimizes the overall

system generation. The systemwide restored power for the black start with different fuel cell capacities is plotted in Fig. 6.3.

Table 6.2 Generator Start-up Time (min) for IEEE 39-bus System with Different Fuel Cells Generation Capacity

Fuel Cell Capacity (MW)	100	50	40	30	20	15	10	5
Generator 3	80	120	80	120	120	140	120	120
Generator 5	140	140	140	140	160	160	160	160
Generator 6	80	80	120	80	100	100	100	140
Generator 7	80	100	140	140	140	100	100	140
Generator 8	120	140	140	140	140	140	160	160
System Average	91.1	100	104.4	104.4	108.8	108.8	111.1	115.5

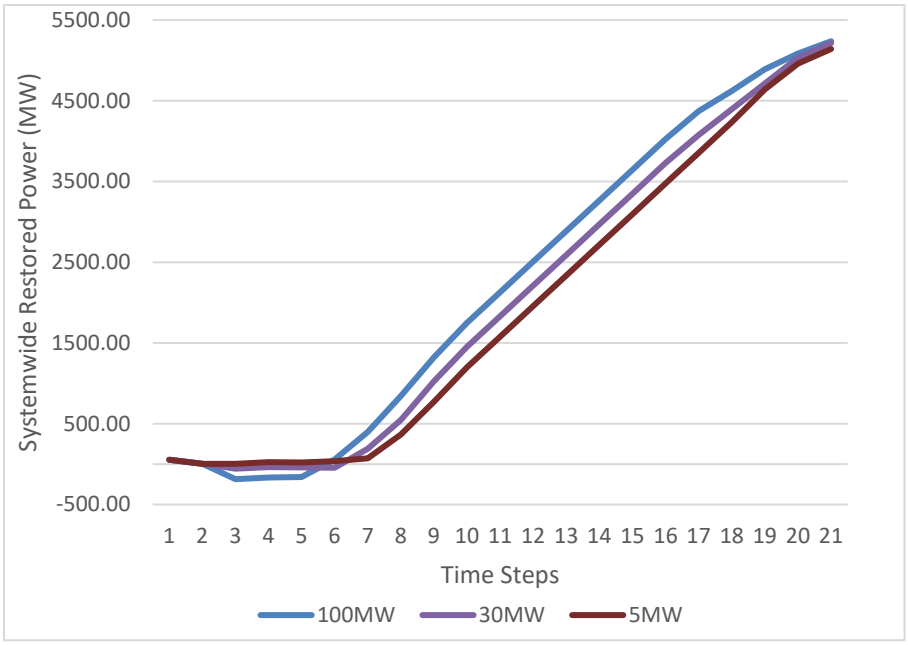

Fig. 6.3. Systemwide restored power of IEEE 39-bus system with different fuel cell capacities.

We further investigate how the size of batteries influences restoration performance. We assume the minimum output is 10% of the maximum output

capacity for batteries, and the batteries are initially charged to release energy at maximum output power for one hour. The numerical results are shown in Table 6.3.

Table 6.3 Generator Start-up Time (min) for IEEE 39-bus System with Different Battery Discharge Capacity

Discharge Capacity (MW)	120	100	80	50	30	20	10	5
Generator 3	100	80	120	120	140	120	120	120
Generator 5	120	140	140	160	140	160	160	160
Generator 6	80	80	80	80	80	100	100	140
Generator 7	80	80	80	100	120	140	100	140
Generator 8	80	120	100	140	120	140	160	160
Generator 9	120	120	120	120	140	120	120	120
Generator 10	100	100	100	100	100	100	140	100
System Average	86.6	91.1	93.3	102.2	106.6	108.8	111.1	115.5

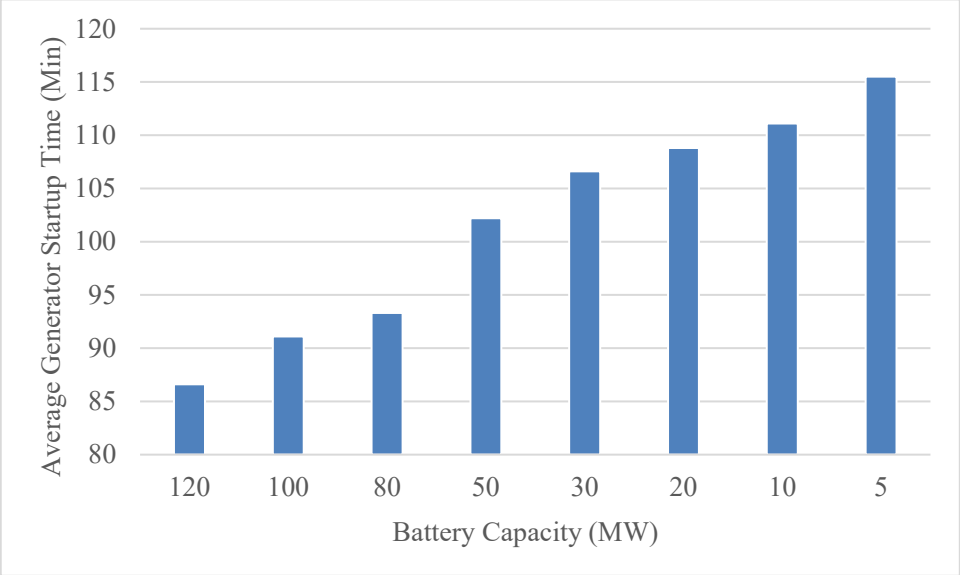

Fig. 6.4. Average generator startup time for IEEE 39-bus system with different battery capacities.

Comparing fuel cells and battery storage, their output capacity or size similarly influences restoration performance. However, due to storage limitations, batteries may have different GSUS.

When a blackout occurs, the battery may not be fully charged. We investigated the influence of the initial state of charge (SOC) on restoration performance. Assuming a maximum storage capacity allowing a two-hour release at maximum output power, with a maximum power output of 30 MW, we observed that when SOC is greater than 70%, the black start maintains high performance. However, when SOC is low at the time of the black start, performance is significantly impacted. The numerical results are shown in Table 6.4.

Table 6.4 Generator Start-up Time (min) for IEEE 39-bus System with Different Battery SOC

Battery SOC	≥70%	50%	30%	10%
Generator 3	120	140	140	120
Generator 5	140	140	160	160
Generator 6	80	80	100	140
Generator 7	140	120	120	140
Generator 8	140	120	120	160
Generator 9	120	140	160	120
System Average	104.4	104.4	111.1	115.5

We also investigated the selection of locations for fuel cells and batteries. In the first selection, the fuel cells and batteries are located on buses with the highest bus importance degree, as used in the simulations above. For the second selection, they are located on buses closer to the generators, within three transmission lines of distance. In this test case, bus 11 and bus 19 are selected. With a fuel cell and battery output capacity of 30 MW, the results are shown in Table 6.5. Based on the results, we can

observe that different locations for fuel cells or batteries can significantly impact the generator start-up sequence.

Table 6.5 Generator Start-up Time (min) for IEEE 39-bus System with Different BS Resources Locations

Configuration	FC		BT	
	Selection 1	Selection 2	Selection 1	Selection 2
Generator 3	120	140	140	140
Generator 4	60	40	60	40
Generator 5	140	160	140	160
Generator 6	80	140	80	140
Generator 7	140	140	120	140
Generator 8	140	80	120	80
Generator 9	120	120	140	120
Generator 10	100	120	100	120
System Average	104.4	111.1	104.4	111.1

The black start simulation is also conducted on our created Texas test system TX-123BT, to validate the scalability of the proposed black start model. The statistical data for utilizing fuel cells in the black start process for TX-123BT is presented in Table 6.6. Notably, only 75 out of the 255 total branches are required to restore large-scale thermal power plants.

Table 6.6 Statistical Data for Black Start on TX-123BT

Total Number of Large-Scale Thermal Power Plants	138
Average Time Steps that Generator Start Ramping Up	5.63
Total Restored Power (MW)	69,152
Total Number of Branches	255
Total Number of Buses	123
Total Number of Critical Branch in BS	75
Total Number of Critical Bus in BS	82

We also conducted the black start on TX-123BT without the installation of fuel cells. Fig. 6.5 compares the system-wide restored power during the black start for

scenarios with and without fuel cells. We observe that fuel cells significantly facilitate the black start process. Fig. 6.6 shows the number of generators ramping up during the black start.

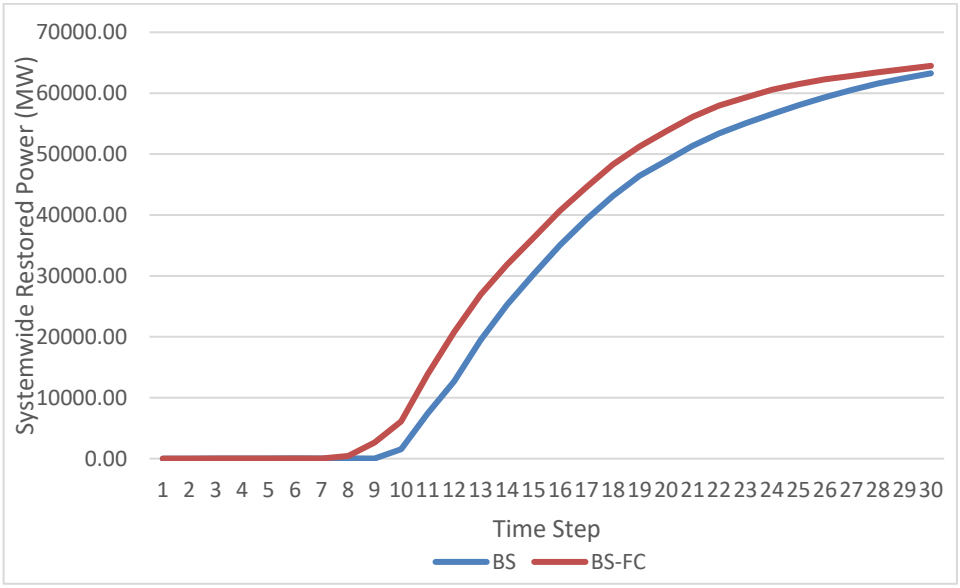

Fig. 6.5. Systemwide restored power during the black start on TX-123BT.

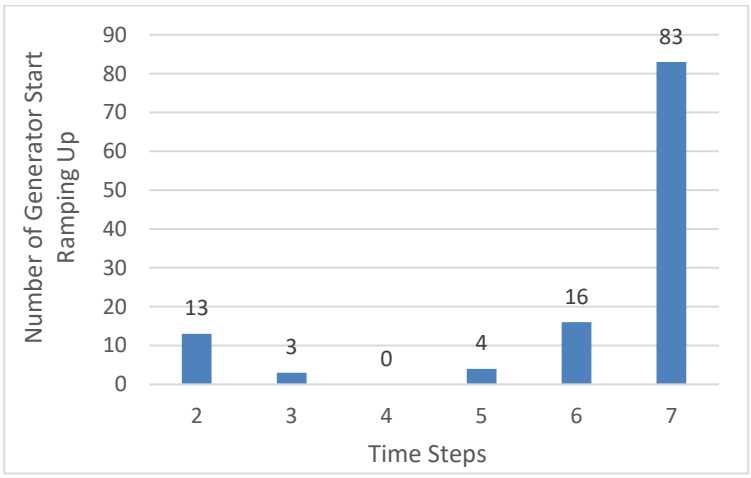

Fig. 6.6. The number of generators that start ramping up in TX-123BT.

The critical transmission network for black start comprises seven separate areas, with only a portion of the entire network needing restoration. Therefore,

network reconfiguration is necessary to identify and reestablish a large and efficient network to support subsequent large-scale load pickup.

6.3 Optimal Skeleton Network Reconfiguration

The network reconfiguration stage aims to reconstruct an efficient and reliable skeleton network, which forms the basis for large-scale load restoration. During the black start stage, some buses and branches are restored to deliver cranking power to non-black start (NBS) generators. These critical buses and branches are necessary for restoration and should be included in the target skeleton network. In other words, the restoration strategy for the skeleton network should take the black start solution as an input to determine the target skeleton network. After the skeleton network and the corresponding restoration sequence are determined, load pickup actions should be taken to eliminate voltage violation problems during the energization of the skeleton network. A general five-step restoration strategy is introduced to demonstrate the decision procedures for network reconfiguration.

6.3.1 Five-step Restoration Strategy

In general, the restoration strategy of network reconfiguration can be divided into five steps. Each step can be considered as a tractable problem. The five-step restoration strategy is described below: (a) find the optimal generator start up sequence and critical transmission paths to crank the generators; (b) determine a well-performed skeleton network; (c) identify the restoration sequence of the skeleton network found by step b; (d) determine the load pickup during the restoration to

eliminate the voltage violation; (e) check whether all safety constraints are satisfied; if the current restoration solution fails the check, it will go back to step a and specific constraints will be added based on the violations. The general skeleton-network restoration strategy is illustrated in Fig. 6.7 (a).

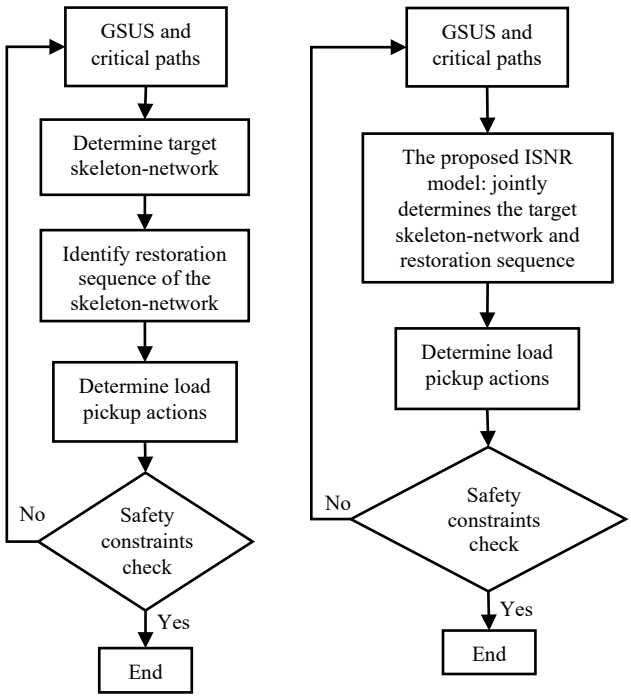

Fig. 6.7. Structure of traditional reconfiguration strategy and ISNR strategy.

6.3.2 The ISNR Model-Based Restoration Strategy

The proposed integrated skeleton network restoration (ISNR) model can simultaneously determine the skeleton-network and the corresponding restoration sequence. The critical branches and buses identified in the black-start stage will be the input data of the proposed ISNR model. Besides, the restoration sequence determined by the proposed ISNR model can be used and modified in the load pickup step. This

indicates the proposed ISNR model can realize the functions of both step b and step c. The skeleton-network and the restoration sequence are co-optimized to achieve an efficient and fast recoverable skeleton-network restoration solution. The restoration strategy with the proposed ISNR model is illustrated in Fig. 6.7 (b).

6.3.3 Formulation of ISNR Model

A. Skeleton-Network Formulation:

To achieve a well-performed skeleton-network that can be restored in the least time, both the skeleton-network quality and the restoration time should be considered in the model. A topology characteristics-based skeleton-network quality index (TCSNQI) is proposed to evaluate the quality of the network at each time step. The network which achieves a quality index larger than a specific value will be regarded as a qualified skeleton-network. A qualified skeleton-network should be restored as soon as possible. Thus, the objective function is to minimize the total time that a skeleton-network does not satisfy the skeleton quality requirement. It is described by

$$\min \quad \sum_{t \in T} (1 - u_t^S), \tag{6.50}$$

where u_t^S is the binary indicator of the skeleton-network quality. When u_t^S is 1, the restored network at time t satisfies the quality requirement; otherwise, the restored network fails to meet the requirement at time t.

The skeleton-network will keep the qualified status after it meets the quality requirement, and it is described by

$$u_{t-1}^{S} \leq u_{t}^{S}, \qquad \forall t \in T. \tag{6.51}$$

The indicator of quality status change v_t^S can be 1 only when the skeleton-network meets the quality requirement at time *t*. It can be expressed as

$$v_{t}^{S} = u_{t}^{S} - u_{t-1}^{S}, \qquad \forall t \in T. \tag{6.52}$$

The TCSNQI proposed to evaluate the quality of the network at each time step is defined as follows:

$$\eta_{t}^{S} = \beta \sum_{i \epsilon B} \alpha_i \, u_{i,t} + \gamma d_t, \qquad \forall t \in T, \tag{6.53}$$

$$\alpha_i = \frac{1}{n_i \cdot l_i}, \tag{6.54}$$

$$l_i = \frac{\sum_{i,j \in V_i} d_{min,ij}}{n_i(n_i - 1)/2}, \tag{6.55}$$

$$\text{and } d_t = d_{t-1} + \sum_{i \epsilon B} \sum_{j \epsilon B, j \neq i} d_{ij} v_{i,t} u_{j,t-1} + \sum_{i \epsilon B} \sum_{j \epsilon B, j \neq i} d_{ij} v_{i,t} v_{j,t}/2 \,, \tag{6.56}$$

$$\forall t \in T.$$

In Equation (6.53), the proposed TCSNQI is the sum of a weighted network importance term and a weighted network distance term. The network importance term is the total bus importance degree of the buses restored by time t, where α_i denotes the bus importance degree of bus i, and $u_{i,t}$ represents the binary variable of restoration status for bus i at time t. The bus importance degree proposed in [175] is defined by Equation (6.54) and Equation (6.55). The network distance term is defined by Equation (6.56). The network distance is the total distance between the restored buses at time t. A larger network distance means the restored skeleton-network can cover a

larger area. The distance between the buses is calculated for the fully restored power system, thus the skeleton-network can cover a large area from the perspective of the entire system. The network distance is the sum of the previous network distance and the distance caused by newly restored buses at time *t*. The total distance between the newly restored buses and previously restored buses is calculated by the second term in Equation (6.56). The total distance between the newly restored buses is calculated by the third term in Equation (6.56). $d_{i,j}$ denotes the distance between bus i and bus j, which is the total number of branches in the shortest path between the two buses.

When the skeleton-network meets the quality requirement at time t, the proposed TCSNQI should be larger than a prespecified number N. It can be described by

$$\eta_t^S \geq N \cdot v_t^S , \qquad \forall t \in T. \tag{6.57}$$

B. Transmission Path Energization Constraints:

The transmission path energization constraints can be expressed as follows:

$$u_{L_{ij},t} \leq u_{i,t} , \ \forall L_{ij} \in L, \forall t \in T, \tag{6.58}$$

$$u_{L_{ij},t} \leq u_{j,t} , \qquad \forall L_{ij} \in L, \forall t \in T, \tag{6.59}$$

$$u_{L_{ij},t+1} \leq u_{i,t} + u_{j,t} , \qquad \forall L_{ij} \in L, \forall t \in T, \tag{6.60}$$

$$u_{i,t} \leq \sum_{L_{ij} \in L_i^N} u_{L_{ij},t} , \qquad \forall i \epsilon B^{NC}, \forall t \in T, \tag{6.61}$$

$$u_{L_{ij},t} \leq u_{L_{ij},t+1}, \ \forall L_{ij} \in L, \forall t \in T, \tag{6.62}$$

$$v_{i,t} = u_{i,t} - u_{i,t-1} , \qquad \forall i \epsilon B, \forall t \in T, \tag{6.63}$$

$$u_{L_{ij},t} = u^{C}_{L_{ij},t}\ ,\ \forall L_{ij} \in L^{C}, \forall t \in T, \tag{6.64}$$

$$\text{and } u_{i,t} = u^{C}_{i,t}, \qquad \forall i \epsilon B^{C}, \forall t \in T, \tag{6.65}$$

If a branch is energized, its terminal buses can be energized by Constraints (6.58)-(6.59). In Constraint (6.60), a branch can be energized at the next time step if at least one of the terminal buses is energized. Constraint (6.61) indicates a bus can be energized when at least one of its connected branches is restored. Constraint (6.62) ensures the branch will remain energized after it is restored. Equation (6.64) and (6.65) guarantee the energization of critical branches and buses identified in the black start stage. $u^{C}_{L_{ij},t}$ and $u^{C}_{i,t}$ are the energization indicators of the critical branches and buses at time t in the black-start stage respectively.

C. Linearization:

The product terms between two binary variables in Equation (6.56) will lead to non-linearity. To address this issue, two ancillary variables $y^{1}_{i,j,t}$ and $y^{2}_{i,j,t}$ that are introduced to linearize Equation (6.56). The variables are defined by

$$\begin{cases} y^{1}_{i,j,t} = u_{i,t} \cdot u_{j,t}, & \forall t \in T, \\ y^{2}_{i,j,t} = u_{i,t-1} \cdot u_{j,t}, & \forall t \in T. \end{cases} \tag{6.66}$$

Equation (6.52) is substituted into Equation (6.56) to obtain the equation as follows:

$$\begin{aligned} d_t = d_{t-1} + \sum_{i \epsilon B} \sum_{j \epsilon B, j \neq i} d_{i,j}\left(u_{i,t} \cdot u_{j,t} - u_{i,t-1} \cdot u_{j,t}\right) \\ + \sum_{i \epsilon B} \sum_{j \epsilon B, j \neq i} d_{i,j}(u_{i,t} \cdot u_{j,t} - u_{i,t-1} \cdot u_{j,t} - u_{i,t} \cdot u_{j,t-1} + u_{i,t-1} \cdot u_{j,t-1})/2 \end{aligned} \tag{6.67}$$

$$\forall t \in T.$$

Then, Equation (6.66) is substituted into Equation (6.67) to obtain the linearized expression shown as

$$d_t = d_{t-1} + \sum_{i \epsilon B} \sum_{j \epsilon B, j \neq i} d_{i,j}\left(1.5y^1_{i,j,t} - 1.5y^2_{i,j,t} - 0.5y^2_{j,i,t} + 0.5y^1_{i,j,t-1}\right) \quad (6.68)$$
$$\forall t \in T.$$

Since the definition of ancillary variables $y^1_{i,j,t}$ and $y^2_{i,j,t}$ still involves non-linearity, a set of linear inequations will be used to replace (6.66) in the proposed ISNR model, which are described as follows:

$$\begin{cases} y^1_{i,j,t} \geq u_{i,t} + u_{j,t} - 1, & \forall t \in T, \\ y^1_{i,j,t} \leq u_{i,t}, & \forall t \in T, \\ y^1_{i,j,t} \leq u_{j,t}, \forall t \in T, \end{cases} \quad (6.69)$$

$$\begin{cases} y^2_{i,j,t} \geq u_{i,t-1} + u_{j,t} - 1, \ \forall t \in T, \\ y^2_{i,j,t} \leq u_{i,t-1}, \ \forall t \in T, \\ y^2_{i,j,t} \leq u_{j,t}, \ \forall t \in T. \end{cases} \quad (6.70)$$

To summarize, the proposed ISNR model consists of Equations (6.50) – (6.55), (6.57) – (6.65), (6.68) – (6.70).

6.3.4 Case Studies

The proposed ISNR model is tested using the New England 39-bus system (also called IEEE 39-bus system). The time interval is 5 minutes. The weight coefficient β is set to 150, and γ is set to 0.7. The least requirement N for skeleton-network quality index is set to 1,500. The test case is solved using solver Gurobi in

Python. The simulation is performed on a desktop computer with Intel-i7 3.2 GHz CPU and 16 GB RAM.

The skeleton-network meets the network quality requirement at 35 minutes according to the optimal objective value. A quality requirement which is easier to achieve is applied, since the restoration can be delayed due to the safety constraints and other reasons. It can be noticed that some critical buses and branches are not restored when the network is qualified. The skeleton-network determined by the proposed ISNR model includes 32 skeleton buses and 31 skeleton branches. The optimal skeleton buses are listed in Table 6.7. It can be noticed that bus 9 is added to the skeleton-network besides the critical buses found by the black start model.

Table 6.7 Buses in Skeleton Network of IEEE 39-bus System

Bus Number	Bus Start Time (Minute)	Bus Importance Degree	Bus Number	Bus Start Time (Minute)	Bus Importance Degree
1	25	0.812	22	50	0.845
2	20	0.903	23	50	0.845
3	25	0.907	24	45	0.823
4	30	0.916	25	25	0.861
5	35	0.883	26	30	0.894
6	40	0.883	29	35	0.840
9	35	0.812	30	15	0.770
10	45	0.845	31	45	0.776
13	40	0.851	32	50	0.778
14	35	0.911	33	50	0.773
16	40	1	34	65	0.781
17	35	0.904	35	55	0.780
18	30	0.846	36	55	0.780
19	45	0.839	37	30	0.773
20	60	0.809	38	40	0.781
21	45	0.823	39	30	0.812

The skeleton branches determined by the proposed ISNR model are shown in Table 6.8. Branch 9-39 is restored at t=35 minutes besides the critical branches. Bus 9 can be energized due to the energization of branch 9-39. It lays the foundation for restoring load bus 8 and load bus 7.

Table 6.8 Branches in Skeleton Network of IEEE 39-bus System

Branch (from bus – to bus)	Start Time (Minute)	Branch (from bus – to bus)	Start Time (Minute)	Branch (from bus – to bus)	Start Time (Minute)
1-2	25	10-32	50	23-36	55
1-39	30	13-14	40	25-26	30
2-3	25	16-17	40	25-37	30
2-25	25	16-19	45	26-29	35
2-30	20	16-21	45	29-38	40
3-4	30	16-24	45		
3-18	30	17-18	35		
4-5	35	19-20	60		
4-14	35	19-33	50		
5-6	40	20-34	65		
6-31	45	21-22	50		
9-39	35	22-35	55		
10-13	45	23-24	50		

The simulation results are compared with the TLR model used in [179]. The method in [176] found a skeleton network with 32 skeleton buses and 32 skeleton branches. Although the two skeleton-networks have the same number of skeleton buses, they do not share the same skeleton buses. The TLR model selects bus 11 as the skeleton bus instead of bus 9 that is selected by the proposed ISNR model. The total

bus importance degree of skeleton-network is 26.8 for the proposed ISNR model which is the same with the TLR model. Fig. 6.8-6.10 shows the plots of network importance, network distance and network quality index vs. time respectively. The proposed ISNR model has larger values for three indexes in the restoration period from 35 minutes to 50 minutes, which demonstrates the proposed ISNR model outperforms the traditional TLR model. This is because the proposed ISNR model integrates the transmission path and topology characteristics that would lead to a more efficient and faster recoverable skeleton network.

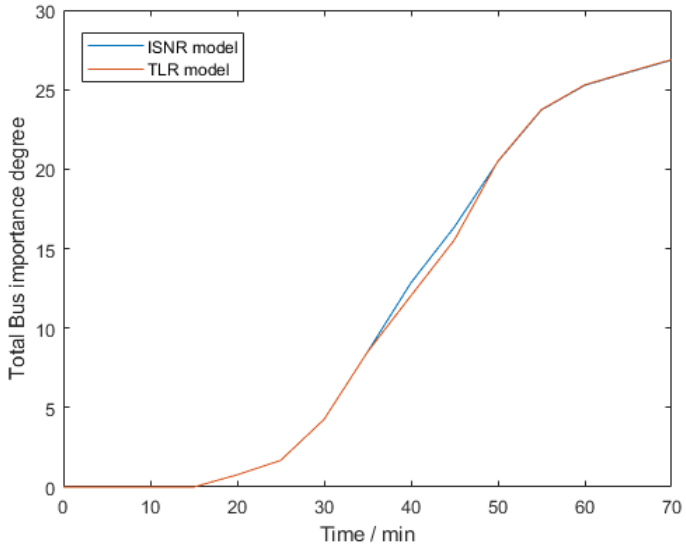

Fig. 6.8. Comparison of total bus importance degree between the proposed ISNR and the traditional TLR models.

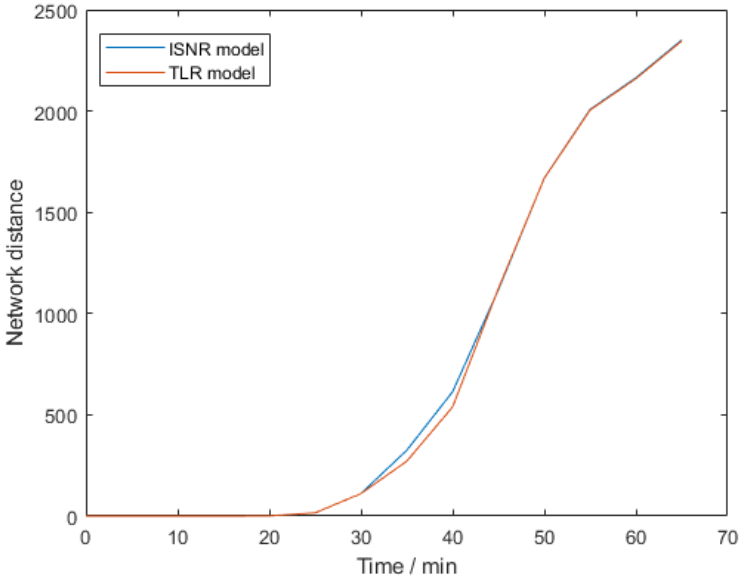

Fig. 6.9. Comparison of the network distance between the proposed ISNR and the traditional TLR models.

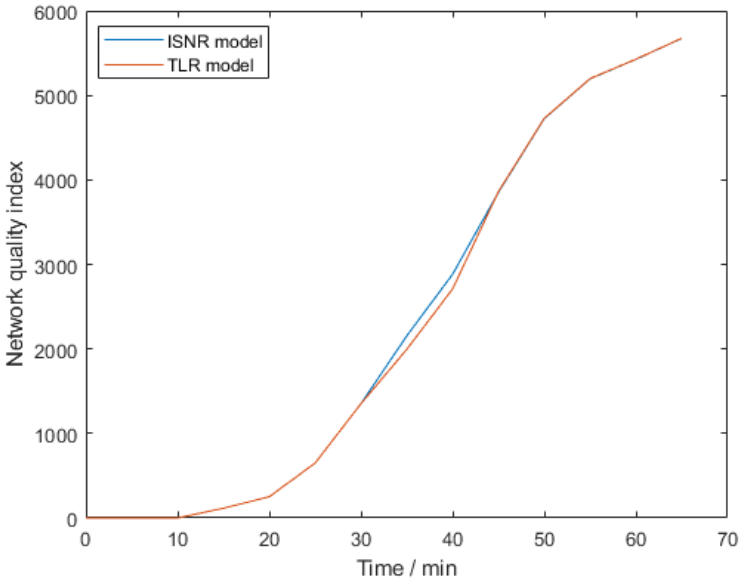

Fig. 6.10. Comparison of the network quality index between the proposed ISNR and the traditional TLR models.

In conclusion, a new skeleton-network reconfiguration model, namely the ISNR model is proposed. The proposed ISNR model aims to obtain a well-performed and fast recoverable skeleton-network as well as the associated restoration sequence of it. The proposed TCSNQI is used to evaluate the quality of the network considering both the bus importance and the total distance between the buses in the network. The proposed ISNR model will determine a target network that has the least restoration time while meeting the specified quality index requirement. The simulation results on the New England 39-bus system demonstrate the proposed method can obtain an efficient skeleton-network during the restoration process.

6.4 Restoration Performance Evaluation

To further study the restoration performance of grids integrated with fuel cells and batteries in the periods following the black start, we conduct network reconfiguration simulations on the IEEE 39-bus system integrated with fuel cells or batteries. According to the proposed network reconfiguration model in Chapter 6.3, the generator startup sequence and the necessary transmission paths for restoring the generators are input into the model to obtain the recovery timeline of the backbone transmission network.

We investigated and compared the network reconfiguration performance of grids integrated with fuel cells and batteries with the benchmark case. As shown in Fig. 6.11, utilizing fuel cells and batteries not only enhances black start performance but also significantly increases the capability to restore the transmission network in a shorter time. The backbone transmission network can be restored by the 8th time step

with the help of fuel cells and batteries, whereas the benchmark case requires 14 time steps to energize the backbone transmission network.

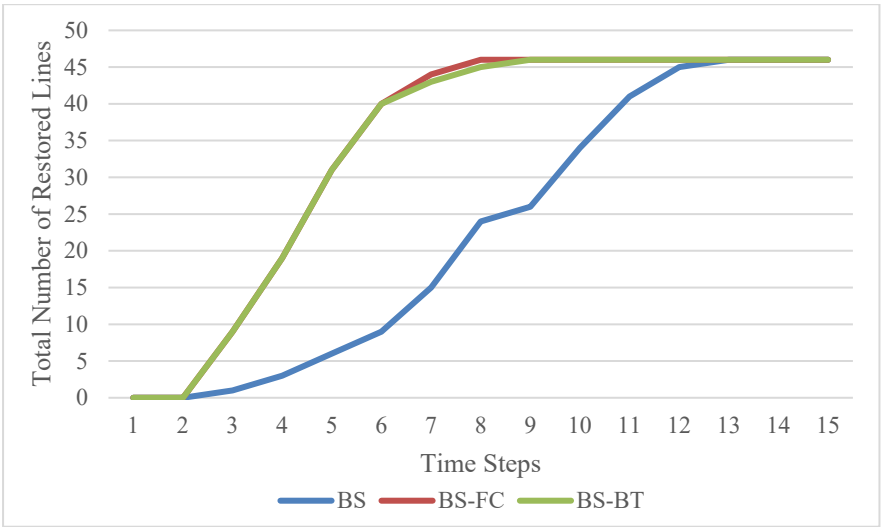

Fig. 6.11. Total number of restored lines for IEEE 39-bus system with different BS resources.

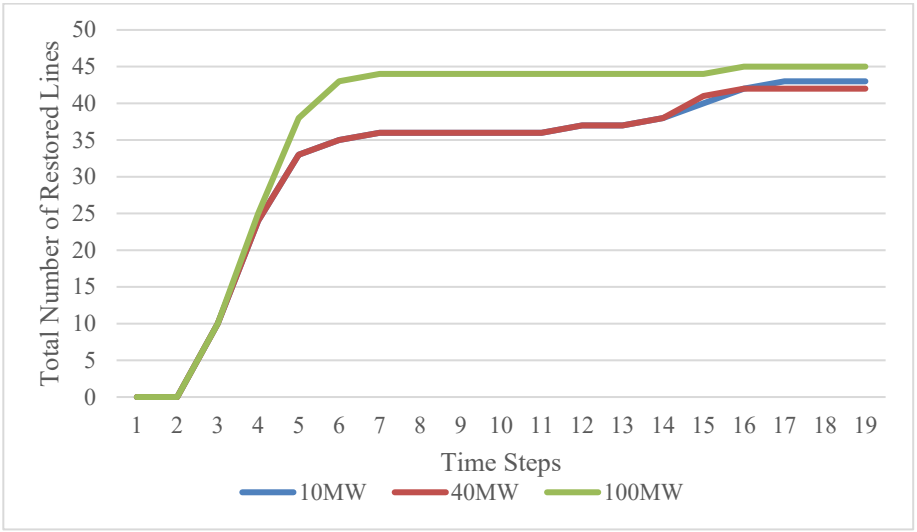

Fig. 6.12. Total number of restored lines for IEEE 39-bus system with different fuel cell capacities.

Fuel cell capacity significantly influences black start performance. During the network reconfiguration stage, fuel cells with larger capacities also provide much better network restoration performance compared to those with smaller capacities.

During the black start, the performance of grids with fuel cells and batteries can differ even when their output capacities are the same. In the subsequent network reconfiguration simulation, the performance of fuel cells and batteries with the same capacity is compared and plotted in Fig. 6.13. We observe that both fuel cell and battery cases can restore the backbone network much more quickly, with the fuel cell case being slightly faster than the battery case.

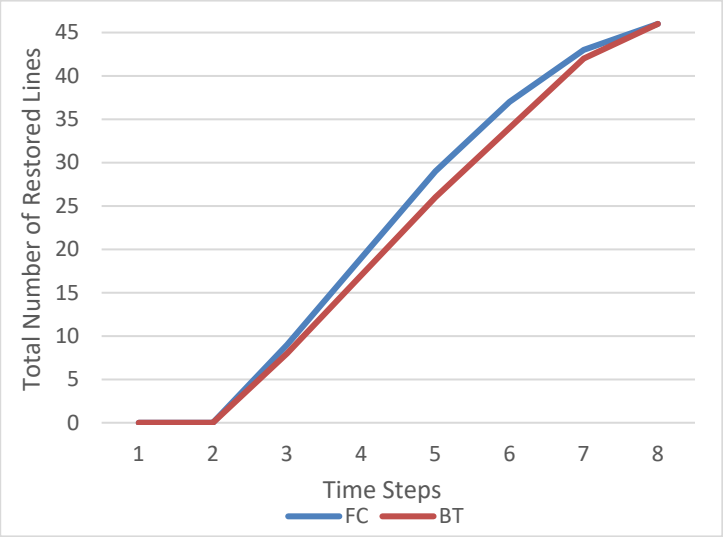

Fig. 6.13. Total number of restored lines for IEEE 39-bus system with fuel cells and batteries.

The network reconfiguration simulation is also conducted on the TX-123BT test case, which covers a large geographic area in Texas. The simulation can verify the performance of network reconfiguration over a large area. The total number of restored skeleton lines during the network reconfiguration process is shown in Fig. 6.14. We observe that our proposed network configuration model can reestablish a skeleton network which includes a sufficient number of lines to form a large and robust transmission system. By utilizing fuel cells, substations at more locations can be restored sooner, allowing for the earlier restoration of additional transmission lines

during network reconfiguration. Fig. 6.15 illustrates the skeleton network distance during the reconfiguration. As more skeleton lines are restored during the reconfiguration, the network distance increases rapidly. The total distance of the restored network is 36,513, indicating that the restored network is widely distributed across various areas. The TX-123BT with fuel cells enables a more distributed restoration of the network compared to scenarios without fuel cells.

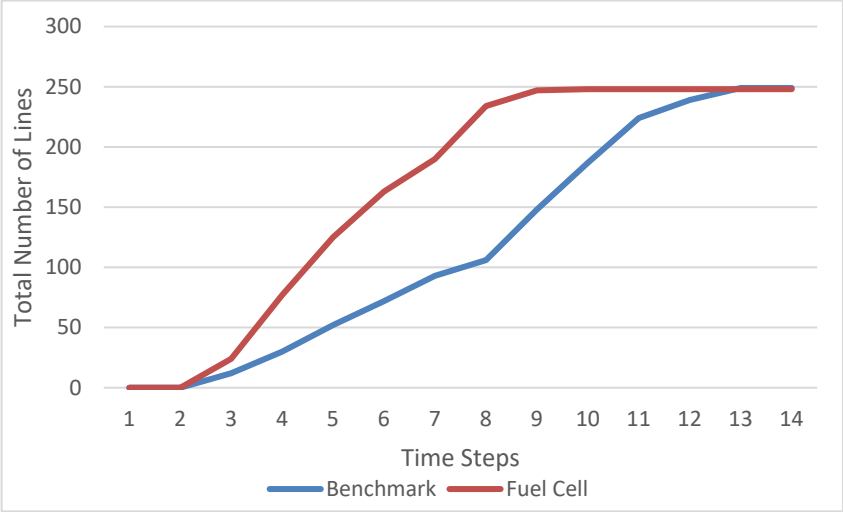

Fig. 6.14. Total number of restored skeleton lines for TX-123BT.

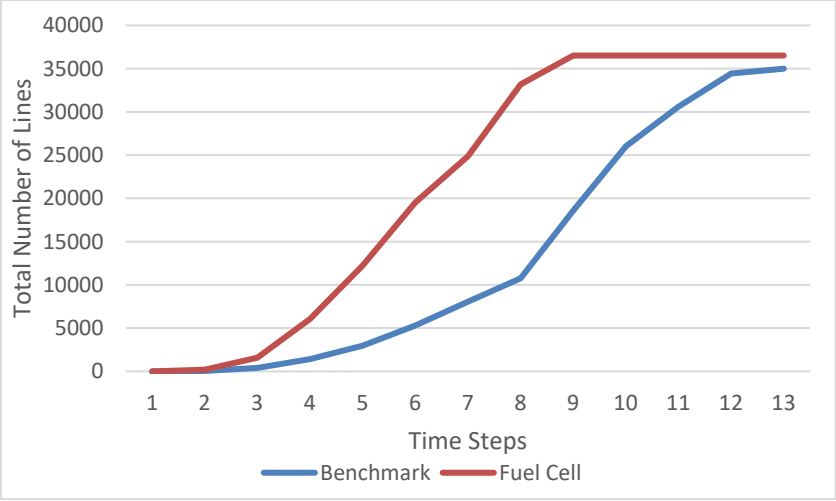

Fig. 6.15. Total skeleton network distance of TX-123BT during the reconfiguration.

6.5 Summary

This chapter discusses enhancing power system restoration using fuel cells as black start resources. We proposed black start models incorporating fuel cells and battery storage, focusing on their unique characteristics. Simulations on the IEEE 39-bus system compare GSUS for systems equipped with fuel cells versus batteries, with sensitivity analyses on fuel cell capacity, battery storage capacity, and initial state of charge (SOC) determining optimal black start scenarios. The model aims to restore all generation capabilities swiftly, prioritizing critical loads, with binary variables representing different generation statuses of fuel cells and ancillary variables linearizing the model. This model includes constraints for energizing transmission paths, ensuring restored generation resources meet cranking power requirements. It also compares the performance of fuel cells and batteries, with binary variables indicating battery discharging status and constraints ensuring adequate power output and SOC. The proposed ISNR model optimizes both network quality and restoration time in the network reconfiguration stage. Simulation results on the New England 39-bus system demonstrate the model's effectiveness, outperforming traditional models by achieving faster and more efficient network restoration. Numerical results show that integrating fuel cells and batteries can enhance both black start and network reconfiguration performance. Fuel cells with larger capacities offer better performance, and both fuel cell and battery cases restore the backbone network more quickly than the benchmark case.

7. CONCLUSION AND FUTURE WORK

This dissertation has thoroughly examined the integration and joint operation of hydrogen-related facilities, such as fuel cells and electrolyzers, within power systems to enhance economic efficiency and system reliability. By addressing both operational and planning aspects, this research has laid the groundwork for incorporating hydrogen technologies into renewable power grids. The motivation behind this work stems from the growing need to integrate renewable energy sources, which are often variable and unpredictable, posing significant challenges to grid reliability. Through comprehensive modeling and optimization strategies, this dissertation has provided valuable insights into the potential of hydrogen as a key component in future energy systems. The results demonstrate that hydrogen-based solutions can significantly reduce operational costs, improve system reliability, and support the transition to cleaner and more sustainable energy sources.

7.1 Contributions

Throughout this dissertation, several key contributions have been made to the field of hydrogen energy systems in power grids. The daily operation model for Hydrogen Energy Transmission and Conversion Systems (HETCS) in Chapter 2 has been a pivotal advancement. This model optimizes the conversion, storage, and transmission of hydrogen, integrating it seamlessly with existing power systems. The proposed models for HETCS have shown that hydrogen can effectively mitigate the intermittency of renewable energy sources, reducing operational costs and enhancing grid reliability.

In Chapter 3, the annual scheduling model (ASM) for hydrogen storage is another significant contribution. By addressing both intra-day and cross-seasonal energy exchanges, the ASM ensures a balanced and efficient operation of hydrogen storage systems throughout the year. Detailed case studies have demonstrated the ASM's effectiveness in reducing renewable energy curtailment and operational costs. This model provides a robust framework for integrating hydrogen storage into renewable power grids, enabling better management of energy resources in longer time periods.

The creation of comprehensive power system test case TX-123BT in Chapter 4, considers factors such as climate impacts, renewable production, and dynamic line ratings, has provided a valuable tool for simulation-based studies. It allows for a detailed analysis of the performance and reliability of power systems under various future scenarios, offering insights into the potential challenges and benefits of integrating hydrogen technologies.

The Transmission Expansion Planning with Hydrogen (TEP-H) model introduced in Chapter 5 represents a novel approach to hybrid transmission network planning. By incorporating both electric and hydrogen transmission systems, this model optimizes investments and operational strategies, demonstrating the economic and operational benefits of hydrogen transmission in renewable-dominated grids. This approach highlights the potential for hydrogen to play a critical role in future energy transmission infrastructure.

The exploration of fuel cells as black start resources for power system restoration in Chapter 6 has provided new strategies for enhancing grid resilience. The proposed five-step restoration strategy and the ISNR model offer optimized solutions for network reconfiguration and restoration sequences, leveraging the unique capabilities of fuel cells to support rapid and reliable system recovery. Another significant contribution is the introduction of a black start model that considers fuel cells as black start resources. This model addresses the critical need for rapid system restoration following a blackout by leveraging the unique characteristics of fuel cells. The proposed model includes detailed constraints and optimization techniques to ensure that fuel cells can provide the necessary power for black start operations, thereby enhancing the resilience of the power system. The comprehensive analysis and case studies presented in this dissertation demonstrate the effectiveness of the proposed black start model in improving system recovery times.

7.2 Future Work

The research presented in this dissertation opens several avenues for future exploration. Further investigation and detailed modeling of advanced hydrogen production, storage, and utilization technologies into the proposed operation and planning models are essential to improve efficiency and reduce costs for hydrogen-integrated power systems. This includes developing more sophisticated models that can accurately represent the physical and economic characteristics of new hydrogen technologies, such as high-efficiency electrolyzers and advanced hydrogen storage. Incorporating these technologies into power system models will enable more precise

assessments of their benefits and trade-offs, thereby enhancing decision-making processes.

The integration of hydrogen energy systems with other emerging technologies, such as advanced battery storage, offers promising prospects. For example, electrolyzers require a steady power input for safe operation, and combining hydrogen facilities with batteries can significantly enhance this capability. Future research should focus on developing optimal planning and operation strategies that leverage the complementary strengths of hydrogen and battery systems. This includes investigating the best ways to integrate these technologies into existing power grids, designing hybrid systems that maximize efficiency and reliability, and evaluating the economic impacts of such integrations.

The created TX-123BT test case, which includes spatio-temporal correlated profiles for long time periods, provides a valuable platform for further research. This test case enables the application of advanced machine learning and artificial intelligence techniques that can improve the accuracy and efficiency of energy system simulations and operations. Machine learning can be used to develop predictive models such can anticipate demand fluctuations and optimize the operation of hydrogen-integrated power systems in real-time. This includes developing algorithms that can quickly process large amounts of data and make real-time decisions to balance supply and demand, minimize costs, and ensure system stability.

7.3 List of Publications

(1) Jin Lu and Xingpeng Li, “Transmission Planning for Climate-impacted Renewable Energy-Dominated Power Grids: Data Preparation, Model Improvement, and Evaluation”, *Journal of Modern Power Systems and Clean Energy* (accepted).

(2) Jin Lu and Xingpeng Li, “Annual Benefit Analysis of Integrating the Seasonal Hydrogen Storage into the Renewable Power Grids”, *IEEE PES General Meeting*, Orlando, Florida, USA, Jul. 2023.

(3) Jin Lu and Xingpeng Li, “The Benefits of Hydrogen Energy Transmission and Conversion Systems to the Renewable Power Grids: Day-ahead Unit Commitment”, *54th North American Power Symposium*, Salt Lake City, UT, USA, Oct. 2022.

(4) Jin Lu and Xingpeng Li, “Optimal Skeleton Network Reconfiguration considering Topological Characteristics and Transmission Path,” *53rd North American Power Symposium, College Station*, TX, USA, Nov. 2021.

(5) Jin Lu and Xingpeng Li, “Power and Hydrogen Hybrid Transmission for Renewable Energy Systems: An Integrated Expansion Planning Strategy”, *Renewable Energy* (under review).

(6) Jin Lu, Xingpeng Li, Hongyi Li, Taher Chegini, Carlos Gamarra, Y. C. Ethan Yang, Margaret Cook, and Gavin Dillingham, “A Synthetic Texas Backbone Power System with Climate-Dependent Spatio-Temporal Correlated Profiles”, *IEEE Transactions on Power Systems* (under review).

(7) Jesus Silva-Rodriguez, Jin Lu and Xingpeng Li, “Cost-Benefit Analysis and Comparisons for Different Offshore Wind Energy Transmission Systems”, *Offshore Technology Conference, Houston*, TX, USA, May 2023.

(8) Jonathan Yang, Mingjian Tuo, Jin Lu, and Xingpeng Li, “Analysis of Weather and Time Features in Machine Learning-aided ERCOT Load Forecasting”, *IEEE Texas Power and Energy Conference*, College Station, TX, Feb. 2024.

REFERENCES

[1] M. Yue, H. Lambert, E. Pahon, R. Roche, S. Jemei, and D. Hissel, "Hydrogen Energy Systems: A Critical Review of Technologies, Applications, Trends and Challenges," *Renewable and Sustainable Energy Reviews*, vol. 146, p. 111180, 2021

[2] J. Hwang, K. Maharjan, and H. Cho, "A Review of Hydrogen Utilization in Power Generation and Transportation Sectors: Achievements and Future Challenges," *International Journal of Hydrogen Energy*, vol. 48, no. 74, pp. 28629–28648, 2023.

[3] N. Stetson and M. Wieliczko, "Hydrogen Technologies for Energy Storage: A Perspective," *MRS Energy & Sustainability*, vol. 7, no. 1, 2020.

[4] M.A. Aminudin, S.K. Kamarudin, B.H. Lim, E.H. Majilan, M.S. Masdar, and N. Shaari, "An Overview: Current Progress on Hydrogen Fuel Cell Vehicles," *International Journal of Hydrogen Energy*, vol. 48, no. 11, pp. 4371–4388, 2023.

[5] H. T. Hwang and A. Varma, "Hydrogen Storage Methods for Fuel Cell Vehicles: Current Status," *Reference Module in Chemistry, Molecular Sci-ences and Chemical Engineering*, 2015.

[6] B. Johnston, M. C. Mayo, and A. Khare, "Hydrogen: The Energy Source for the 21st Century," *Technovation*, vol. 25, no. 6, pp. 569–585, 2005.

[7] B. Olateju and A. Kumar, "Clean Energy Based Production of Hydrogen: An Energy Carrier," *Handbook of Clean Energy Systems*, pp. 1–30, 2015.

[8] L. Ge, B. Zhang, W. Huang, Y. Li, L. Hou, J. Xiao, Z. Mao, and X. Li, "A Review of Hydrogen Generation, Storage, and Applications in Power System," *Journal of Energy Storage*, vol. 75, p. 109307, 2023.

[9] S. Bennoua, A. Le Duigou, M.-M. Quéméré, and S. Dautremont, "Role of Hydrogen in Resolving Electricity Grid Issues," *International Journal of Hydrogen Energy*, vol. 40, no. 23, pp. 7231–7245, 2015.

[10] R. Lin, Y. Zhao, and B. Wu, "Toward a Hydrogen Society: Hydrogen and Smart Grid Integration," *International Journal of Hydrogen Energy*, vol. 45, no. 39, pp. 20164–20175, 2020.

[11] H. Zhang, W. Xiang, W. Lin, and J. Wen, "Grid Forming Converters in Renewable Energy Sources Dominated Power Grid: Control Strategy, Stability, Application, and Challenges," *Journal of Modern Power Systems and Clean Energy*, vol. 9, no. 6, pp. 1239–1256, 2021.

[12] V. Monteiro, J. S. Martins, J. C. Aparício Fernandes, and J. L. Afonso, "Review of a Disruptive Vision of Future Power Grids: A New Path Based on Hybrid AC/DC Grids and Solid-State Transformers," *Sustainability*, vol. 13, no. 16, p. 9423, 2021.

[13] R. Xie, W. Wei, M. Li, Z. Dong, and S. Mei, "Sizing Capacities of Renewable Generation, Transmission, and Energy Storage for Low-Carbon Power Systems: A Distributionally Robust Optimization Approach," *Energy*, vol. 263, p. 125653, 2023.

[14] M. Rahman, S. Tanzil, R. H. Ritu, and D. M. Kamunya, “Geographical Distribution of Renewable Energy Production for Maximum Efficiency and Environmental Sustainability,” *9th International Conference on Modern Power Systems*, 2021.

[15] Statista Research Department, “Gas Pipeline Capacity by Status Worldwide,” Statista, https://www.statista.com/statistics/1131492/gas-pipeline-capacity-by-status-worldwide/ (accessed Dec. 4, 2023).

[16] “Hydrogen Pipelines,” Office of Energy Efficiency & Renewable Energy, https://www.energy.gov/eere/fuelcells/hydrogen-pipelines (accessed Dec. 4, 2023).

[17] P. Parfomak. “Pipeline Transportation of Hydrogen: Regulation, Research, and Policy,” No. R46700, 2021.

[18] California Public Utilities Commission, “CPUC Acts to Advance Understanding of Hydrogen's Role as Decarbonization Strategy,” 2022, https://www.cpuc.ca.gov/news-and-updates/all-news/cpuc-acts-to-advance-understanding-of-hydrogen-role-as-decarbonization-strategy.

[19] N. Simon, P. E. Mike McCurdy, and P. E. Heidi Marie Larson, “Examining the Current and Future Economics of Hydrogen Energy,” ICF International, Inc., https://www.icf.com/insights/energy/economics-hydrogen-energy (accessed Dec. 4, 2023).

[20] L. Stalker, J. J. Roberts, L. Mabon, and P. G. Hartley, “Communicating Leakage Risk in the Hydrogen Economy: Lessons Already Learned From Geoenergy Industries,” *Frontiers in Energy Research*, vol. 10, 2022.

[21] D. Hauglustaine, F. Paulot, W. Collins, R. Derwent, M. Sand, and O. Boucher, “Climate Benefit of A Future Hydrogen Economy,” *Communications Earth & Environment*, vol. 3, no. 1, 2022.

[22] G. Glenk and S. Reichelstein, “Reversible Power-to-gas Systems for Energy Conversion and Storage,” *Nature Communications*, vol. 13, no. 1, 2022.

[23] F. BARBIR, “Efficiency and Economics of Proton Exchange Membrane (PEM) Fuel Cells,” *International Journal of Hydrogen Energy*, vol. 21, no. 10, pp. 891–901, 1996.

[24] M. Carmo, D. L. Fritz, J. Mergel, and D. Stolten, “A Comprehensive Review on PEM Water Electrolysis,” *International Journal of Hydrogen Energy*, vol. 38, no. 12, pp. 4901–4934, 2013.

[25] J. Bernholz. "RWE’s Former, Current and Possible Future Energy Storage Applications," VGB Kongress & IEKE Workshop. 2018.

[26] L. Fan, Z. Tu, and S. H. Chan, “Recent Development of Hydrogen and Fuel Cell Technologies: A Review,” *Energy Reports*, vol. 7, pp. 8421–8446, 2021.

[27] S. Rahman, “Fuel Cell As A Distributed Generation Technology,” *Power Engineering Society Summer Meeting*, 2001.

[28] G. Glenk, P. Holler, and S. Reichelstein, “Advances in Power-to-gas Technologies: Cost and Conversion Efficiency,” *SSRN Electronic Journal*, 2022.

[29] B. C. Tashie-Lewis and S. G. Nnabuife, “Hydrogen Production, Distribution, Storage and Power Conversion in A Hydrogen Economy - A Technology Review,” *Chemical Engineering Journal Advances*, vol. 8, p. 100172, 2021.

[30] H. Singh, C. Li, P. Cheng, X. Wang, and Q. Liu, “A Critical Review of Technologies, Costs, and Projects for Production of Carbon-neutral Liquid E-fuels From Hydrogen and Captured co2,” *Energy Advances*, vol. 1, no. 9, pp. 580–605, 2022.

[31] J. M. Bracci, E. D. Sherwin, N. L. Boness, and A. R. Brandt, “A Cost Comparison of Various Hourly-reliable and Net-zero Hydrogen Production Pathways in the United States,” *Nature Communications*, vol. 14, no. 1, 2023.

[32] E. Taibi, R. Miranda, M. Carmo, and H. Blanco, "Green Hydrogen Cost Reduction," *International Renewable Energy Agency (IRENA)*, 2020.

[33] F. Pasimeni, U. Sezer, F. Boshell, and G. Boedt, "Innovation Trends in Electrolysers for Hydrogen Production: Patent Insight Report," 2022. Online access: https://research.tue.nl/en/publications/innovation-trends-in-electrolysers-for-hydrogen-production-patent

[34] K. Jiao, J. Xuan, Q. Du, Z. Bao, B. Xie, B. Wang, Y. Zhao, L. Fan, H. Wang, Z. Hou, S. Huo, N.P. Brandon, Y. Yin, and M.D. Guiver, "Designing the Next

Generation of Proton-exchange Membrane Fuel Cells," Nature, 595(7867), pp. 361-369, 2021.

[35] K. Hong, M. Choi, Y. Bae, J. Min, J. Lee, D. Kim, S. Bang, H.-K. Lee, W. Lee, and J. Hong, “Direct Methane Protonic Ceramic Fuel Cells with Self-Assembled Ni-Rh Bimetallic Catalyst,” *Nature Communications*, vol. 14, no. 1, 2023.

[36] K. Sun, J. Dong, H. Sun, X. Wang, J. Fang, Z. Zhuang, S. Tian, and X. Sun, “Co(CN)3 catalysts with Well-Defined Coordination Structure for the Oxygen Reduction Reaction,” *Nature Catalysis*, 2023.

[37] Mo. Mohitpour, H. Solanky, and G. K. Vinjamuri, “Materials Selection and Performance Criteria for Hydrogen Pipeline Transmission,” *ASME Pressure Vessels and Piping Conference*, 2004.

[38] N. Ishikawa, J. Shimamura, D. Izumi, H. Okano, and Y. Nishihara, “Hydrogen Effect on Linepipe Steel and Material Compatibility to A High-Pressure Hydrogen Pipeline,” *International Journal of Offshore and Polar Engineering*, vol. 32, no. 4, pp. 448–456, 2022.

[39] R. Hill and A. Perez, “Line Pipe Material Consideration for Transport of High-Pressure Hydrogen,” *AISTech 2022 Proceedings of the Iron and Steel Technology Conference*, 2022.

[40] Mingjian Tuo and Xingpeng Li, “Security-Constrained Unit Commitment Considering Locational Frequency Stability in Low-Inertia Power Grids,” *IEEE Transaction on Power System*, Oct. 2022.

[41] Arun Venkatesh Ramesh and Xingpeng Li, “Feasibility Layer Aided Machine Learning Approach for Day Ahead Operations,” *IEEE Transactions on Power Systems*, Apr. 2023.

[42] E. Ghirardi, G. Brumana, G. Franchini, and A. Perdichizzi, “H2 Contribution to Power Grid Stability in High Renewable Penetration Scenarios,” *International Journal of Hydrogen Energy*, vol. 48, no. 32, pp. 11956–11969, 2023.

[43] G. Glenk and S. Reichelstein, “Economics of Converting Renewable Power to Hydrogen,” *Nature Energy*, vol. 4, no. 3, pp. 216–222, 2019.

[44] R.Y. Kannah, S. Kavitha, Preethi, O.P. Karthikeyan, G. Kumar, N.V. Dai-Viet, and J.R. Banu, “Techno-economic Assessment of Various Hydrogen Production Methods – A Review,” *Bioresource Technology*, vol. 319, p. 124175, 2021.

[45] U.S. Department of Energy (DOE), “20% Wind Energy by 2030: Increasing Wind Energy’s Contribution to U.S. Electricity Supply,” 2008.

[46] S. Impram, S. V. Nese and B. Oral, “Challenges of Renewable Energy Penetration on Power System Flexibility: A survey,” in *Energy Strategy Reviews*, vol. 31, p.100539, 2020.

[47] S. Ali, S. Ramteen, J. C. Antonio, A. Saeed, “The Role of Energy Storage in Mitigating Ramping Inefficiencies Caused by Variable Renewable Generation,” in *Energy Conversion and Management*, Vol. 162, pp. 307-320, April 2018.

[48] H. K. Jacobsen, and S. T. Schröder, “Curtailment of Renewable Generation: Economic Optimality and Incentives,” *Energy Policy*, 49, pp.663-675. 2012.

[49] H. Schermeyer, C. Vergara and W. Fichtner, “Renewable Energy Curtailment: A Case Study on Today's and Tomorrow's Congestion Management,” *Energy Policy*, vol. 112, pp.427-436. 2018

[50] L. Bird, D. Lew, M. Milligan, E. M. Carlini, A. Estanqueiro, D. Flynn, E. Gomez-Lazaro, H. Holttinen, N. Menemenlis, A. Orths and P. B. Eriksen, “Wind and Solar Energy Curtailment: A review of International Experience,” *Renewable and Sustainable Energy Reviews*, vol. 65, pp.577-586. 2016.

[51] A. V. Ramesh and X. Li, “Reducing Congestion-Induced Renewable Curtailment with Corrective Network Reconfiguration in Day-ahead Scheduling,” *IEEE PES General Meeting 2020*, Montreal, QC, Canada, Jul. 2020.

[52] A. V. Ramesh and X. Li, “Network Reconfiguration Impact on Renewable Energy System and Energy Storage System in Day-ahead Scheduling,” *IEEE PES General Meeting 2021*, Washington, DC, USA, Jul. 2021.

[53] X. Li and Q. Xia, “Stochastic Optimal Power Flow with Network Reconfiguration: Congestion Management and Facilitating Grid Integration of Renewables,” *IEEE PES T&D Conference & Exposition*, Chicago, IL, USA, Oct. 2020.

[54] California ISO, “Fast Facts: Impacts of Renewable Energy on Grid Operations,” May 2017.

[55] California ISO, “Stay Informed - Managing Oversupply,” Jan 2022.

[56] J. Lu and X. Li, “Optimal Skeleton Network Reconfiguration Considering Topological Characteristics and Transmission Path,” *53rd North American Power Symposium*, College Station, TX, USA, Nov. 2021.

[57] D. B. Richardson, “Electric Vehicles and the Electric Grid: A Review of Modeling Approaches, Impacts, and Renewable Energy Integration,” in *Renewable and Sustainable Energy Reviews*, vol. 19, pp.247-254. 2013.

[58] N. K. C. Nair, and N. Garimella, “Battery Energy Storage Systems: Assessment for Small-scale Renewable Energy Integration,” *Energy and Buildings*, vol. 42, pp.2124-2130. 2010.

[59] D. Stenclik, P. Denholm and B. Chalamala, "Maintaining Balance: The Increasing Role of Energy Storage for Renewable Integration," in *IEEE Power and Energy Magazine*, vol. 15, no. 6, pp. 31-39, Nov.-Dec. 2017.

[60] H. S. De Boer, L. Grond, H. Moll and R. Benders, “The Application of Power-to-gas, Pumped Hydro Storage and Compressed Air Energy Storage In An Electricity System at Different Wind Power Penetration Levels,” in *Energy*, vol. 72, pp.360-370. 2014.

[61] B. Yodwong, D. Guilbert, M. Phattanasak, W. Kaewmanee, M. Hinaje. and G. Vitale, “AC-DC Converters for Electrolyzer Applications: State of the Art and Future Challenges,” in *Electronics*, vol. 9, no. 6, p.912, May 2020.

[62] S. Mekhilef, R. Saidur. and A. Safari, “Comparative Study of Different Fuel Cell Technologies,” in *Renewable and Sustainable Energy Reviews*, vol.16, pp.981-989. Jan. 2012.

[63] Y. H. Li, S. Rajakaruna and S. S. Choi, "Control of a Solid Oxide Fuel Cell Power Plant in a Grid-connected System," in *IEEE Transactions on Energy Conversion*, vol. 22, no. 2, pp. 405-413, Jun. 2007.

[64] M. Ban, J. Yu, M. Shahidehpour and Y. Yao, "Integration of Power-to-hydrogen in Day-Ahead Security-Constrained Unit Commitment with High Wind Penetration," in *Journal of Modern Power Systems and Clean Energy*, vol. 5, no. 3, pp. 337-349, May 2017.

[65] Firstgas Group, "Firstgas Group Commented the CCC for Retaining Energy Options," Jun. 2021.

[66] European Commission, "Communication from the Commission to the European Parliament, the Council, the European Economic and Social Committee and the Committee of the Regions - A hydrogen Strategy for a Climate-Neutral Europe," Aug. 2020.

[67] U.S. Department of Energy, "HyBlend: Opportunities for Hydrogen Blending in Natural Gas Pipelines," June 2021.

[68] A. V Ramesh and X. Li, "Enhancing System Flexibility Through Corrective Demand Response in Security-Constrained Unit Commitment," in *2020 52nd North American Power Symposium*, April 2021.

[69] A. V. Ramesh, X. Li and K.W. Hedman, "An Accelerated-Decomposition Approach for Security-Constrained Unit Commitment with Corrective Network Reconfiguration," in *IEEE Transactions on Power Systems*, vol. 37, no. 2, pp. 887-900, Mar. 2022.

[70] A. V. Ramesh and X. Li, “Security Constrained Unit Commitment with Corrective Transmission Switching,” *North American Power Symposium*, Wichita, KS, USA, Oct. 2019.

[71] X. Li, A. S. Korad, and P. Balasubramanian, “Sensitivity Factors based Transmission Network Topology Control for Violation Relief,” in *IET Generation, Transmission & Distribution*, July 2020.

[72] C. Grigg, P. Wong, P. Albrecht, R. Allan, M. Bhavaraju, R. Billinton, Q. Chen, C. Fong, S. Haddad, S. Kuruganty, W. Li, R. Mukerji, D. Patton, N. Rau, D. Reppen, A. Schneider, M. Shahidehpour, and C. Singh, "The IEEE Reliability Test System-1996. A Report Prepared by the Reliability Test System Task Force of the Application of Probability Methods Subcommittee," in *IEEE Transactions on Power Systems*, vol. 14, no. 3, pp. 1010-1020, Aug. 1999.

[73] A. Gallo, P. A. Vázquez-Canteli, and Z. Nagy, “The Role of Flywheel Energy Storage in Addressing Renewable Energy Intermittency and Grid Stability,” *Renewable Energy*, vol. 128, pp. 163-174, Feb. 2018.

[74] B. E. Conway, “Electrochemical Supercapacitors: Scientific Fundamentals and Technological Applications,” Kluwer Academic/Plenum Publishers, 1999.

[75] O. Kruck, F. Crotogino, R. Prelicz, and T. Rudolph, “Design Aspects of Salt Caverns for Hydrogen Storage,” *International Journal of Hydrogen Energy*, vol. 38, no. 10, pp. 4507-4517, Apr. 2013.

[76] N. Heinemann, J. Alcalde, M. S. Miocic, M. Wilkinson, M. G. Haszeldine, and R. E. Shipton, “Salt Caverns for Hydrogen Storage: Practical Applications in

Energy Systems," *International Journal of Hydrogen Energy*, vol. 44, no. 14, pp. 7913-7924, Mar. 2019.

[77] A. Amid, M. Mignard, and D. Wilkinson, "Hydrogen Storage in Salt Caverns: Integration with Renewable Energy Systems," *International Journal of Hydrogen Energy*, vol. 41, no. 1, pp. 554-570, Jan. 2016.

[78] H. Wang, J. Song, and X. Zhang, "Seasonal Hydrogen Storage in Multi-Energy Systems: A Mathematical Modeling Approach," *Energy*, vol. 162, pp. 260-273, Nov. 2018.

[79] M. Anwar, R. Chokhawala, and K. L. Walton, "Annual Management of Power Grids with Integrated Hydrogen and Heat Systems," *Energy Conversion and Management*, vol. 220, p. 113016, Aug. 2020.

[80] X. Zhang, H. Wang, and J. Wang, "Cost-Effectiveness and Environmental Impact of Hydrogen Storage Integration with Renewable Energy Sources," *Renewable and Sustainable Energy Reviews*, vol. 135, p. 110239, Jan. 2021.

[81] IRENA, "Hydrogen from Renewable Power: Technology Outlook for the Energy Transition," 2018.

[82] Hydrogen and Fuel Cell Technologies Office, "Hydrogen Storage," Energy.gov.

[83] M. A. Semeraro, "Renewable Energy Transport via Hydrogen Pipelines and HVDC Transmission Lines," *Energy Strategy Reviews*, vol. 35, 2021.

[84] Z. Xin-gang, L. Ji, M. Jin, and Z. Ying, "An Improved Quantum Particle Swarm Optimization Algorithm for Environmental Economic Dispatch," *Expert Systems with Applications*, vol. 152, p. 113370, 2020.

[85] X. Li and Q. Xia, “Power System Expansion Planning with Seasonal Network Optimization,” *Innovative Smart Grid Technologies (ISGT)*, Washington D.C., USA, Feb. 2020.

[86] J. Lu and X. Li, “Optimal Skeleton Network Reconfiguration Considering Topological Characteristics and Transmission path,” *53rd North American Power Symposium (NAPS)*, 2021.

[87] N. Bhusal, M. Abdelmalak, M. Kamruzzaman, and M. Benidris, “Power System Resilience: Current Practices, Challenges, and Future Directions,” *IEEE Access*, vol. 8, pp. 18064–18086, 2020.

[88] S. Peyghami, P. Davari, M. Fotuhi-Firuzabad, and F. Blaabjerg, “Standard Test Systems for Modern Power System Analysis: An Overview,” *IEEE Industrial Electronics Magazine*, vol. 13, no. 4, pp. 86–105, 2019.

[89] J. Snodgrass, S. Kunkolienkar, U. Habiba, Y. Liu, M. Stevens, F. Safdarian, T. Overbye, and R. Korab, “Case Study of Enhancing the MATPOWER Polish Electric Grid,” *IEEE Texas Power and Energy Conference (TPEC)*, 2022.

[90] Texas A&M University Electric grid test case repository. https://electricgrids.engr.tamu.edu/electric-grid-test-cases/

[91] H. Shakouri G. and S. Aliakbarisani, “At What Valuation of Sustainability Can We Abandon Fossil Fuels? A Comprehensive Multistage Decision Support Model for Electricity Planning,” *Energy*, vol. 107, pp. 60–77, 2016.

[92] Renewable Power Grid Lab, University of Houston, “Resources / Synthetic Texas 345 kV Backbone Transmission System (TX-123BT) with Climate-

Dependent Spatio-Temporal Correlated Profiles," [Online]. Available at: https://rpglab.github.io/resources/TX-123BT/

[93] J. Lu and X. Li, "Texas Synthetic Power System Test Case (TX-123BT)," figshare, 23-Feb-2023, doi: 10.6084/m9.figshare.22144616.

[94] Y. Xia, B. A. Cosgrove, M. B. Ek, J. Sheffield, L. Luo, E. F. Wood, and K. Mo, "Overview of the North American Land Data Assimilation System (NLDAS)," *Land Surface Observation, Modeling and Data Assimilation*, pp. 337–377, 2013.

[95] README Document for North American Land Data Assimilation System Phase 2 (NLDAS-2) Products. https://hydro1.gesdisc.eosdis.nasa.gov/data/NLDAS/README.NLDAS2.pdf

[96] A.B. Birchfield, T. Xu, K.M. Gegner, K.S. Shetye, T.J. Overbye, "Grid Structural Characteristics as Validation Criteria for Synthetic Networks," *IEEE Transactions on Power Systems*, vol. 32, no. 4, pp. 3258-3265, July 2017.

[97] ERCOT report for interval generation by fuel. http://www.ercot.com/content/wcm/lists/181766/IntGenbyFuel2021.xlsx

[98] ERCOT winter capacity by fuel type. https://www.spglobal.com/marketintelligence/en/news-insights/latest-news-headlines/as-texas-digs-out-plans-proceed-to-add-35-gw-of-solar-wind-capacity-to-grid-62719521

[99] The U.S. generators fuel type data by EIA: https://www.eia.gov/state/maps.php

[100] T. Xu, A. B. Birchfield, K. M. Gegner, K. S. Shetye, and T. J. Overbye, "Application of Large-scale Synthetic Power System Models for Energy Economic Studies," *Proceedings of the 50th Hawaii International Conference on System Sciences (2017)*, 2017.

[101] "Gas Power Plant Fuel Requirements and Uncertainty Considering Increasing Renewables Penetration," [Online]. Available: https://www.researchgate.net/profile/Jarrad-Wright/publication.

[102] Average Cost of Coal Delivered for Electricity Generation by EIA. https://www.eia.gov/electricity/monthly/xls/table_4_10_a.xlsx

[103] Texas Heat Content of Natural Gas by EIA. https://www.eia.gov/dnav/ng/hist/nga_epg0_vgth_stx_btucfa.htm

[104] Power Plant Cycling Cost by NREL: https://www.nrel.gov/docs/fy12osti/55433.pdf

[105] Average Power Plant Operating Expenses for Major U.S. Investor-Owned Electric Utilities by EIA. https://www.eia.gov/electricity/annual/html/epa_08_04.html

[106] Technical and Economic Aspects of Load Following with Nuclear Power Plants by OECD. https://www.oecd-nea.org/ndd/reports/2011/load-following-npp.pdf

[107] Published by Statista Research Department, "U.S. Hydroelectric Power Plant Operating Expenses 2021," Statista.

[108] Y.R. Glazer, D.M. Tremaine, J.L. Banner, M. Cook, R.E. Mace, J. Nielsen-Gammon, E. Grubert, K. Kramer, A.M.K. Stoner, B.M. Wyatt, A. Mayer, T.

Beach, R. Correll, and M.E. Webber, “Winter Storm Uri: A Test of Texas’ Water Infrastructure and Water Resource Resilience to Extreme Winter Weather Events,” *Journal of Extreme Events*, vol. 08, no. 04, 2021.

[109] “Optimizing Wind Generation in ERCOT Nodal Market”, *FERC Conference on Increasing Real-Time and Day-Ahead Market Efficiency through Improved Software*, June 2014.

[110] ERCOT Hourly Aggregated Wind Output. https://www.ercot.com/misapp/GetReports.do?reportTypeId=13424&reportTitle=Hourly%20Aggregated%20Wind%20Output&showHTMLView=&mimicKey

[111] J. Gerdes, “Kissing the Sky: The Pros and Cons of Ultra-Tall Wind Turbine Towers,” *Greentech Media*, 05-Sep-2019. [Online]. Available: https://www.greentechmedia.com/articles/read/the-pros-and-cons-of-ultra-tall-wind-turbine-towers.

[112] J. D. Holmes and S. Bekele, Wind Loading of Structures. Boca Raton: CRC Press, 2022.

[113] J.L. Gray, “The Physics of the Solar Cell,” *Handbook of Photovoltaic Science and Engineering*, 2011.

[114] W. De Soto, S. A. Klein, and W. A. Beckman, “Improvement and Validation of a Model for Photovoltaic Array Performance,” *Solar Energy*, vol. 80, no. 1, pp. 78–88, 2006.

[115] "IEEE Standard for Calculating the Current-Temperature Relationship of Bare Overhead Conductors," *IEEE Std 738-2012*, pp.1-72, Dec. 2013.

[116] J. Lu and X. Li, "The Benefits of Hydrogen Energy Transmission and Conversion Systems to the Renewable Power Grids: Day-ahead Unit Commitment," *54th North American Power Symposium*, Oct. 2022.

[117] M. I. Aydin, I. Dincer, and H. Ha, "Development of Oshawa Hydrogen Hub in Canada: A Case Study," *International Journal of Hydrogen Energy*, vol. 46, no. 47, pp. 23997–24010, Jul. 2021.

[118] Lawrence Livermore National Laboratory, "CMIP6 - Coupled Model Intercomparison Project Phase 6," https://pcmdi.llnl.gov/CMIP6/ (accessed Sep. 24, 2023).

[119] K. Riahi, S. Rao, V. Krey, C. Cho, V. Chirkov, G. Fischer, G. Kindermann, N. Nakicenovic, and P. Rafaj, "RCP 8.5—a Scenario of Comparatively High Greenhouse Gas Emissions," *Climatic Change*, vol. 109, no. 1–2, pp. 33–57, Aug. 2011.

[120] NASA, "NLDAS-2 Model Data," https://ldas.gsfc.nasa.gov/nldas/nldas-2-model-data (accessed Sep. 10, 2023).

[121] J. Holmes, P. Carol, and K. Robert, "Wind Loading of Structures," CRC press, 2007.

[122] A. Ghaffari, F. Hung, J. Lu and X. Li, "Development of a Coupled Agent-based Generation Expansion Planning Tool with a Power Dispatch Model," *Energy Clim. Change*, under review.

[123] M. S. Kandil, S. M. El-Debeiky, and N. E. Hasanien, "Long-Term Load Forecasting for Fast Developing Utility Using a Knowledge-based Expert System," *IEEE Trans. Power Syst.*, vol. 17, no. 2, pp. 491–496, May 2002.

[124] J. Zhu, Z. Yang, M. Mourshed, Y. Guo, Y. Zhou, Y. Chang, Y. Wei, and S. Feng, "Electric Vehicle Charging Load Forecasting: A Comparative Study of Deep Learning Approaches," *Energies*, vol. 12, no. 14, p. 2692, July 2019.

[125] Federal Energy Regulatory Commission (FERC), "FERC Order 2003: Initial Pro Forma Large Generator Interconnection Procedures (LGIP)," https://ferc.gov/electric-transmission/generator-interconnection/final-rules-establishing-and-revising-standard

[126] A. Moreira, D. Pozo, A. Street, and E. Sauma, "Reliable Renewable Generation and Transmission Expansion Planning: Co-optimizing System's Resources for Meeting Renewable Targets," *IEEE Trans. Power Syst.*, vol. 32, no. 4, pp. 3246–3257, Nov. 2017.

[127] Intergovernmental panel on climate change (IPCC), "Climate Change 2021: The Physical Science Basis," https://report.ipcc.ch/ar6/wg1/IPCC_AR6_WGI_FullReport.pdf

[128] J. Hansen, M. Sato, R. Ruedy, and M. Medina-Elizade, "Global Temperature Change," *Proc. Natl. Acad. Sci. U.S.A.*, vol. 103, no. 39, pp. 14288-14293, Sep. 2006.

[129] M. Auffhammer, P. Baylis, and C. H. Hausman, "Climate Change is Projected to Have Severe Impacts on the Frequency and Intensity of Peak Electricity

Demand Across the United States," *Proc. Natl. Acad. Sci. U.S.A.*, vol. 114, no. 8, pp. 1886–1891, 2017.

[130] F. Qiu and J. Wang, "Distributionally Robust Congestion Management with Dynamic Line Ratings," *IEEE Trans. Power Syst.*, vol. 30, no. 4, pp. 2198–2199, July 2015.

[131] M. A. Russo, D. Carvalho, N. Martins, and A. Monteiro, "Forecasting the Inevitable: A Review on the Impacts of Climate Change on Renewable Energy Resources," *Sustainable Energy Technol. Assessments*, vol. 52, p. 102283, May 2022.

[132] P. Dhanasekar, C. Zhao and X. Li, "Quantitative Analysis of Demand Response Using Thermostatically Controlled Loads," *IEEE PES Innovative Smart Grid Technology (ISGT)*, Apr. 2022.

[133] National Renewable Energy Laboratory, "2022 Standard Scenarios Report: A U.S. Electricity Sector Outlook," Jan. 2023.

[134] U.S. Department of Energy (DOE), "Operation and Planning Tools for Inverter-Based Resource Management and Availability for Future Power Systems (Optima)," Energy Communities, https://energycommunities.gov/funding-opportunity/operation-and-planning-tools-for-inverter-based-resource-management-and-availability-for-future-power-systems-optima/ (accessed Sep. 10, 2023).

[135] M.T. Craig, S. Cohen, J. Macknick, C. Draxl, O.J. Guerra, M. Sengupta, S.E. Haupt, B.-M. Hodge, and C. Brancucci, "A Review of the Potential Impacts of

Climate Change on Bulk Power System Planning and Operations in the United States," *Renew. Sustain. Energy Rev.*, vol. 98, pp. 255–267, Sep. 2018.

[136] K. Handayani, T. Filatova, Y. Krozer, and P. Anugrah, "Seeking for a Climate Change Mitigation and Adaptation Nexus: Analysis of a Long-Term Power System Expansion," *Appl. Energy*, vol. 262, p. 114485, Jan. 2020.

[137] J. N. Fidalgo, D. de Sao Jose, and C. Silva, "Impact of Climate Changes on the Portuguese Energy Generation Mix," *2019 16th Int. Conf. Eur. Energy Market*, Lisbon, Portugal, Sep. 2019.

[138] M. D. Esteban, J. J. Diez, J. S. López, V. Negro, "Why Offshore Wind Energy?," *Renewable Energy*, vol. 36, issue 2, 2011, pp. 444-450.

[139] S. Lauria, M. Schembari, F. Palone, M. Maccioni, "Very Long Distance Connection of Gigawatt-Size Offshore Wind Farms: Extra High-Voltage AC Versus High-Voltage DC Cost Comparison," *IET Renewable Power Generation*, 2016, pp. 713-720.

[140] K. Nieradzinska, C. MacIver, S. Gill, G.A. Agnew, O. Anaya-Lara, K.R.W. Bell, "Optioneering Analysis for Connecting Dogger Bank Offshore Wind Farms to the GB Electricity Network," *Renewable Energy*, vol. 91, 2016, pp. 120-129.

[141] D. Ferrero, M. Gamba, A. Lanzini, M. Santarelli, "Power-to-Gas Hydrogen: Techno-Economic Assessment of Processes Towards a Multi-Purpose Energy Carrier," *Energy Procedia*, vol. 101, 2016, pp. 50-57.

[142] J. Lu and X. Li, “Annual Benefit Analysis of Integrating the Seasonal Hydrogen Storage into the Renewable Power Grids,” *arXiv*:2211.11097, Nov. 2022.

[143] A. Taieb and M. Shaaban, "Cost Analysis of Electricity Transmission from Offshore Wind Farm by HVDC and Hydrogen Pipeline Systems," *2019 IEEE PES GTD Grand International Conference and Exposition Asia (GTD Asia)*, 2019, pp. 632-636.

[144] B. Miao, L. Giordano, S. H. Chan, “Long-Distance Renewable Hydrogen Transmission Via Cables and Pipelines,” *International Journal of Hydrogen Energy*, vol. 46, issue 36, 2021, pp. 18699-18718.

[145] M. A. Semeraro, “Renewable Energy Transport Via Hydrogen Pipelines and HVDC Transmission Lines,” *Energy Strategy Reviews*, vol. 35, 2021.

[146] D. De Wolf, Y. Smeers, “Optimal Dimensioning of Pipe Networks with Application to Gas Transmission Networks,” *Operations Research*, 1996.

[147] J. André, S. Auray, J. Brac, D. De Wolf, G. Maisonnier, M. Ould-Sidi, A. Simonnet, “Design and Dimensioning of Hydrogen Transmission Pipeline Networks,” *European Journal of Operational Research*, vol. 229, issue 1, 2013, pp. 239-251.

[148] IRENA, “Hydrogen from Renewable Power: Technology Outlook for the Energy Transition,” 2018. [online] Available: https://irena.org/publications/2018/Sep/Hydrogen-from-renewable-power//irena.org/publications/2018/Sep/Hydrogen-from-renewable-power.

[149] G. Parks, R. Boyd, J. Cornish, R. Remick, "Hydrogen Station Compression, Storage, and Dispensing Technical Status and Costs," NREL, May 2014, [Online], Available: https://www.nrel.gov/docs/fy14osti/58564.pdf.

[150] D.D. Papadias, R.K. Ahluwalia, "Bulk Storage of Hydrogen," vol. 46, issue 70, 2021, pp. 34527-34541.

[151] T. Włodek, M. Łaciak, K. Kurowska and Ł. Węgrzyn. "Thermodynamic Analysis of Hydrogen Pipeline Transportation – Selected Aspects," *AGH Drilling, Oil, Gas*, 2016.

[152] M. Klell, "Storage of Hydrogen in the Pure Form," *Handbook of Hydrogen Storage: New Materials for Future Energy Storage*, Wiley, pp. 1-37, March 2010.

[153] Pyomo Package, http://www.pyomo.org/ (accessed Mar. 15, 2024).

[154] Gurobi Optimization Solver, https://www.gurobi.com/ (accessed Mar. 15, 2024).

[155] X. Li and Q. Xia, "Transmission Expansion Planning with Seasonal Network Optimization," *2020 IEEE Power & Energy Soc. Innovative Smart Grid Technol. Conf. (ISGT)*, Washington, D.C., Feb. 2020.

[156] I. Pavičić, N. Holjevac, I. Ivanković, and D. Brnobić, "Model for 400 kV Transmission Line Power Loss Assessment using the PMU Measurements," *Energies*, vol. 14, no. 17, p. 5562, 2021.

[157] Y. Wang, C. Chen, J. Wang and R. Baldick, "Research on Resilience of Power Systems Under Natural Disasters—A Review," in *IEEE Transactions on Power Systems*, vol. 31, no. 2, pp. 1604-1613, March 2016.

[158] Y. Liu, H. Wang and H. Ye, “Power System Restoration Theory and Technology,” Science and Technology Press, Beijing.

[159] Y. Liu, R. Fan and V. Terzija, "Power System Restoration: A Literature Review from 2006 to 2016," *Journal of Modern Power Systems and Clean Energy*, vol. 4, no. 3, pp. 332-341, July 2016.

[160] Y. Hou, C. Liu, K. Sun, P. Zhang, S. Liu and D. Mizumura, "Computation of Milestones for Decision Support During System Restoration," *IEEE Transactions on Power Systems*, vol. 26, no. 3, pp. 1399-1409, Aug. 2011.

[161] A. Golshani, W. Sun, Q. Zhou, Q. P. Zheng and J. Tong, "Two-Stage Adaptive Restoration Decision Support System for a Self-Healing Power Grid," *IEEE Transactions on Industrial Informatics*, vol. 13, no. 6, pp. 2802-2812, Dec. 2017.

[162] W. Sun, C. Liu and L. Zhang, "Optimal Generator Start-Up Strategy for Bulk Power System Restoration," *IEEE Transactions on Power Systems*, vol. 26, no. 3, pp. 1357-1366, Aug. 2011.

[163] H. Zhong and X. Gu, "Determination of Optimal Unit Start-up Sequences Based on Fuzzy AHP in Power System Restoration," *2011 4th International Conference on Electric Utility Deregulation and Restructuring and Power Technologies*, pp. 1541-1545.

[164] H. Zhu, Z. Yu, T. Wang, M. Liu, J. Song, Y. Xue, N. Yang, and Y. Hu, "Generator Restoration After Blackout Based on Preference Optimization method," *2018 International Conference on Power System Technology*, pp. 1135-1142.

[165] Y. Zhao, Z. Lin, Y. Ding, Y. Liu, L. Sun and Y. Yan, "A Model Predictive Control Based Generator Start-Up Optimization Strategy for Restoration with Microgrids as Black-Start Resources," *IEEE Transactions on Power Systems*, vol. 33, no. 6, pp. 7189-7203, Nov. 2018.

[166] Z. Lin, F. Wen and Y. Xue, "A Restorative Self-Healing Algorithm for Transmission Systems Based on Complex Network Theory," *IEEE Transactions on Smart Grid*, vol. 7, no. 4, pp. 2154-2162, July 2016.

[167] C. Wang, V. Vittal, V. S. Kolluri and S. Mandal, "PTDF-Based Automatic Restoration Path Selection," *IEEE Transactions on Power Systems*, vol. 25, no. 3, pp. 1686-1695, Aug. 2010.

[168] C. Zhang, Z. Lin, F. Wen, G. Ledwich and Y. Xue, "Two-stage Power Network Reconfiguration Strategy Considering Node Importance and Restored Generation Capacity," *IET Generation, Transmission & Distribution*, vol. 8, no. 1, pp. 91-103, Jan. 2014.

[169] D.R. Medina, E. Rappold, O. Sanchez, X. Luo, S.R. Rivera Rodriguez, D. Wu, and J.N. Jiang, "Fast Assessment of Frequency Response of Cold Load Pickup in Power System Restoration," *IEEE Transactions on Power Systems*, vol. 31, no. 4, pp. 3249-3256, July 2016.

[170] H. Qu and Y. Liu, “Maximizing Restorable Load Amount for Specific Substation During System Restoration,” *Int J Electr Power Energy Syst*, vol. 43, no. 1, pp. 1213–1220, Dec. 2012.

[171] W. Liu, Z. Lin, F. Wen, and G. Ledwich, “A Wide Area Monitoring System Based Load Restoration Method,” *IEEE Trans Power Syst*, vol. 28, no. 2, pp. 2025–2034, May 2013.

[172] J. Li, H. You, J. Qi, M. Kong, S. Zhang, and H. Zhang, “Stratified Optimization Strategy Used for Restoration with Photovoltaic-Battery Energy Storage Systems as Black-Start Resources,” *IEEE Access*, vol. 7, pp. 127339–127352, 2019.

[173] I. Beil, A. Allen, A. Tokombayev, and M. Hack, “Considerations When Using Utility-Scale Battery Storage to Black Start a Gas Turbine Generator,” *2017 IEEE Power and Energy Society General Meeting*, Jul. 2017.

[174] H. Haggi, W. Sun, J. M. Fenton, and P. Brooker, “Proactive Rolling-Horizon-Based Scheduling of Hydrogen Systems for Resilient Power Grids,” *IEEE Transactions on Industry Applications*, vol. 58, no. 2, pp. 1737–1746, Mar. 2022.

[175] Y. Liu and X. Gu, "Skeleton-Network Reconfiguration Based on Topological Characteristics of Scale-Free Networks and Discrete Particle Swarm Optimization," *IEEE Transactions on Power Systems*, vol. 22, no. 3, pp. 1267-1274, Aug. 2007.

[176] J. -k. Huang, L. Du and G. -s. Zhang, "Skeleton-Network Reconfiguration Based on Node Importance and Line Optimization," *2012 Asia-Pacific Power and Energy Engineering Conference*, pp. 1-4.

[177] H. Jafarian, M. R. Mashhadi and M. H. Javidi, "Skeleton network Reconfiguration for System Restoration in Restructured Power Industry," *2011 19th Iranian Conference on Electrical Engineering*, pp. 1-6.

[178] Z. Lin, F. Wen, H. Wang, G. Lin, T. Mo and X. Ye, "CRITIC-Based Node Importance Evaluation in Skeleton-Network Reconfiguration of Power Grids," *IEEE Transactions on Circuits and Systems II: Express Briefs*, vol. 65, no. 2, pp. 206-210, Feb. 2018.

[179] L. Sun, Z. Lin, Y. Xu, F. Wen, C. Zhang and Y. Xue, "Optimal Skeleton-Network Restoration Considering Generator Start-Up Sequence and Load Pickup," *IEEE Transactions on Smart Grid*, vol. 10, no. 3, pp. 3174-3185, May 2019.

[180] Q. Jiang, X. Li, B. Wang and H. Wang, "PMU-Based Fault Location Using Voltage Measurements in Large Transmission Networks," *IEEE Transactions on Power Delivery*, vol. 27, no. 3, pp. 1644-1652, July 2012.